THE UNIVERSITY OF CHICAGO

TYPE IA SUPERNOVA RATE STUDIES FROM THE SDSS-II SUPERNOVA SURVEY

A DISSERTATION SUBMITTED TO
THE FACULTY OF THE DIVISION OF THE PHYSICAL SCIENCES
IN CANDIDACY FOR THE DEGREE OF
DOCTOR OF PHILOSOPHY

DEPARTMENT OF PHYSICS

BY
BENJAMIN E. P. DILDAY

CHICAGO, ILLINOIS
AUGUST 2008

I dedicate this thesis to you,

the reader.

ABSTRACT

I present new measurements of the type Ia SN rate from the SDSS-II Supernova Survey. The SDSS-II Supernova Survey was carried out during the Fall months (Sept. - Nov.) of 2005-2007 and discovered ≈ 500 spectroscopically confirmed SNe Ia with densely sampled (once every ≈ 4 days), multi-color light curves. Additionally, the SDSS-II Supernova Survey has discovered several hundred SNe Ia candidates with well-measured light curves, but without spectroscopic confirmation of type. This total, achieved in 9 months of observing, represents $\approx 15-20\%$ of the total SNe Ia discovered worldwide since 1885. I describe some technical details of the SN Survey observations and SN search algorithms that contributed to the extremely high-yield of discovered SNe and that are important as context for the SDSS-II Supernova Survey SN Ia rate measurements.

The type Ia SNe rate is an observational constraint on the progenitor systems of SNe Ia, with applications for both fundamental astrophysics (the physics of white dwarf and binary stars) and for the utility of SNe Ia as cosmological distance indicators. I describe 3 separate SN Ia studies: 1) A precise measurement of the SN Ia rate at low-redshift ($z < 0.12$) based on a highly pure sample of SNe Ia with a well measured selection function. 2) A measurement of the type Ia SN rate to a redshift limit $z \lesssim 0.3$, based on ≈ 350 SNe Ia. 3) A measurement of the type Ia SN rate in galaxy clusters in the redshift range $0.03 < z < 0.30$.

The low-redshift SN Ia rate measurement includes 17 SNe Ia at redshift $z \leq 0.12$. Assuming a flat cosmology with $\Omega_m = 0.3 = 1 - \Omega_\Lambda$, we find a volumetric SN Ia rate of $[2.93^{+0.17}_{-0.04}(\text{systematic})^{+0.90}_{-0.71}(\text{statistical})] \times 10^{-5}$ SNe Mpc^{-3} h^3_{70} year^{-1}, at a volume-weighted mean redshift of 0.09. This result is consistent with previous measurements of the SN Ia rate in a similar redshift range. The systematic errors

are well controlled, resulting in the most precise measurement of the SN Ia rate in this redshift range. We use a maximum likelihood method to fit SN rate models to the SDSS-II Supernova Survey data in combination with other rate measurements, thereby constraining models for the redshift-evolution of the SN Ia rate. Fitting the combined data to a simple power-law evolution of the volumetric SN Ia rate, $r_V \propto (1+z)^{\beta}$, we obtain a value of $\beta = 1.5 \pm 0.6$, i.e. the SN Ia rate is determined to be an increasing function of redshift at the $\sim 2.5\sigma$ level. Fitting the results to a model in which the volumetric SN rate, $r_V = A\rho(t) + B\dot{\rho}(t)$, where $\rho(t)$ is the stellar mass density and $\dot{\rho}(t)$ is the star formation rate, we find $A = (2.8 \pm 1.2) \times 10^{-14}$ SNe $M_{\odot}^{-1}$ year^{-1}, $B = (9.3^{+3.4}_{-3.1}) \times 10^{-4}$ SNe $M_{\odot}^{-1}$.

The SN rate measurement to a redshift limit $z \lesssim 0.3$ provides an order of magnitude improvement in the statistics for SN Ia rate measurement in this redshift range. Although systematic uncertainties on the SN rate for $0.2 < z < 0.3$ are significant, the SN rate is determined precisely for $z \lesssim 0.2$ based on a sample of ≈ 132 SNe Ia, with the majority being spectroscopically confirmed. The large sample of SNe Ia included in this study allow us to place constraints on the redshift dependence of the SN Ia rate in the redshift range covered by the SDSS-II Supernova Survey, based on the SDSS-II Supernova Survey data alone.

The SN rate in galaxy clusters is an important complementary probe of both the nature of type Ia SN progenitors and of mechanisms for metal enrichment of the intra-cluster medium (ICM). The SN rate in galaxy clusters has been measured with much less statistical significance than the cosmic SN rate due in part to the relative rarity of galaxy clusters. The measurement of the cluster SN Ia rate from the first two seasons of the SDSS-II Supernova Survey includes 5 events in clusters at $z \lesssim 0.17$ (c4 clusters), and 12 events in clusters in the redshift range $0.1 < z < 0.3$ (maxBCG clusters). There are additionally 3 SNe Ia in low-redshift c4 clusters from

the third season of the SDSS-II Supernova Survey. These measurements represent significant contributions to the study of the SN rate in galaxy clusters, in terms of both statistical significance and redshift coverage. We find values of the SN Ia rate of $0.10^{+0.068}_{-0.043}$ SNuM h^2 and $0.12^{+0.046}_{-0.034}$ SNuM h^2 in c4 and maxBCG clusters, respectively. The SN rate in galaxy clusters as a function of redshift is consistent with a constant rate, which supports the idea that cluster SNe Ia are primarily produced by an old stellar population, with a rate that is weakly dependent on time delay with respect to star formation.

ACKNOWLEDGMENTS

I would like to thank all of my collaborators for making my time working with the SDSS-II Supernova Survey both rewarding and enjoyable. I thank Joshua Frieman for always being generous with his advice and guidance. I thank Rick Kessler also for many useful discussions. I thank my friends and family for their invaluable support over the years.

Funding for the SDSS and SDSS-II has been provided by the Alfred P. Sloan Foundation, the Participating Institutions, the National Science Foundation, the U.S. Department of Energy, the National Aeronautics and Space Administration, the Japanese Monbukagakusho, the Max Planck Society, and the Higher Education Funding Council for England. The SDSS Web Site is http://www.sdss.org/.

The SDSS is managed by the Astrophysical Research Consortium for the Participating Institutions. The Participating Institutions are the American Museum of Natural History, Astrophysical Institute Potsdam, University of Basel, University of Cambridge, Case Western Reserve University, University of Chicago, Drexel University, Fermilab, the Institute for Advanced Study, the Japan Participation Group, Johns Hopkins University, the Joint Institute for Nuclear Astrophysics, the Kavli Institute for Particle Astrophysics and Cosmology, the Korean Scientist Group, the Chinese Academy of Sciences (LAMOST), Los Alamos National Laboratory, the Max-Planck-Institute for Astronomy (MPIA), the Max-Planck-Institute for Astrophysics (MPA), New Mexico State University, Ohio State University, University of Pittsburgh, University of Portsmouth, Princeton University, the United States Naval Observatory, and the University of Washington.

This work is based in part on observations made at the following telescopes.

The Hobby-Eberly Telescope (HET) is a joint project of the University of Texas at Austin, the Pennsylvania State University, Stanford University, Ludwig-Maximillians-Universität München, and Georg-August-Universität Göttingen. The HET is named in honor of its principal benefactors, William P. Hobby and Robert E. Eberly. The Marcario Low-Resolution Spectrograph is named for Mike Marcario of High Lonesome Optics, who fabricated several optical elements for the instrument but died before its completion; it is a joint project of the Hobby-Eberly Telescope partnership and the Instituto de Astronomía de la Universidad Nacional Autónoma de México. The Apache Point Observatory 3.5 m telescope is owned and operated by the Astrophysical Research Consortium. We thank the observatory director, Suzanne Hawley, and site manager, Bruce Gillespie, for their support of this project. The Subaru Telescope is operated by the National Astronomical Observatory of Japan. The William Herschel Telescope is operated by the Isaac Newton Group, on the island of La Palma in the Spanish Observatorio del Roque de los Muchachos of the Instituto de Astrofisica de Canarias. Kitt Peak National Observatory, National Optical Astronomy Observatory, is operated by the Association of Universities for Research in Astronomy, Inc. (AURA) under cooperative agreement with the National Science Foundation. The W.M. Keck Observatory is operated as a scientific partnership among the California Institute of Technology, the University of California, and the National Aeronautics and Space Administration. The Observatory was made possible by the generous financial support of the W. M. Keck Foundation.

This work was supported in part by the Kavli Institute for Cosmological Physics at the University of Chicago through grants NSF PHY-0114422 and NSF PHY-0551142 and an endowment from the Kavli Foundation and its founder Fred Kavli.

TABLE OF CONTENTS

LIST OF FIGURES

LIST OF TABLES

CHAPTER 1

INTRODUCTION

Type Ia supernovae (SNe) occupy a prominent position in contemporary astrophysics for a number of reasons, both theoretical and observational. Type Ia SNe are important sources of iron elements and are important components of theories of galaxy evolution and stellar enrichment. Type Ia SNe provide a rich source for study of theoretical models of stellar/binary evolution and of the physics of nuclear explosions under extreme conditions. Additionally, type Ia SNe are currently the best example of an astrophysical "standard candle", and have been used as cosmic distance indicators to provide the first direct evidence for an accelerated expansion of the universe (Riess et al., 1998; Perlmutter et al., 1999), which is commonly attributed to a "dark energy" component of the universal composition (Frieman et al., 2008a). More precisely, the intrinsic luminosities of type Ia SNe are correlated with an observable quantity, the decline rate of the SN light-curve, and this fact allows the distances to a type Ia SN to be "standardized". The correlation between the absolute magnitude and decline rate for type Ia SNe has been reported at least as far back as Pskovskii (1977), but was quantified statistically, and popularized as a useful observational tool, by Phillips (1993). Therefore this correlation is commonly referred to as the "Phillips relation" and has since been parameterized in different ways and exploited by various methods (e. g. Riess et al. (1996); Jha et al. (2007); Guy et al. (2005, 2007)) to provide accurate relative distance measurements to type Ia SNe, with a precision of $\approx$ 7%.

The realization that type Ia SNe can act as accurate distance indicators over cosmological scales has resulted in a vigorous campaign within the astronomical community to discover and measure large numbers of type Ia SNe. Examples of dedicated SN searches include the Carnegie Supernova Project, the Higher-z SN Search, the

Supernova Cosmology Project (SCP), the Supernova Legacy Survey, the Nearby Supernova Factory, Lick Observatory Supernova Serach (LOSS), and the Equation of State Supernova Trace Cosmic Expansion (ESSENCE) project. Programs for observation and study of type Ia SNe continue to be of high priority for the astronomy community, and large SN samples are expected in the near future from the Dark Energy Survey (DES), the Large Synoptic Survey Telescope (LSST), the Panoramic Survey Telescope & Rapid Response System (PanSTARRS), SkyMapper, and the Joint Dark Energy Mission (JDEM).

One such dedicated SN search program is the recently completed Sloan Digital Sky Survey - II Supernova Survey (SDSS-II SN Survey). The SDSS-II Supernova Survey was conceived with the explicit goals of

- Obtaining well-measured light-curves for several hundred type Ia SNe, in the redshift range $0.05 < z < 0.35$, for measuring distances and placing improved constraints on the cosmic expansion history
- Making precise measurements of the type Ia SN rate with an unbiased sample of SNe
- Exploring and evaluating systematic uncertainties in SN studies
- Measuring rest-frame UV light-curves for many type Ia SNe
- Studying SN demographics and peculiar SNe

An extensive overview of the SDSS-II Supernova Survey is given in Frieman et al. (2008b). Technical details of the SDSS-II Supernova Survey operations are given in Sako et al. (2008). Descriptions of spectroscopic and photometric data reductions are given in Zheng et al. (2008) and Holtzman et al. (2008), respectively. The first cosmological analysis based on SDSS SNe is presented in Kessler et al. (2008). Extensive

studies of the peculiar SNe 2005hk and 2005gj are given in Phillips et al. (2007) and Prieto et al. (2007), respectively. The focus of this thesis will be on studies of the type Ia SN rate, which is motivated in the following section.

1.1 The Physics of the Type Ia SN Rate

There is now broad consensus that a type Ia supernova is the thermonuclear explosion of a Carbon-Oxygen white dwarf star that approaches the Chandrasekhar mass limit (e.g. Branch et al. (1995)) through accretion of mass from a binary companion. However, much remains to be learned about the physics of SNe Ia, and there is active debate about both the nature of the progenitor systems and the details of the explosion mechanism. For example, the binary companion may be a main-sequence star, a giant or sub-giant, or a second white dwarf. The type of the companion star determines in part the predicted time delay between the formation of the binary system and the SN event (Greggio, 2005). The time delay can be constrained observationally by comparing the SN Ia rate as a function of redshift to the star formation history (SFH) (Strolger et al., 2004; Cappellaro et al., 2007).

The insight into the nature of the progenitor systems that SN Ia rate measurements provide can also potentially strengthen the utility of SNe Ia as cosmological distance indicators. Although the strong correlation between SN Ia peak luminosity and light curve decline rate was found purely empirically (Pskovskii, 1977; Phillips, 1993), the physics underlying this relation has been extensively studied (Höflich et al., 1995, 1996; Kasen & Woosley, 2007). There is hope that improved physical understanding and modeling of SN Ia explosions, coupled with larger high-quality observational data sets, will lead to improved distance estimates from SNe Ia. As part of this program, deeper understanding of the nature of the progenitor systems can help

narrow the range of initial conditions that need to be explored in carrying out the costly simulations of SN Ia explosions that in principle predict their photometric and spectroscopic properties.

Measurement of the SN Ia rate may also have a more direct impact on the determination of systematic errors in SN Ia distance estimates. Mannucci et al. (2006); Scannapieco & Bildsten (2005); Neill et al. (2006) and Sullivan et al. (2006b) have argued that a two-component model of the SN Ia rate, in which a prompt SN component follows the star formation rate and a second component follows the total stellar mass, is strongly favored over a single SN Ia channel. In this picture, since the cosmological star formation rate increases sharply with lookback time, the prompt component is expected to dominate the total SN Ia rate at high redshift. Mannucci et al. (2006) and Howell et al. (2007) pointed out that this evolution with redshift can be a potential source of systematic error in SN Ia distance estimates, if the two populations have different properties. In order to test such a model for the evolution of the SN Ia rate, improved measurements of the rate as a function of redshift and of host galaxy properties are needed.

In this thesis, I present new measurements of the SN Ia rate based on the SDSS-II Supernova Survey. The SDSS-II Supernova Survey (Frieman et al., 2008b) offers several advantages for this measurement. It covers a larger spatial volume than previous SN surveys, a result of the combination of intermediate-scale (2.5-m) telescope aperture, wide field of view (3 square degrees), modest effective sidereal exposure time (54 sec), and use of drift-scanning to efficiently cover a large sky area ($\sim$ 300 square degrees). The SDSS-II Supernova Survey is a rolling search, with new SNe discovered simultaneously with the follow-up of previously discovered SNe. Unlike SN searches that target known galaxies, the SDSS-II Supernova Survey is not biased against finding SNe in low-luminosity host galaxies. Well-calibrated photometry in

the SDSS *ugriz* passbands (Fukugita et al., 1996), with a typical interval between observations of four days, yields well-sampled, multi-band light curves that enable photometric typing of SNe with high confidence. Moreover, rapid on-mountain photometric reduction and image processing coupled with an extensive spectroscopic follow-up program enable spectroscopic confirmation of a very high fraction of the low-redshift SN Ia candidates.

In this thesis I will give a detailed description of the SDSS-II Supernova Survey, as it relates to studies of the type Ia SN rate, and discuss three separate SN rate studies. The SN rate studies described herein are additionally being published in Dilday et al. (2008), Dilday et al. (2008a), and Dilday et al. (2008b).

In Chapter 2 I will elaborate on the technical aspects of the SDSS-II SN Survey. In Chapter 3 I will provide a brief overview of the SN sample obtained by the SDSS. In Chapter 4 I will discuss measurements of the low-redshift volumetric type Ia SNe rate and discuss implications of these measurements for SN progenitor models. In Chapter 5 I will discuss measurements of the redshift dependence of the type-Ia SN rate from the SDSS-II Supernova Survey. In Chapter 6 I will discuss measurements of the type Ia SN rate in galaxy clusters. I will conclude in Chapter 7.

CHAPTER 2

THE SDSS-II SUPERNOVA SURVEY OBSERVATIONS

In this Chapter I describe the SDSS-II Supernova Survey observations and SN search program. As was mentioned in Chapter 1, the SDSS-II Supernova Survey offers several advantages for making precise measurements of the SN rate, and a description of the SN Survey is necessary to provide some context for the SN discovery efficiency studies and selection functions that will be discussed in Chapters 4-6. The observations of the SDSS-II Supernova Survey were carried out during the Fall months (Sept. 1- Nov. 30) of 2005-2007. A summary of the observations is given in Table B.1. Additionally, a half-scale "engineering" run of the SDSS-II SN Survey was carried out in the Fall of 2004 (Sako et al., 2005). Although the SNe discovered in 2004 are less densely sampled than the SNe from the SDSS-II Supernova Survey, and the SN yield represents a marginal contribution to the total SNe discovered by the SDSS-II Supernova Survey, the engineering run did serve as an opportunity for developing the data-processing software and the SN search algorithms. In that regard, the 2004 run was an extremely important component in the success and high yield of SNe of the SDSS-II Supernova Survey. Some of the lessons learned from the 2004 engineering run will be mentioned below.

2.1 Photometric Observations

The SDSS-II Supernova Survey was carried out on the 2.5m telescope (Gunn et al., 2006) at Apache Point Observatory (APO), using a wide-field CCD camera (Gunn et al., 1998) operating in time-delay-and-integrate (TDI, or drift scan) mode. Observations were obtained nearly simultaneously in the SDSS *ugriz* filter bands (Fukugita et al., 1996).

The SDSS-II Supernova Survey covered a region, designated stripe 82, centered on the celestial equator in the Southern Galactic hemisphere, bounded by $-60^\circ < \alpha_{J2000} < 60^\circ$, and $-1.258^\circ < \delta_{J2000} < 1.258^\circ$. Stripe 82 has been imaged multiple times in photometric conditions by the SDSS-I survey and co-added images from those runs provided deep template images and veto catalogs of variable objects for the SDSS-II Supernova Survey transient search. Due to gaps between the CCD columns on the camera, each stripe in the SDSS is divided into northern (N) and southern (S) *strips*; the SDSS-II Supernova Survey alternated between the N and S strips on subsequent nights. Each strip encompasses $\sim$ 162 square degrees of sky, with a small overlap between them, so that the survey covered $\sim$ 300 square degrees. On average each part of the survey region was observed once every four nights during the SDSS-II Supernova Survey.

Figure 2.1 shows the sky coverage versus survey time for the 2005 observing season, along with a representative SN Ia light curve.

2.2 SN Search Pipeline and Algorithms

There are five main components to the supernova search pipeline: photometric reduction, image subtraction, automated object selection, visual inspection, and light curve fitting for spectroscopic target selection. We describe them briefly in turn. For a full night of imaging data, the entire pipeline ran in approximately 20 hours, sufficient for keeping up with the data flow and for rapid spectroscopic targeting.

In the first stage of the search pipeline, the imaging data was acquired from the camera and processed through the the SDSS photometric reduction pipeline, known as `PHOTO` (Lupton et al., 2001). `PHOTO` produces "corrected" images that are astrometrically calibrated (Pier et al., 2003) and provides a local estimate of the point

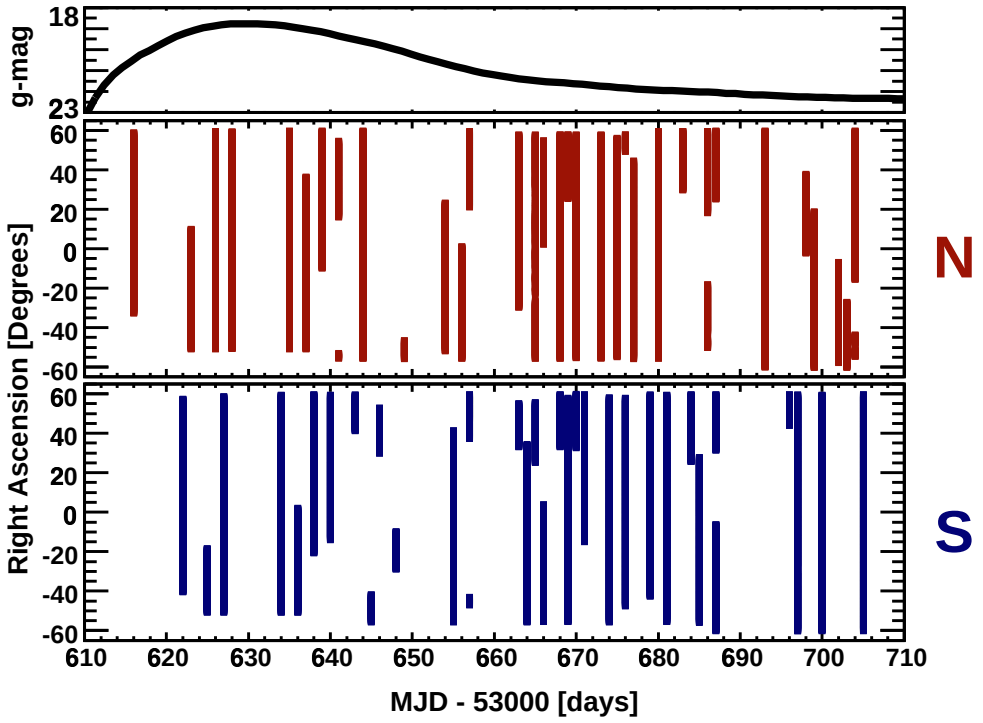

Figure 2.1: Right ascension range covered by SDSS-II Supernova Survey imaging runs vs. epoch for the 2005 observing season. The panels labelled N & S denote the Northern and Southern strips of stripe 82. The regions $\alpha_{J2000} < -51^\circ$ and $\alpha_{J2000} > 57^\circ$ are not covered early in the season, and these regions are suppressed from the rate measurement. The top panel shows an example unextincted g-band light curve for a SN Ia at a redshift of 0.12, based on the MLCS2k2 model.

spread function (PSF). In the second stage, images were processed through a difference imaging pipeline, which was derived from the `PHOTPIPE` software used in previous transient searches (Smith et al., 2002), but was modified to work effectively with the SDSS data. To run the search pipeline to completion in less than a day with the available on-mountain computing resources, only the corrected *gri* images were processed beyond the first stage. In the difference imaging pipeline, the search image was astrometrically and photometrically registered to the template image, and the template image was convolved with a kernel chosen to minimize subtraction residuals (Alard

& Lupton, 1998). A difference image was then obtained by subtracting the convolved template image from the survey image. Peaks were detected in the difference image using the `DoPHOT` photometry and object detection package (Schechter et al., 1993). The signal-to-noise threshold for object detection is at ~ 3.5, corresponding in typical conditions to $g \sim 23.2$, $r \sim 22.8$, and $i \sim 22.5$. The typical magnitudes at signal-to-noise of 10 for point-like objects are $g \sim 21.8$, $r \sim 21.5$, and $i \sim 21.2$.

The third stage of the SN search pipeline comprised a sequence of automated filtering operations that select events of potential interest from among those detected in the difference images. We required a close positional match (within 0.8") in at least two of the *gri* images, which removed cosmic rays, single-band spurious noise fluctuations, and a large fraction of asteroids and other rapidly moving objects detected by the survey. All detections that satisfy these criteria were entered into a `MySQL` database and are referred to as *objects*. To reject active galactic nuclei (AGN) and variable stars, we vetoed any detection occurring at the position of a previously cataloged variable, using observations of stripe 82 from several previous years. The area corresponding to previously cataloged variable objects represents $\sim 1\%$ of the total survey area.

In addition to SNe, the database of detected objects includes a variety of physical and non-physical transients. Physical sources include slow-moving asteroids that were not rejected by the moving object veto, AGN and variable stars not already cataloged, and high proper-motion stars. Non-physical sources include improperly masked diffraction spikes from bright stars and artifacts of imperfect image registration. To remove non-physical sources, cut-out images of all objects that remained after the automated filtering were visually inspected and classified in the fourth stage of the search pipeline. The visual inspection and classification of transient detections is referred to as *handscanning*. To make the handscanning process convenient,

a webpage interface was developed that displayed images of the object along with information on the current detection, and on any previous detections at the same coordinates. An example of the webpage interface for handscanning is shown in Figure 2.2. For each object that was scanned by a human, the scanner was presented with a list of choices for classification of the object as follows:

- **None**

  Object does not appear to be an authentic astrophysical transient. Often objects classified as none are marginally above the detection threshold and are indistinguishable from noise.

- **Artefact**

  Artifacts of the subtraction process. Generally diffraction spikes from bright stars that extend across 2 frames and are therefore not properly masked out.

- **Moving**

  Object appears to be moving. Generally there is an apparent offset between the detections in the g and r filters, which are the 2 most widely separated filters on the SDSS camera (observations occur ≈ 358.5 secs apart).

- **Saturated Star**

  A bright star which did not subtract cleanly.

- **Dipole**

  An object with adjacent regions of positive and negative subtraction residuals (i. e. a dipole configuration). Generally objects in this category are the core regions of bright galaxies or stars, where imperfect PSF matching can result in residuals that have a large absolute magnitude, relative to the statistical noise.

- **Variable**

  Object appears to be near the center of a star-like (as opposed to galaxy-like) object. Additionally, the object may have detections that span across several years, which is strongly suggestive that the object is not a SN.

- **Transient**

  An object that does not have any apparent host galaxy but is not obviously a moving object.

- **Cosmic Ray**

  A sharply defined transient detection that has an extent much less than the PSF. In practice the requirement of a matching detection in at least 2 filters removes cosmic rays, and this category is almost never used.

There are 4 categories of SN candidate. The 'Gold', 'Silver', 'Bronze' nomenclature was originally devised as a subjective ranking system for SN candidates. However, following the 2004 engineering run, a set of more rigorous definitions was implemented. In all cases a SN classification implies that the object has the appearance of a SN (i. e. a point source), and does not fall into any of the categories of background listed above.

- **SN Gold**

  Object is associated with, and is well separated from, a galaxy-like object. The object shown in Figure 2.2 is a prototypical example of a SN Gold.

- **SN Silver**

  Object has no host galaxy, but is not a moving object. In most cases a SN Silver is an object that was classified as a "transient" on its first epoch.

- **SN Bronze**

  Object is associated with, and is near the center of, a galaxy-like object. Detections of AGN are generally classified as SN Bronze.

- **SN Other**

  Object has features inconsistent with a normal SN, but is nevertheless an interesting astrophysical transient. Including this category allows us to keep a record of objects that may prove to be of interest, but that are not necessarily of high priority for immediate spectroscopic observation.

Objects visually classified as one of the SN classes were flagged for further analysis and are denoted *candidates*. Subsequent object detections in difference images at the same position were automatically associated with the same candidate. Allowing for distinction between different classes of background objects was useful in developing the autoscanner software as discussed below. The distribution of classifications is given in Table 2.1.

In the fifth and final stage of processing for the SN search, the *gri* light curve for each SN candidate was fit to models of type-Ia, type-Ib/c and type-II SNe. The non-Ia SN models consist of template light curves constructed from photometric measurements of individual SNe provided by the SUSPECT database[1], coupled with the corresponding SN spectral model provided by Nugent et al. (2002). For the SN Ia model, a stretch and a wavelength-dependent scale factor was applied to a fiducial bolometric light curve in a way designed to reproduce the Δm_{15} parameterization of the peak-luminosity/decline-rate relation (Hamuy et al., 1996). The time of maximum, Δm_{15}, redshift, and extinction parameter A_V (magnitudes of extinction in the V-band) are fit parameters that were searched on a grid for the set of values

1. http://bruford.nhn.ou.edu/~suspect/index1.html

Table 2.1. Distribution of scanning types

Type	2005 Number (%)	2006 Number (%)	2007 Number (%)
none	52555 (33.77)	1460 (10.12)	2194 (16.12)
artefact	16325 (10.49)	4578 (31.73)	3048 (22.39)
moving	10205 (6.56)	661 (4.58)	1056 (7.76)
sat. star	1488 (0.96)	292 (2.02)	186 (1.37)
dipole	15966 (10.26)	1913 (13.26)	1620 (11.90)
variable	14090 (9.05)	235 (1.63)	99 (0.73)
transient	20247 (13.01)	1102 (7.64)	964 (7.08)
cosmic ray	338 (0.22)	— (0.0)	3 (0.02)
SN Gold	4132 (2.66)	760 (5.27)	859 (6.31)
SN Silver	864 (0.56)	400 (2.77)	701 (5.15)
SN Bronze	17069 (10.97)	2702 (18.72)	2389 (17.55)
SN Other	2337 (1.50)	327 (2.27)	494 (3.63)

that produce the minimum value of the χ^2 statistic. This procedure is referred to as *color-typing*. For some candidates, we additionally carried out difference imaging in the u and z passbands in order to better distinguish Type II and Type Ia SNe that tend to have a significantly different $u-g$ color at early epochs. To further constrain the early light curve shape, we carried out forced-positional photometry on difference images at the position of the candidate in pre-discovery images. The relative goodness of fit of candidate *gri* light curves to SNe Ia and core-collapse SNe models was used as a factor in prioritizing spectroscopic follow-up. In particular, all SN Ia candidates found before peak and with estimated current r-band magnitude $\lesssim 20$ were placed on the spectroscopic target list, and our follow-up observations were nearly complete out to that magnitude. Since the typical peak magnitude for a SN Ia with no extinction at redshift $z = 0.1$ is $r \simeq 19.3$, we might expect that the spectroscopic SN Ia sample should be essentially complete out to roughly this redshift as well; we shall

see later that this is the case. This photometric pre-selection of SNe Ia proved very effective: approximately 90% of the candidates initially targeted as SNe Ia after two or more epochs of imaging resulted in a SN Ia spectroscopic confirmation. The SDSS-II Supernova Survey photometric classification and spectroscopic target selection are discussed in full detail in Sako et al. (2008).

2.2.1 Autoscanner

During the 2005 SN observing season we took a conservative approach and hand-scanned every object that was detected in 2 of the *gri* filters and was not coincident with a known AGN or variable star. In the course of the 3-month observing season, this resulted in $\approx 150,000$ objects being handscanned, which required a substantial time commitment from the SN team members. To reduce the number of objects to be scanned by humans and thereby improve the efficiency of the SN survey, prior to the 2006 season we implemented a new software filter, called the *autoscanner*. The software performs two primary tasks: 1) identifies all objects detected in more than one epoch as well as bright (g or $r < 21$ mag) objects detected for the first time, and 2) uses statistical classification techniques to identify and filter out first-epoch background non-SN objects.

The reasons for performing 1) are as follows. First, the selection of objects detected in more than one epoch provides a very robust way of eliminating moving objects, one of the major contaminants of the 2005 SN candidates. Second, the selection of bright first-epoch objects enabled us to discover nearby SNe; we could thereby obtain spectroscopic observations well before maximum light and provide rapid alerts to the SN community. In addition, bright, single-epoch candidates provided a back-up list of spectroscopic targets for nights when the spectroscopy queue was not filled by

promising multi-epoch candidates. Although most of our targets were spectroscopically observed after two or more epochs of photometry, in a few instances, we did obtain spectroscopic observations of SN candidates based on a single epoch of detection. In the selection of these objects, the autoscanner also identified and flagged objects associated with either a known variable in the veto catalog or a known SN candidate. In each case these objects were not handscanned, but the new photometric observations are used in the light curve analysis.

For 2), the autoscanner attempted to identify and filter out bright first-epoch objects that belong to one of three classes of background; unmasked diffraction spikes, artifacts of imperfect image registration (dipoles), and moving objects. The autoscanner software treats the set of objects, along with their evaluations by a human, from the 2005 search as a training set, and compares the observed quantities for newly detected objects against this set. The method used to classify an object is the *histogram method of probability density function (PDF) estimation* (e. g. Webb (2002)). In this method the observable quantities, or attributes, of an object form a multi-dimensional space, and a classification decision is made by considering the number count of objects, in the training set, from each class in a bin centered at the point describing the object we wish to classify. This method has the advantages of being non-parametric, allowing the decision boundaries in the observable space to be arbitrarily complicated, and of explicitly retaining the correlations between observables. A caveat of using the histogram method of PDF estimation is that one must have a sufficient number of objects in the training set to sample the PDF well in all regions of interest. With $\approx 90,000$ objects in the training set, this is not a significant limitation for the SDSS-II SN Survey. A technical discussion of the algorithm is presented below.

During the 2006 and 2007 observing seasons, the autoscanner was used to reject moving objects from among the set of bright first-epoch objects that were to be

handscanned. For such bright objects, only $\approx 0.7\%$ of them are incorrectly tagged as moving objects by the autoscanner. We initially chose not to reject objects classified as artifacts or dipoles from the handscanning as they are a small fraction of the background in comparison to moving objects, and the relatively small reduction in handscanning that would be accomplished was determined to be outweighed by the risk of missing an early epoch of a nearby SN. However, a comparison of the objects classified by the autoscanner as artifacts during the 2006 observing season to their human classification shows that the autoscanner is extremely efficient at recognizing artifacts, and that our concern about potentially rejecting nearby SNe was overly cautious. During the 2006 observing campaign, 3753 objects had been classified by the autoscanner as artifacts. Humans classified 2668 of these objects as artifacts and 3710 of them as some type of non-SN background. Of the remaining 43 objects classified by a humans as SN candidates, 41 were background (non-SN) events erroneously classified by the scanner, one was a bright nova outburst, and one was the first epoch of a SN that was later (after the 2nd epoch detection) classified as a SN. Therefore, in cases where they disagree on classification of artifacts, the autoscanner appears to be more reliable than the human scanners, and during the 2007 season we used the autoscanner to reject objects classified as artifact, and loosened the definition of "bright" first epochs from (r or g) < 21 to (r or g) < 21.5.

This new handscanning strategy and the autoscanner enabled a reduction in the number of objects scanned per year by more than an order of magnitude between 2005 and 2006-2007, with no reduction in the quality or quantity of confirmed SNe. While scanning a single camera column in 2005 typically took $2-3$ hours per person for a full night of data, in 2006-2007 a scanner could cover two columns in only $10-20$ minutes. The reduction in handscanning due to the autoscanner is summarized in Table 2.2. In addition to greatly improving the efficiency for SN discovery by the

Table 2.2. Summary of the 2005-2007 search seasons

Number of	2005	2006	2007
Nights on SDSS 2.5m	59	60	54
Runs	73	90	75
Total number of objects	375,187	391,435	354,397
Number of objects scanned	155,616	14,430	13,613
Number of objects tagged as SN	24,402	4,189	4,443
SN candidates discovered[a]	11,385	3,694	3,968
Single-epoch candidates[b]	6,618	599	1,192
Confirmed SNe Ia	129	192	166
Objects scanned per confirmed SN	1206	75	82

[a]The number of unique SN candidates tagged by a scanner. This number differs from the number of objects tagged as a SN because it includes multiple objects from the same candidate.

[b]Candidates that were detected in only a single run. Most of these sources are likely to be solar system objects.

SDSS-II Supernova Survey, such automated transient classification algorithms will be crucial for efficiently prioritizing the much higher yield of transients expected from up-coming transient surveys such as LSST.

2.2.2 Autoscanner Algorithm

As a further illustration of the histogram method of PDF estimation, we note that Bayes' theorem, applied to classification, says that,

$$\frac{P(c_i|\theta)}{P(c_j|\theta)} = \frac{P(\theta|c_i)P(c_i)}{P(\theta|c_j)P(c_j)} \tag{2.1}$$

where $P(a|b)$ is the conditional probability for a given b, c_i represents object class i, and θ denotes particular values for the set of observables of an object. If this ratio is

larger than one, then the object is more likely to belong to class i than to class j.

Applied to the problem at hand, this can be written as,

$$\frac{P(c_i|\theta)}{P(c_j|\theta)} = \frac{(N_i'/N_i)(N_i/N)}{(N_j'/N_j)(N_j/N)} = \frac{N_i'}{N_j'} \tag{2.2}$$

where N_i is the total number of objects in the training set belonging to class i, N is the number of total objects in the training set, and a $'$ denotes objects possessing observables θ. The θ represents a subset of all possible observables, which is equivalent to marginalizing over all other observables, and the set used differs according to which class of background is being tested.

The criterion used by the autoscanner to identify objects of class i is,

$$\frac{N_i'}{N_j'} > \frac{N_i}{N_j} \tag{2.3}$$

where i represents the classes of background (artifact, mover, dipole), and class j is always taken as SN. The motivation for this criterion is that we are searching for an *overdensity* of objects of class i in the region of observable space in question. In practice the threshold, N_i/N_j above, is a free parameter that can be adjusted to control the relative level of accepted signal to background events.

In this experiment, background events dominate over SNe epochs by a large factor, and a Bayesian classifier would reject SN epochs that lie in a reasonable region of the observable space if the region overlaps with background events, even far away from the peak of the background distribution. A cartoon of the situation is shown in Figure 2.3. Thus, the autoscanner can also be regarded as a Bayesian classifier where the thresholds are adjusted *a priori* to mitigate false negatives, at the cost of more background in the scanning.

The training set for the autoscanner consists of all objects from the 2005 observing season that were ranked by a human as an artifact, a dipole, a moving object, or a SN. This set is composed of 91220 total objects, of which 65576 are a sub-class of background, and 25644 are objects ranked as a SN. The quantities used for classification of artifacts are, a measure of the objects ellipticity, the signal-to-noise ratio, and the value of the reduced χ^2 when fitting the object to a model of the PSF. In computing the χ^2, we do not account for possible uncertainty in the PSF model and so objects with large signal-to-noise values also have large χ^2 values. Therefore, in classifying artifacts it is important to retain the correlation between χ^2 and signal-to-noise ratio. The quantities used for classifying dipoles are the measured flux in negative valued pixels, and the ratio of measured flux in negative valued pixels to the flux in positive valued pixels. The quantities used for classifying moving objects are the measured magnitudes, the magnitude of the apparent motion between different filters, and an angle describing the apparent motion between filters. If the object has a detection in the 3 filter-bands *gri*, then the angle is the angle between the "vector" that describes the apparent motion between the r and i filters, and the "vector" that describes the apparent motion between the i and g filters. If the object is truly moving then these apparent motions should be nearly collinear. If the object is only detected in 2 of the *gri* filters then the angle is the angle between the apparent motion between the 2 filters and the "unit vector" aligned in the direction of increasing right-ascension. Main-belt asteroids typically have an apparent motion in a fixed direction, and using this angle in the classification is a way to encode that information. Considering not only the magnitude of the apparent motion between filters, but also the direction, allows the autoscanner to identify relatively slowly moving objects.

2.2.3 VOEvent Network

Beginning with the 2006 observing season, SN candidates discovered by the SDSS-II Supernova Survey were distributed to the astronomical community via the VOEvent network (Williams & Seaman, 2006). All candidates with ≥ 2 detections by the SN search pipeline were sent as alerts to the subscribers to the VOEvent network, and a database of alerts was maintained as part of the SDSS-II Supernova Survey operations. The alerts were automated as a daily cronjob. This was an important contribution to the infrastructure development for a fully automated transient detection pipeline.

2.3 Artificial Supernovae

To measure the SN rate, it is clearly important to understand the efficiency of the survey for discovering SNe. As part of normal survey operations, we inserted artificial SNe Ia (hereafter fakes) directly into the corrected survey images after the photometric reduction (`PHOTO`) but before difference imaging. The primary motivation for inserting fakes into the data stream was to provide real-time monitoring of the performance of the survey software pipeline and of the human scanning of objects. The fakes provide quantitative information about the efficiency of the survey software, human scanning, and the photometric classification of SNe Ia that is useful in the rate determination. Here we describe the basic algorithm for generating fakes and inserting them into the data stream.

A fake is a pixel-level simulation of a point source with a light curve chosen to closely represent that of a real SN Ia. At each epoch for which the fake has a chance of being detected, the calculated CCD signal for the fake is directly added to the survey image. For each observing season, we generated a library of fake light curves: each fake light curve is assigned a position, redshift, date of peak luminosity (in V-band),

and an intrinsic luminosity that correlates with decline rate. We generated ≈ 1000 fakes during the 2005 season and ≈ 2000 fakes during each of the 2006 and 2007 seasons. This resulted in $\sim 7,800$ fake epochs during the 2005 season, and $\approx 25,000$ for each of 2006 and 2007. For each season, the redshift distribution for the fakes was generated by assuming that the number of SNe Ia is roughly proportional to the volume element, $(dN/dz) \propto z^2$, in the range $0.0 < z < 0.4$.

To model the effect of contamination from host galaxy light on the detection efficiency, each fake is placed near a galaxy selected from the photometric redshift catalog (Oyaizu et al., 2008) for SDSS imaging on stripe 82. A host galaxy is drawn at random, from a distribution proportional to the r-band luminosity, from galaxies which have a photometric redshift within ~ 0.01 of the redshift assigned to the fake.

The SN Ia light curve model used to generate *ugriz* magnitudes for a fake at each epoch is the same model that is used for early light curve fitting and photometric typing on the imaging data, but with the light curve parameters now chosen from an input probability distribution. To generate a point-source image from the ideal magnitudes, we use the estimate of the PSF from `PHOTO` at the position of the fake at the given epoch. We obtain the conversion from magnitudes to instrumental units (analog-to-digital units, or ADU) by running the `DoPHOT` photometry package on a set of cataloged stars in the survey image for which the magnitudes have been previously measured by the SDSS. After scaling the PSF model to match the computed ADU flux, we add Poisson fluctuations to each pixel. Finally, the row and column in the field that correspond to the position of the fake are taken from the astrometric solution provided by the imaging pipeline, and the fake is overlaid on the survey image.

When a fake is detected in the difference images, its identity as a fake is kept hidden while it is scanned by humans. After scanning, the fakes are revealed so that they are not mistakenly targeted for spectroscopic follow-up and so that the efficiency

of scanners in tagging fakes as SN candidates can be monitored. However, like all candidates, fakes are processed through the automated light curve fitter/photometric typing algorithm so that we can test if they are accurately typed as SNe Ia after a few photometric epochs. The use of the fakes for measuring the survey detection efficiency is discussed in § 4.3.1. Additional technical details on the generation of fakes are presented in Appendix A.

2.4 Spectroscopic Observations

The classification of SNe is defined by their spectroscopic features. In addition, spectroscopy provides a precise redshift determination and, in a number of cases, host galaxy spectroscopic-type information. Spectroscopic follow-up of the SDSS-II Supernova Survey candidates was undertaken by a number of telescopes, including the Hobby-Eberly 9.2m at McDonald Observatory, the Astrophysical Research Consortium 3.5m at Apache Point Observatory, the William-Herschel 4.2m, the Hiltner 2.4m at the MDM Observatory, the Subaru 8.2m and Keck 10m on Mauna Kea, and the SALT 11m at the South African Astronomical Observatory.

The classification of SN spectra is performed by comparing the spectral data to normal and peculiar supernova spectral templates from the work of Nugent et al. (2002) and to a public library of well-measured supernova spectra (Matheson et al., 2005; Blondin & Tonry, 2007). The SN typing in this work is in many cases based on visual inspection of the spectra, but was guided by applying the cross-correlation technique of Tonry & Davis (1979) to the spectrum and the template library. The visual inspection relies heavily on the characteristic SN Ia features of Si and S absorption, which are usually prominent at optical wavelengths for this redshift range. The SDSS-II Supernova Survey defines 2 categories of SNe Ia; those that are considered to

be identified securely as SNe Ia, and those that are considered probable SNe Ia based on analysis of their spectra. These are referred to as "Ia" and "Ia?", respectively. The classifications as "Ia" and "Ia?" are somewhat subjective, but are guided by statistics of the cross-correlation analysis.

The redshift determination is based on galaxy features when they are present; otherwise SN features are used. In some cases, particularly at low redshift, a high-quality spectrum of the SN host galaxy is available from the SDSS-I spectroscopic survey. Comparison with those spectra indicate that our follow-up spectroscopic redshifts are determined to an accuracy of ~ 0.0005 when galaxy features are used and ~ 0.005 when SN features are used. Further details of the SDSS-II Supernova Survey spectroscopic analysis, with application to the first-year data, are presented in Zheng et al. (2008).

2.5 Final Photometry

To obtain more precise SN photometry than the on-mountain difference imaging pipeline provides, we re-process the imaging data for all spectroscopically confirmed and other interesting SN candidates through a final photometry pipeline (Holtzman et al., 2008). In this "scene-modeling photometry" (SMP) pipeline, the supernova and the host galaxy (the *scene*) are modeled respectively as a time-varying point-source and a background that is constant in time, both convolved with a time-varying PSF. This model is constrained by jointly fitting all available images at the SN position, including images well before and after the SN explosion. Since there is no spatial resampling or convolution of the images that would correlate neighboring pixels, the error on the flux can be robustly determined. The SMP pipeline often provides photometric measurements at additional epochs compared to the survey operations

pipeline. The final analysis of SN light curves discussed in this paper is based on SMP; in particular, the selection cuts described in §4.2 are made using the SMP pipeline.

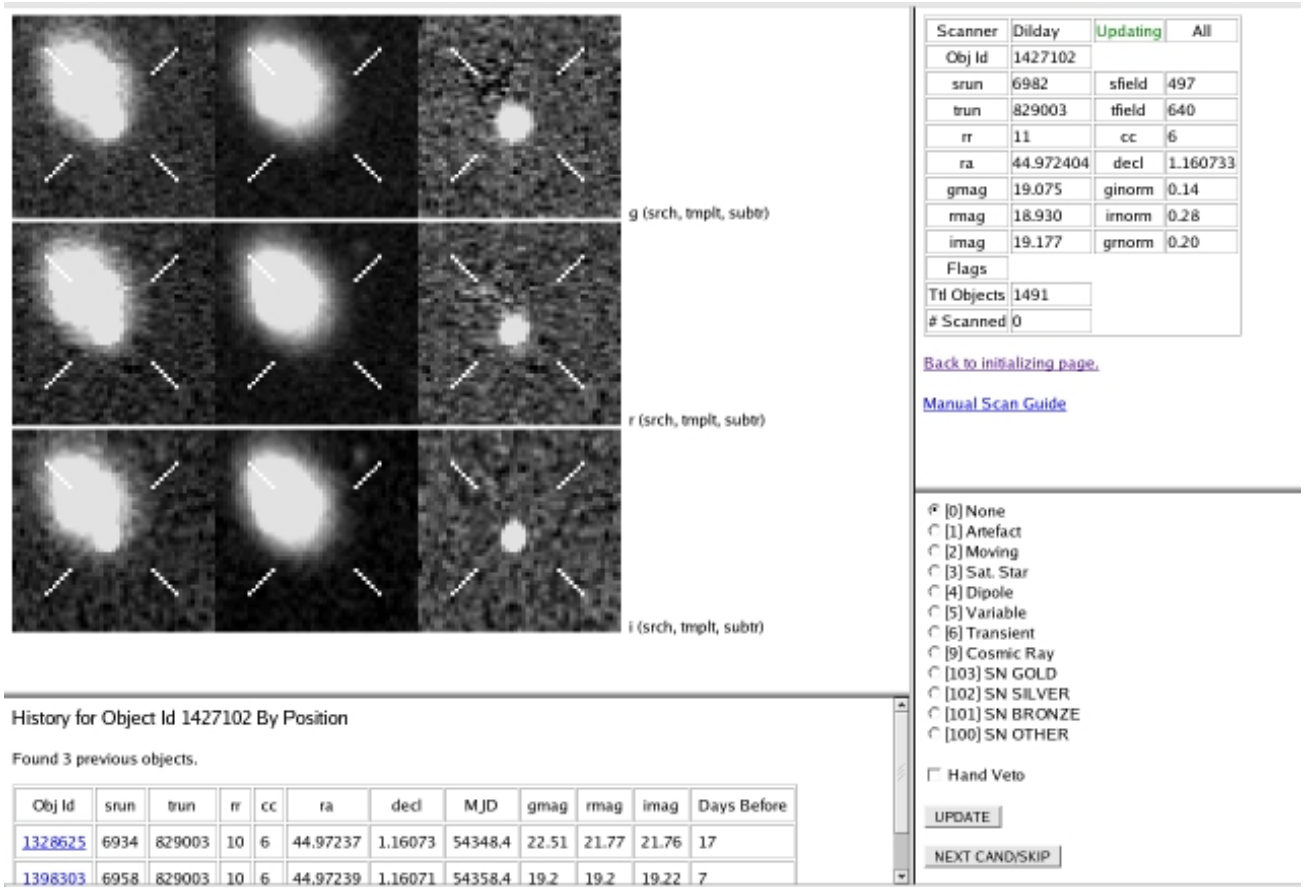

Figure 2.2: Example of the handscanning web interface. In the top left panel the search (left column), template (middle column) and difference (right column) images are shown for g (top row), r (middle row), and i (bottom row). The bottom left panel shows information on any previous detections of a transient object at the same sky position (within 0.8"). The top right panel displays summary information on the present detection of the object. The bottom right panel contains a set of choices for the human evaluation of the object.

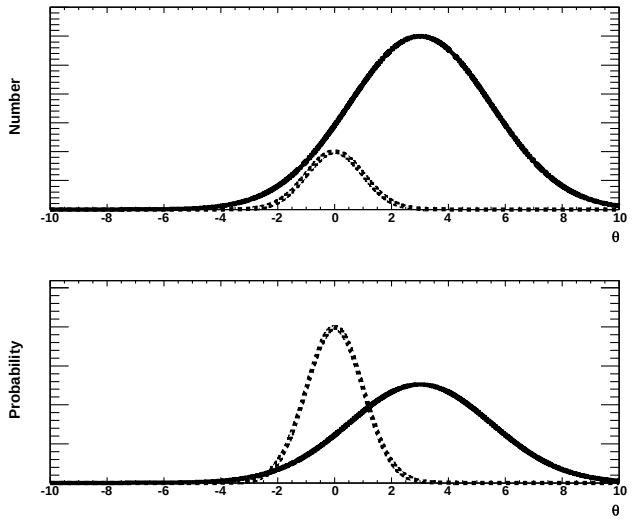

Figure 2.3: Hypothetical distributions of an observable for signal (dashed) and background (solid). The peak of the signal occurs at 0; however, the vastly greater number of background events swamps the signal. While it is true that an object with a value of this observable of 0 is more likely to be a background event, this is clearly not the behavior we want from our classifier, as we are trying to isolate the relatively rare signal events (i.e. SN epochs). The bottom panel shows the effect of recasting the problem from one of relative probabilities to one of overdensities. The peak of the signal (dashed) is now strongly inconsistent with background.

CHAPTER 3

THE SDSS-II SUPERNOVA SURVEY SN SAMPLE

The observing strategies and SN search program described in §2 resulted in a very successful campaign for discovering SNe. During its 3 3-month observing seasons, the SDSS-II Supernova Survey discovered ≈ 500 spectroscopically confirmed SNe Ia. This includes 498 SNe with a spectroscopic "Ia" designation and 51 SNe with a "Ia?" designation (see §2.4). It is possible that improved spectroscopic analysis techniques may change the spectroscopic designation in a few cases. A count of known SNe Ia is difficult to precisely determine, but inspection of the database of SNe publicly announced through the International Astronomical Union (IAU) circulars [1] suggests that this may be as much as $\approx 15-20\%$ of all SNe Ia discovered since 1885. The SDSS-II Supernova Survey also discovered 18 type Ib/c and 61 type II SNe.

In addition to spectroscopically identified SNe Ia, the SDSS-II Supernova Survey has identified and measured light curves for several hundred SN candidates for which a spectroscopic confirmation of type was not possible. This spectroscopic incompleteness is primarily due to limited spectroscopic resources, but in some cases spectra were obtained that were indeterminate for SN typing due to , e. g. low signal-to-noise on the observation. To improve the utility of these objects for SN rate determinations, for investigation of the demographics of astrophysical transients, and for possible use in future cosmological analysis, efforts are underway to precisely measure host galaxy redshifts. At present the SDSS-II Supernova Survey has obtained ≈ 200 host galaxy redshifts for these photometric SN candidates.

The SDSS-II Supernova Survey SN discoveries were routinely announced via the IAU circulars and the Central Bureau for Astronomical Telegrams (CBET)

1. http://www.cfa.harvard.edu/iau/lists/Supernovae.html

(Adelman-McCarthy et al., 2005; Barentine et al., 2005j,e,a,b,c,d,i,f,g,h; Bassett et al., 2006y,a,b,c,d,e,f,g,h,i,j,k,l,m,n,o,p,q,r,s,t,u,v,w,x, 2007p,o,a,b,c,d,e,f,g,h,i,j,k,l,m,n).

The spectroscopically confirmed SNe Ia from the SDSS-II Supernova Survey are listed in Table B.2. An image gallery of 484 confirmed SNe Ia with designations by the IAU is shown in Figure 3.1.

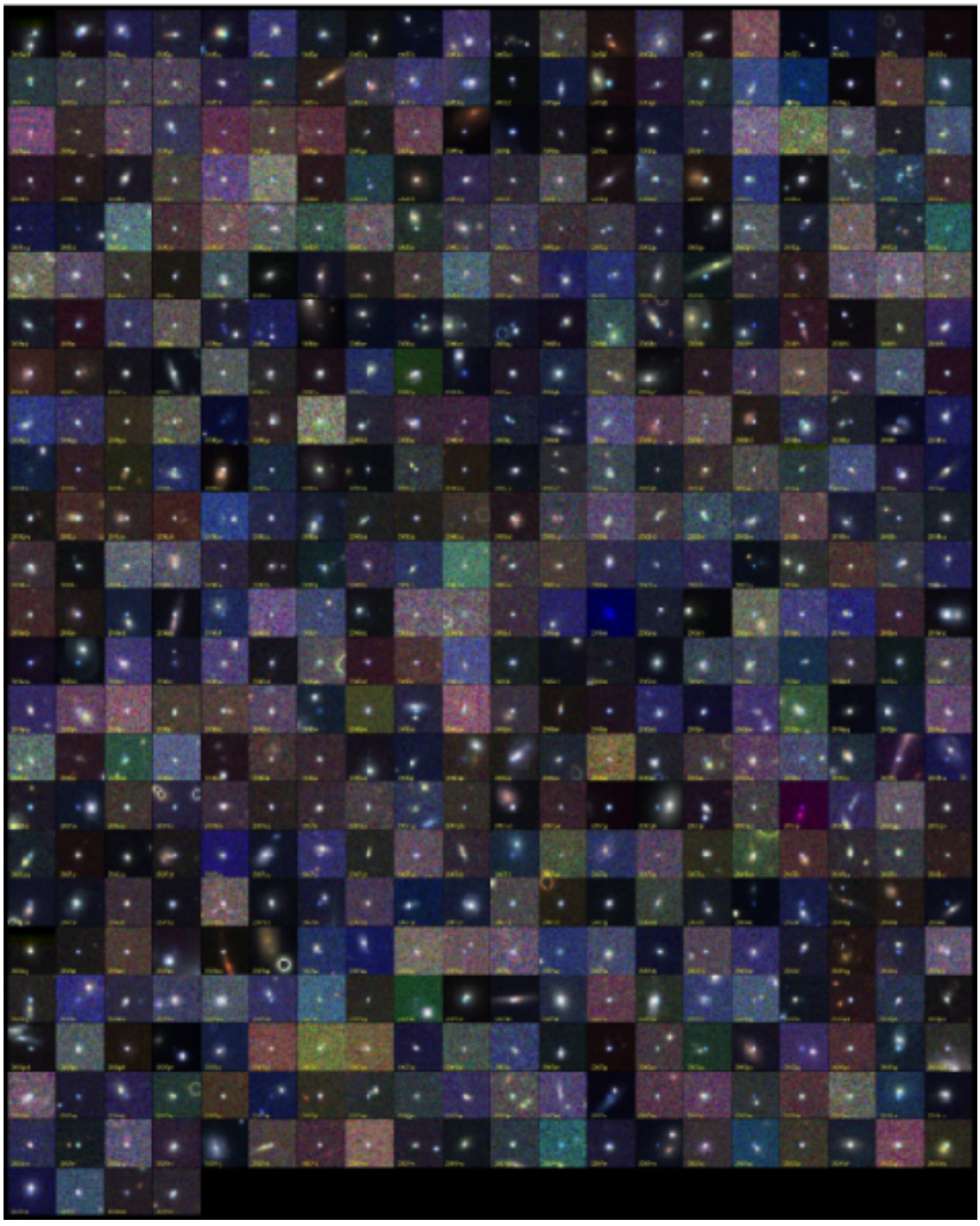

Figure 3.1: 484 Spectroscopically confirmed SDSS SNe Ia from 2005- 2007, with designation by the International Astronomical Union (IAU).

CHAPTER 4

THE LOW-REDSHIFT SN RATE

4.1 Introduction and Review of Previous Measurements

In this Chapter I will discuss measurement of the low-redshift type Ia SN rate, based on a highly pure sample of SNe Ia with a well determined selection function. At low redshifts ($z \sim 0.1$), SN Ia rate measurements (Cappellaro et al., 1999; Hardin et al., 2000; Madgwick et al., 2003; Blanc et al., 2004) have suffered from small sample sizes and also from systematic errors associated with heterogeneous samples (Cappellaro et al., 1999) and with selection biases due to the targeting of known, relatively luminous galaxies (Hardin et al., 2000; Blanc et al., 2004). The low-redshift measurement of Madgwick et al. (2003), based on SNe discovered fortuitously in SDSS galaxy spectra, is affected by different systematic uncertainties than traditional photometric searches, e.g., due to the finite aperture of the SDSS spectroscopic fibers.

While the SDSS-II Supernova Survey was carried out over three three-month seasons, during Sept.-Nov. 2005-7, the results presented in this Chapter are based on the Fall 2005 season, as presented in Dilday et al. (2008). The SDSS-II Supernova Survey measures light curves for SNe Ia to redshift $z \simeq 0.4$, with a median redshift of $\langle z \rangle = 0.22$ for spectroscopically confirmed SNe Ia. However, in this analysis we limit the analysis to low redshift, $z \leq 0.12$, since the SDSS-II Supernova Survey spectroscopic follow-up is essentially complete over this redshift range, and the uncertainty due to spectroscopically unobserved (and untyped) SNe is therefore negligible. In presenting a SN Ia rate measurement, one must decide whether to include peculiar SNe Ia, i.e., events that are photometrically and/or spectroscopically unusual, since it is not clear that they are members of the same population as the "normal" SNe

Ia. Formerly, the peculiar designation included events such as 1991T and 1991bg, which are highly overluminous and underluminous events, respectively. However, since these SNe appear to follow the standard peak-luminosity/decline-rate relation, they are now generally considered extreme members of the normal SN Ia population (Nugent et al., 1995). Other events, such as 2002ic (Hamuy et al., 2003) and 2002cx (Li et al., 2003), exhibit more pronounced peculiarities and do not fit the luminosity-decline relation. The first season of the SDSS-II Supernova Survey included two such truly peculiar events at low redshift, 2005hk (Phillips et al., 2007) and 2005gj (Prieto et al., 2007; Aldering et al., 2006). Although these peculiar events may arise from the same evolutionary path as normal SNe Ia, which would argue for including them in a SN Ia rate measurement, we have chosen to include only SNe with light curves that obey the standard brightness-decline relation. More specifically, we include in our rate measurement sample only SNe with light curves that are well described by the MLCS2k2 SN Ia light curve model (Riess et al., 1996; Jha et al., 2007), see §4.2.1. Regardless of the physical arguments surrounding peculiar events, we exclude them from this analysis primarily because we do not yet have a robust determination of our efficiency for detecting them.

4.2 Defining the SN Ia Sample for the Rate Measurement

The SN Ia sample for the rate measurement must include all SNe Ia in the redshift range of interest, not just those for which we have a confirming spectrum. Although the SDSS-II Supernova Survey has high efficiency for discovering and spectroscopically confirming low-redshift SNe Ia (§4.2.1), we can take advantage of our rolling search data to carry out an extensive post-season hunt for SNe Ia that may have been missed by the search pipeline during the survey season (§4.2.2).

4.2.1 Spectroscopic SN Sample

In its first season (Fall 2005), the SDSS-II Supernova Survey discovered 130 events with secure spectroscopic identifications as SNe Ia[1] and 16 events that are considered probable SNe Ia based on their spectra. For SN Ia events satisfying the selection criteria below, the spectroscopic follow-up is essentially complete for redshifts $z \leq 0.12$, so we have chosen to focus on this redshift range for this measurement of the SN rate. For $z \leq 0.12$, the sample contains 27 spectroscopically confirmed SNe Ia and 2 spectroscopically probable SNe Ia before making selection cuts.

For the measurement of the SN Ia rate, we impose a number of selection criteria on the SN photometric data, with the aim of producing a sample that has a well-characterized selection function. These criteria are applied to the spectroscopically confirmed and probable SNe Ia with $z \leq 0.12$. For consistency, we will also apply these selection cuts to the photometric (i.e., spectroscopically unconfirmed) SN sample discussed in §4.2.2. The selection cuts for the rate measurement are as follows:

1. $-51^\circ < \alpha_{J2000} < 57^\circ$.

   Although the SDSS-II Supernova Survey covers the RA range $-60^\circ < \alpha_{J2000} < 60^\circ$, early in the Fall 2005 observing season we did not have complete templates available for the regions $\alpha_{J2000} < -51^\circ$ and $\alpha_{J2000} > 57^\circ$, so these RA regions were not initially used for the SN search, as shown in Fig. 2.1. In principle, we could account for this by modeling the time-varying effective search area, but for simplicity we choose to excise these RA regions from the rate measurement. Furthermore, the calibration star catalog used by our final photometry pipeline (Ivezić et al., 2007) does not extend below $\alpha_{J2000} \sim -51^\circ$, and we cannot

1. The classification of 2005gj as a SN Ia may be controversial (Prieto et al., 2007); as noted in §4.1, we exclude it from this analysis.

presently simulate light curves for SNe in this region. This cut removes one confirmed SN Ia, 2005iu, from the rate sample.

2. There are photometric observations on at least five separate epochs between -20 days and $+60$ days relative to peak light in the SN rest-frame.

   Peak light refers to the date of maximum luminosity in the SN rest-frame B-band according to the best-fit MLCS2k2 light curve model. This cut requires that the light curve is reasonably well-sampled and it is primarily useful for photometrically distinguishing SNe Ia from other SN types with high confidence when there is no SN spectrum available (see §4.2.2). Here and below, a photometric observation simply means that the survey took imaging data at that epoch on that region of sky and that SMP reported a SN flux measurement (not necessarily significant or even positive) with no error flags (see Holtzman et al. (2008)) in at least one of the three *gri* passbands. It does *not* imply a detection above some signal-to-noise threshold. One SN discovered late in the observing season, 2005lk, fails this cut.

3. At least one epoch with signal-to-noise ratio > 5 in each of g, r, and i (not necessarily the same epoch in each passband).

   This cut ensures that there are well-measured points on the light curve, and is mainly useful for rejecting low signal-to-noise events from the photometric sample. All spectroscopically confirmed SNe Ia in the low-redshift sample satisfy this cut.

4. At least one photometric observation at least two days *before* peak light in the SN rest frame.

5. At least one photometric observation at least ten days *after* peak light in the

SN rest frame.

These two cuts require sampling of the light curve before and after peak light, ensuring that we have a precise determination of the time of peak light. These cuts also help remove non-SN Ia contaminants from the photometric sample (see §4.2.2). Finally, they guarantee that the epoch of peak light occurs during our observing season, i.e., between Sept. 1 and Nov. 30, which is one of the criteria used in defining the rate measurement in §4.4. Since these cuts are *more* restrictive than the requirement of peak light during the observing season, they are the main contributors to the inefficiency estimated in §4.3.2. These are the most restrictive cuts on the spectroscopic SN Ia sample, together removing nine events: four SNe Ia discovered early in the observing season do not have a pre-maximum observation, and five SNe Ia found late in the season do not have a photometric observation more than ten days past peak light.

6. MLCS2k2 light curve fit probability > 0.01.

The MLCS2k2 light curve fitter (Riess et al., 1996; Jha et al., 2007) takes as input the measured SN magnitudes in each passband at each epoch, and the measured SN redshift; it then finds the likelihood as a function of the four parameters μ (the distance modulus), A_V (the extinction parameter), the time of peak light in rest-frame B-band, and the light curve shape/luminosity parameter Δ. The MLCS2k2 fit probability is defined by evaluating the usual χ^2 statistic for the data and the best fitting MLCS model and assuming that this statistic obeys a χ^2_{n-4} probability distribution, where n is the number of photometric data points. The model parameters of the best fitting MLCS2k2 model are defined as the mean of the probability distribution for each corresponding parameter. This cut on the fit probability provides an automated method of

removing photometrically peculiar SNe Ia from the sample. We find that essentially all of the spectroscopically normal SNe Ia in our confirmed sample have a fit probability > 0.1. However, the spectroscopically confirmed SN Ia sample is likely to be biased toward "high-quality" light curves, so we place the selection cut at a less restrictive value. Three spectroscopically identified SNe Ia are rejected by this cut, including the peculiar SNe 2005hk (χ^2/d.f. = 90/21) and 2005gj (χ^2/d.f. = 198/45). The third rejected SN, with internal SDSS candidate designation 6968 (χ^2/d.f. = 78/27), was classified as a spectroscopically probable SN Ia (see §2.4) and shows some evidence of being spectroscopically similar to 2005hk. For the sample of photometric SN candidates (§4.2.2), this cut helps remove non-SN astrophysical variables, such as AGN and M stars.

7. MLCS2k2 light curve fit parameter $\Delta > -0.4$.

   The MLCS parameter Δ is a measure of the light curve shape and intrinsic luminosity. Smaller values of the Δ parameter correspond to more slowly-declining, intrinsically brighter SNe Ia. This cut requires that Δ be consistent with the values observed for the low-redshift SNe Ia that were used to train the MLCS2k2 light curve fitter. For the photometric SN candidates, this cut helps reject Type II supernovae, which often have a long plateau after the epoch of peak luminosity and result in large negative fitted values of Δ.

Placing the above selection requirements results in the 16 spectroscopically identified SNe Ia that are listed in Table 4.1. This sample includes 2005je, which was classified as spectroscopically probable. The spectroscopically confirmed SNe Ia that are removed from the rate-measurement sample are listed in Table 4.2; the last column indicates which of the above selection criteria was used to remove each SN.

Table 4.1. SNe Ia included in the rate sample.

SDSS Id	IAUC Designation	α (J2000.0)	δ (J2000.0)	Redshift	Redshift Source
1241	2005ff	22 30 41.41	−00 46 35.7	0.088	SN
1371	2005fh	23 17 29.71	+00 25 45.8	0.120	galaxy
2561	2005fv	03 05 22.42	+00 51 30.1	0.119	galaxy
3256	2005hn	21 57 04.23	−00 13 24.4	0.107	galaxy
3592	2005gb	01 16 12.58	+00 47 31.0	0.086	galaxy
3901	2005ho	00 59 24.10	+00 00 09.3	0.063	galaxy
5395	2005hr	03 18 33.81	+00 07 24.3	0.117	SN
5549	2005hx	00 13 00.13	+00 14 53.7	0.120	SN
5944	2005hc	01 56 47.94	−00 12 49.1	0.046	galaxy
6057	2005if	03 30 12.87	−00 58 28.5	0.067	galaxy
6295	2005js	01 34 41.51	−00 36 19.4	0.084	SN
6558	2005hj[a]	01 26 48.40	−01 14 17.3	0.057	—
6962	2005je	02 35 26.61	+01 04 29.6	0.094	galaxy
7147	2005jh	23 20 04.42	−00 03 19.8	0.109	galaxy
7876	2005ir	01 16 43.80	+00 47 40.7	0.076	galaxy
8719	2005kp	00 30 53.15	−00 43 07.9	0.117	galaxy
9266[b]	—	03 20 43.16	−01 00 07.2	0.036	galaxy

[a]SN type confirmed by Quimby et al. (2005)

[b]Photometrically identified SN Ia. See §(4.2.2)

Note. — SDSS Id denotes internal candidate designation.

Table 4.2. Spectroscopically confirmed SNe Ia with $z \leq 0.12$ cut from the rate sample.

SDSS Id	IAUC Designation	α (J2000.0)	δ (J2000.0)	Redshift	Cut Index
722	2005ed	00 02 49.37	+00 45 04.6	0.086	4
739	2005ef	00 58 22.87	+00 40 44.6	0.107	4
774	2005ex	01 41 51.24	−00 52 35.0	0.093	4
2102	2005fn	20 48 53.04	+00 11 28.1	0.095	4
4524	2005gj	03 01 11.95	−00 33 13.9	0.062	6
6773	2005iu	20 20 15.61	+00 13 02.5	0.090	1
6968	—	01 18 13.37	−00 54 23.6	0.098	6
8151	2005hk	00 27 50.88	−01 11 53.3	0.013	6
10028	2005kt	01 10 58.04	+00 16 34.1	0.066	5
10096	2005lj	01 57 43.03	−00 10 46.0	0.078	5
10434	2005lk	21 59 49.43	−01 11 37.3	0.103	5,2
10805	2005ku	22 59 42.61	−00 00 49.3	0.045	5
11067	2005ml	02 14 04.42	−00 14 21.1	0.119	5

Note. — SDSS Id denotes internal candidate designation. See section 4.2.1 for explanation of cut index.

4.2.2 Photometric SN Sample

In addition to the spectroscopically identified SNe Ia discussed above, the survey has measured light-curves for a few thousand variable objects per year, including possible SNe, for which we did not obtain a classifiable spectrum while the source was bright enough to identify. We refer to these spectroscopically unobserved or unclassified objects as *photometric SN candidates*. There are a number of reasons for such spectroscopic incompleteness, including limited spectroscopic resources, targeting errors (e.g., misplacement of a spectroscopic slit), poor weather either preventing spectroscopic observations or rendering them indeterminate, and possible inefficiencies in the spectroscopic target selection algorithm. In order to make a reliable SN Ia rate measurement, we must investigate the photometric SN candidates to determine the level of incompleteness, if any, of the spectroscopic SN Ia sample. This is a challenge, because a sample of purely photometric SN Ia candidates may be heavily contaminated by objects that are not SNe Ia, especially if there are significant numbers of objects with multi-band light curves that are not too dissimilar from those of SNe Ia. The combination of selection cuts listed in §4.2.1 is designed to meet this challenge, by rejecting the majority of non-SN Ia contaminants. In addition to the spectroscopically confirmed and spectroscopically probable SNe Ia discussed above, the SDSS-II Supernova Survey discovered 16 low-redshift SNe that were spectroscopically confirmed as non-Ia SNe in its first year. As a check that our selection cuts are effective at rejecting non-Ia SNe, we apply the same cuts to this sample of 16 low-redshift ($z < 0.2$) spectroscopically confirmed non-Ia SNe. All but one of these non-Ia SNe are rejected by these selection cuts. The selection criteria above could be made more restrictive in order to reduce potential non-Ia contamination of the photometric SN sample. For example, by requiring a photometric observation at least 16 (as opposed

to 10) days after peak light in the SN rest frame, the spectroscopic non-Ia SN above would be eliminated from the sample. However, we find that such a change would have no impact on the selection of photometric SN candidates for inclusion in the rate sample.

To determine whether any of the photometric SN candidates are genuine SNe Ia in the redshift range of this rate measurement, we must estimate both the SN type and redshift for each candidate. There are two categories of photometric SN candidates, (a) those for which we have a precise spectroscopic measurement of the redshift and (b) those for which we do not. The redshifts for category (a) candidates come from two sources. The first source is the SDSS-I spectroscopic galaxy survey, which measured redshifts for $\sim 28,000$ galaxies in our survey region at redshifts $z \leq 0.12$. The second source is from subsequent spectroscopic observations of ~ 80 host galaxies of the highest-quality photometric SN candidates; these spectra were obtained in the summer and fall of 2006 and 2007. Using the sample selection process described below in §4.2.2, we found in our imaging data only one photometric SN Ia candidate that passes the selection criteria in §4.2.1 and that has a spectroscopic redshift $z \leq 0.12$ (category (a)). The host galaxy of this SN Ia candidate, which has internal SDSS SN designation 9266, has a spectroscopic redshift of $z = 0.0361$ measured by the SDSS galaxy redshift survey. This object was not targeted for spectroscopic follow-up during the SDSS-II Supernova Survey because it has very high extinction, $A_V \simeq 4$ according to the MLCS2k2 fit. This extinction value lies outside the range of the A_V-search grid for the photometric typing algorithm used during the search (§2.2).

Redshift estimation for photometric SN candidates

For each photometric SN candidate *without* a spectroscopically determined redshift (category (b) above), we must estimate both the redshift and the SN type from the photometric data. We do this using a modification of the standard MLCS2k2 light curve fit, in which the redshift is included as a parameter in the likelihood function. In this instance, the distance modulus μ is *not* treated as a fit parameter; instead, we adopt the concordance LCDM cosmology, with $\Omega_m = 0.3$, $\Omega_\Lambda = 0.7$, and dark energy equation of state parameter $w = -1$, and fix $\mu(z)$ to its functional form for that cosmology. The photometric redshift estimate, z_{phot}, is then obtained by marginalizing over the other fit parameters, i.e., the epoch of peak luminosity, the extinction A_V, and the shape parameter Δ.

Although these SN photometric redshift estimates depend on the assumed cosmology, we do not expect them to be extremely sensitive to the values of the cosmological parameters, especially at the modest redshifts under consideration here. To test the accuracy of these redshift estimates, we applied the MLCS2k2 redshift fit to SNe Ia light curves that have spectroscopically measured redshifts. For this test, we use two sets of objects: (i) all spectroscopically confirmed SNe Ia with redshift $z \leq 0.25$, and (ii) all photometric SN Ia candidates that satisfy the selection criteria in §4.2.1 and that have spectroscopic (host galaxy) redshift $z \leq 0.25$. We include objects in category (ii) because the spectroscopically confirmed SNe Ia could represent a biased sample of the SN Ia population if there are spectroscopic selection biases. We include objects with redshift $z > 0.12$ to yield a more statistically significant test and to check for photometric redshift biases that could cause these objects to be erroneously included in the $z \leq 0.12$ sample. There are 61 and 28 events in categories (i) and (ii), respectively.

The residuals of the SN photometric redshift estimates for this test sample of 89 objects are shown in Figure 4.1. The distributions of the residuals are shown in Figure 4.2 separately for categories (i) and (ii), which indicates that the distributions for the two samples are consistent. The fit residuals for the combined sample are shown in Figure 4.3. For the combined sample, the mean residual of the photometric redshift estimate is consistent with zero. The scatter in the photometric redshift estimate for the combined test sample is $\sigma_z = 0.018$, and Fig. 4.1 shows that the scatter increases with redshift. The distribution of the residuals normalized by the MLCS-reported redshift error is shown in the right panel of Figure 4.3. If the reported redshift errors were accurate and Gaussian, this distribution would be a Gaussian with unit variance, $\sigma = 1$. The distribution appears to be approximately Gaussian, but with measured variance $\sigma = 1.4$; we therefore choose to multiply the MLCS-estimated photometric redshift error for each candidate by 1.4.

In addition to the SN photometric redshift estimates, we also have host galaxy photometric redshift estimates for the majority of photometric SN candidates (Oyaizu et al., 2008). Although the galaxy z_{phot} estimates have larger scatter than those from the SN light curves, in principle we could require consistency between these two redshift estimates as an additional selection cut on the photometric SN sample. Since core-collapse SNe are typically fainter than SNe Ia, they would typically be assigned incorrectly high photometric redshifts by the light curve fitter. Using the existing selection cuts, however, we find no contamination of the rate-measurement sample from the photometric SN candidates without spectroscopic redshifts (see §4.2.2). Therefore a requirement of consistency between the supernova- and galaxy-derived photometric redshift estimates is not necessary in the present analysis.

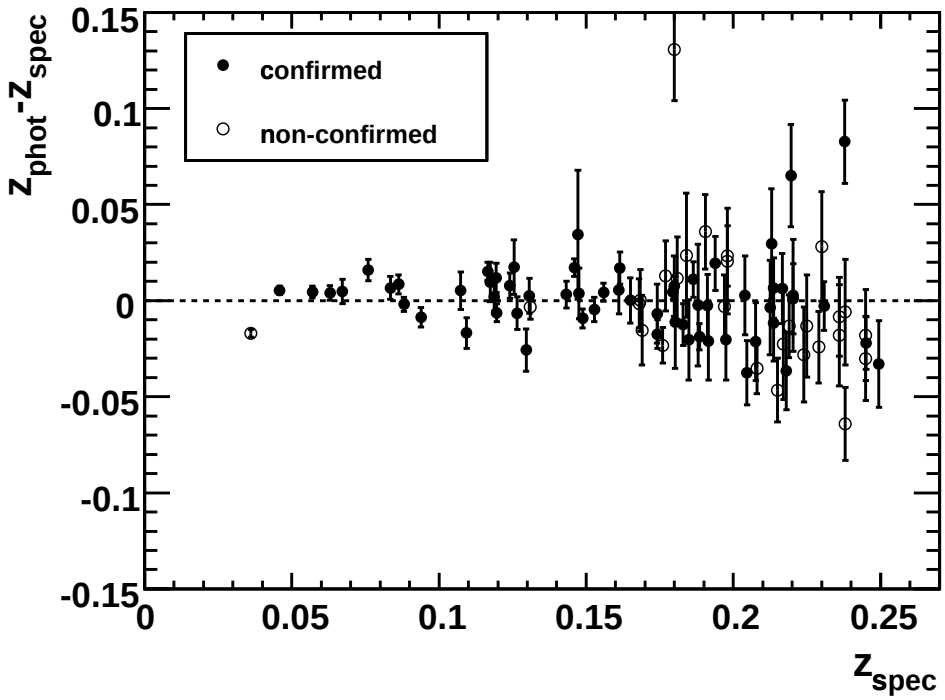

Figure 4.1: Residuals of the photometric redshift estimates, $z_{phot} - z_{spec}$ vs. z_{spec}, for the sample of spectroscopically confirmed and spectroscopically probable SNe Ia (black points) and for the photometric SN Ia candidates that satisfy the rate selection cuts and for which host galaxy redshifts are available (open points). The marginalized redshift errors reported by the MLCS2k2 light-curve fits are shown.

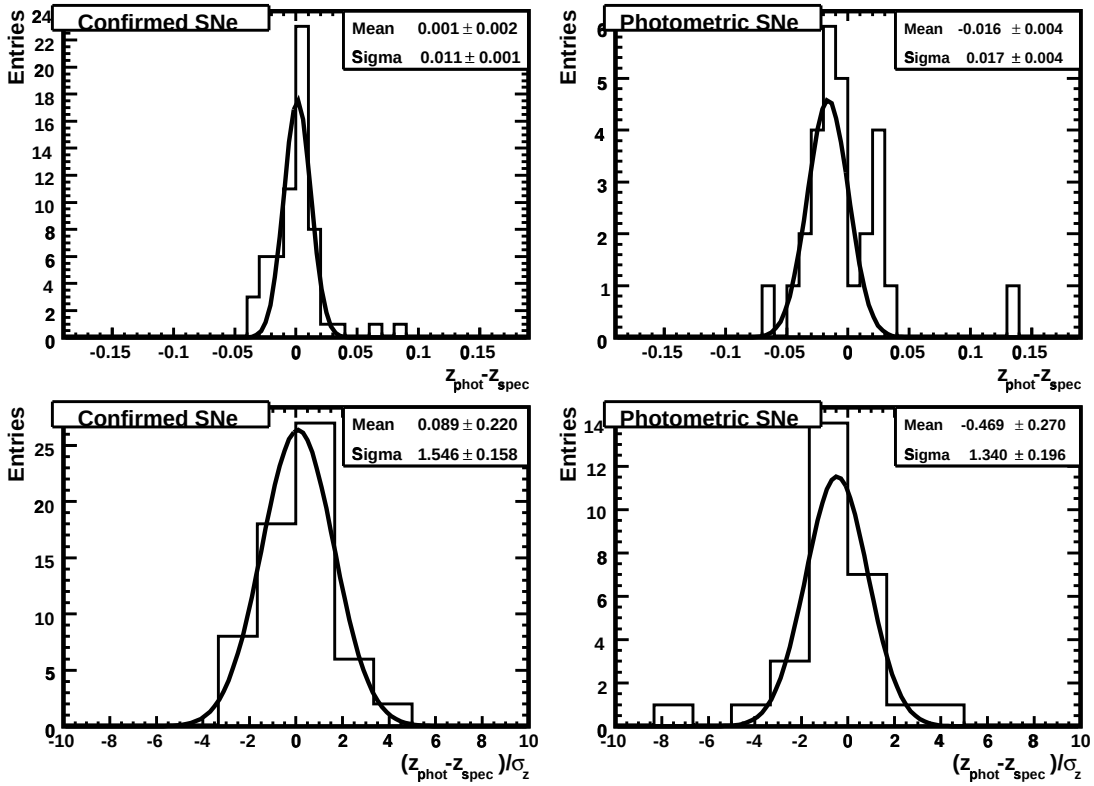

Figure 4.2: The distribution of photometric redshift residuals for the spectroscopically confirmed SNe Ia (left panels) and the photometric SN Ia candidates (right panels) shown in Fig. 4.1. Upper panels show distributions of the difference between the photometric redshift, z_{phot}, and the spectroscopic redshift, z_{spec}; lower panels show distributions of $(z_{phot} - z_{spec})/\sigma_z$, where σ_z is the photometric redshift uncertainty reported by the MLCS2k2 fit. Inset panels show the inferred mean and dispersion of the Gaussian fits to each distribution.

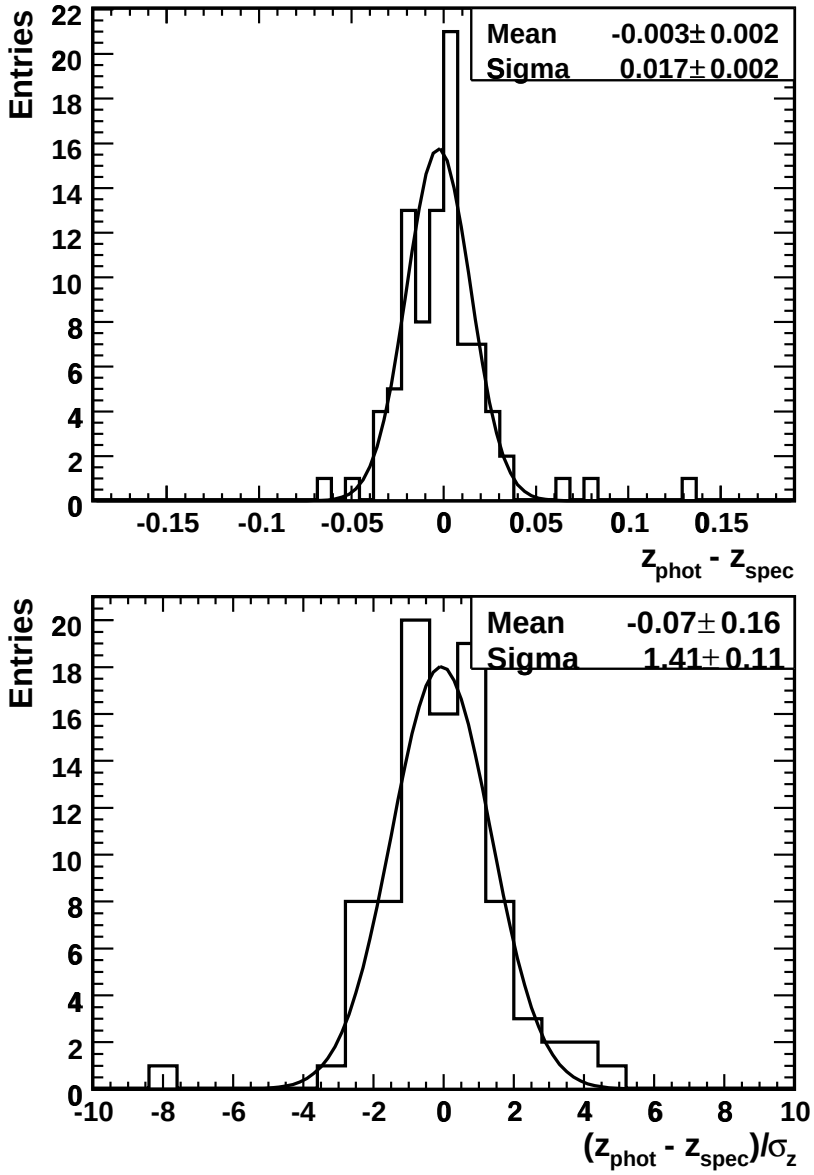

Figure 4.3: *Top panel:* The distribution of photometric redshift residuals, $z_{phot} - z_{spec}$, for the combined spectroscopic+photometric SN Ia samples. z_{phot} is the photometric redshift and z_{spec} the spectroscopic redshift; *Bottom panel:* distribution of residuals normalized by the reported photometric redshift uncertainty, σ_z.

Selection of photometric SN candidates

In the Fall 2005 observing season, the software and human data processing pipeline described in §2.2 yielded 11,385 SN candidates, including the 146 spectroscopically confirmed and probable SNe Ia and 20 that were confirmed as other SN types. The majority of the remaining candidates ($\sim 60\%$) are single epoch events that are most likely to be slow-moving asteroids, leaving ~ 4500 multi-epoch SN candidates. To search for photometric SNe Ia among this large set of candidates, we studied two subsamples selected according to different criteria.

The first photometric subsample is designed to exhaust the list of candidates that are most likely to be SNe Ia. This subsample was selected by choosing all SN candidates that the survey photometric typing code (described in §2.2) classified as SNe Ia[2] and that were detected in at least 3 epochs by the on-mountain software pipeline. The images for the resulting subsample of ~ 420 candidates were processed through the final SMP pipeline, and the resulting light curves were fit with the MLCS2k2 program, using the redshift as a fit parameter in cases where there was no measured host galaxy spectroscopic redshift (the majority of cases). One highly extincted SN Ia (SDSS-SN 9266, discussed in §4.2.2), with a host galaxy redshift measured by the SDSS galaxy survey, was recovered from this subset of photometric SN candidates. No other candidates in this subsample pass the rate selection cuts and have a spectroscopic or SN photometric redshift $z \leq 0.12$.

The second photometric subsample is designed to study the candidates that are less likely to be SNe Ia. This subsample was selected by choosing all SN candidates with detections at more than two epochs during the search and with an estimated time of maximum light, based on the survey photometric typing code, in the twenty-

2. More precisely, according to the photometric typing code, one of the "type A" or "type B" criteria were satisfied; see Sako et al. (2008)

day interval between modified Julian day (MJD) of 53660 and 53680 (October 17 and November 6). Since the selection criteria for this second subsample are looser than for the first (there is no requirement that a SN Ia light-curve template provides the best-fit), the number of candidates it selects would be an order of magnitude larger. Using a restricted time interval provides a manageable number of events to study that are representative of the population of these lower-quality light curves. These selection criteria resulted in 462 candidates, which represent $\sim 1/6$ of the multi-epoch SN candidates that have not already been included in the samples discussed above. We find no events in the second subsample that pass the rate measurement selection cuts and that have a spectroscopic or SN photometric redshift $z \leq 0.12$.

Although no other photometric SN candidates pass our selection criteria, we must allow for uncertainties in the SN photometric redshift estimates from MLCS2k2. In the two photometric subsamples, two candidates that pass the rate-selection cuts have estimated SN photometric redshifts within $\sim 1.5\sigma$ of our cutoff of $z = 0.12$, using the inflated redshift errors discussed in §4.2.2. One of these candidates is from the first photometric subsample and has a fitted redshift 0.17 ± 0.03 (SDSS-SN internal ID 3077); the second is from the second photometric subsample and has a fitted redshift of 0.18 ± 0.04 (SDSS-SN ID 6861). Efforts are underway to obtain spectroscopic redshifts for the host galaxies of these events. Interpreting the (inflated) photometric redshift errors as Gaussian (§4.2.2), the probability that at least one of these two candidates has a redshift $z \leq 0.12$ is significantly less than unity. To be conservative, we assign a systematic uncertainty of +1 SN Ia based on this study.

4.2.3 Summary of Rate Sample Selection

In summary, rate-sample selection requirements have been applied to SN candidates with $z \leq 0.12$ from the 2005 observing season. The resulting sample comprises 16 spectroscopically identified and 1 photometrically identified SNe Ia. These events are enumerated in Table 4.1, and their *gri* light curves are shown in Figure 4.4 along with the best-fit MLCS2k2 model light-curve. Figure 4.5 shows the redshift distribution for SNe Ia from the first year of the SDSS-II Supernova Survey at $z \leq 0.21$; the lowest-redshift photometric candidates with no spectroscopic redshift are in the bin $0.15 < z < 0.18$ and are safely above the redshift cut.

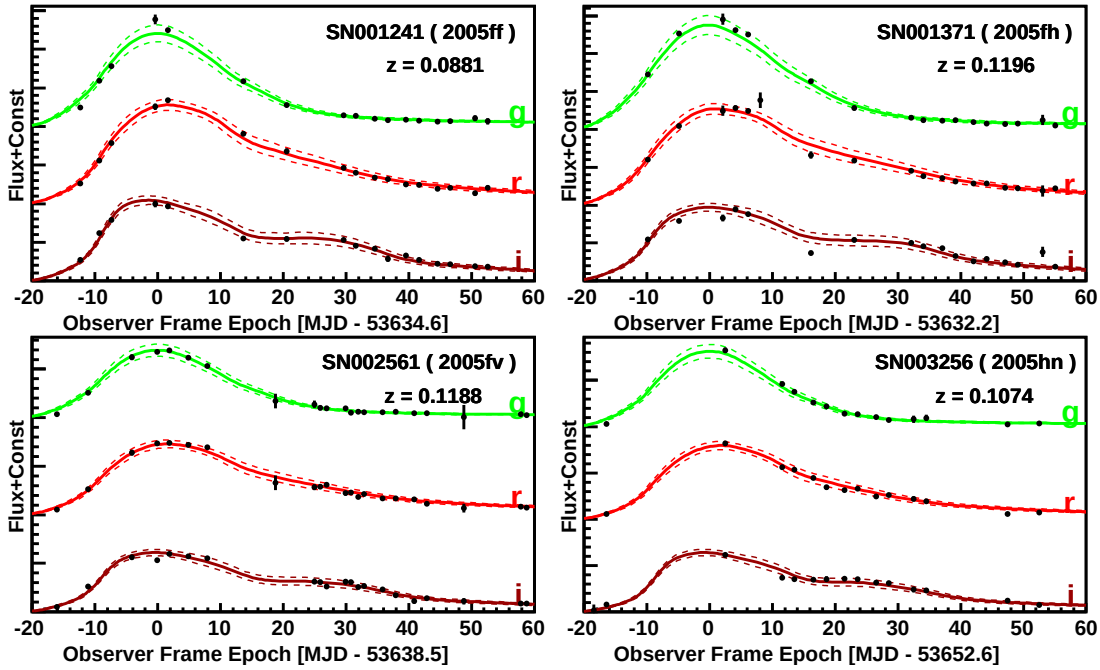

Figure 4.4: *gri* light curves for SNe Ia used in this rate measurement. Black points show the SDSS SN photometry from SMP. The errors on the photometry are shown. Solid curves denote the best-fit SN Ia model light curves in g (green), r (red), and i (dark red) from the MLCS2k2 light-curve fitter, and corresponding dotted curves show the 1-sigma model error range. The curves and data for the different passbands have been vertically offset for clarity. The flux offsets are the same for each SN.

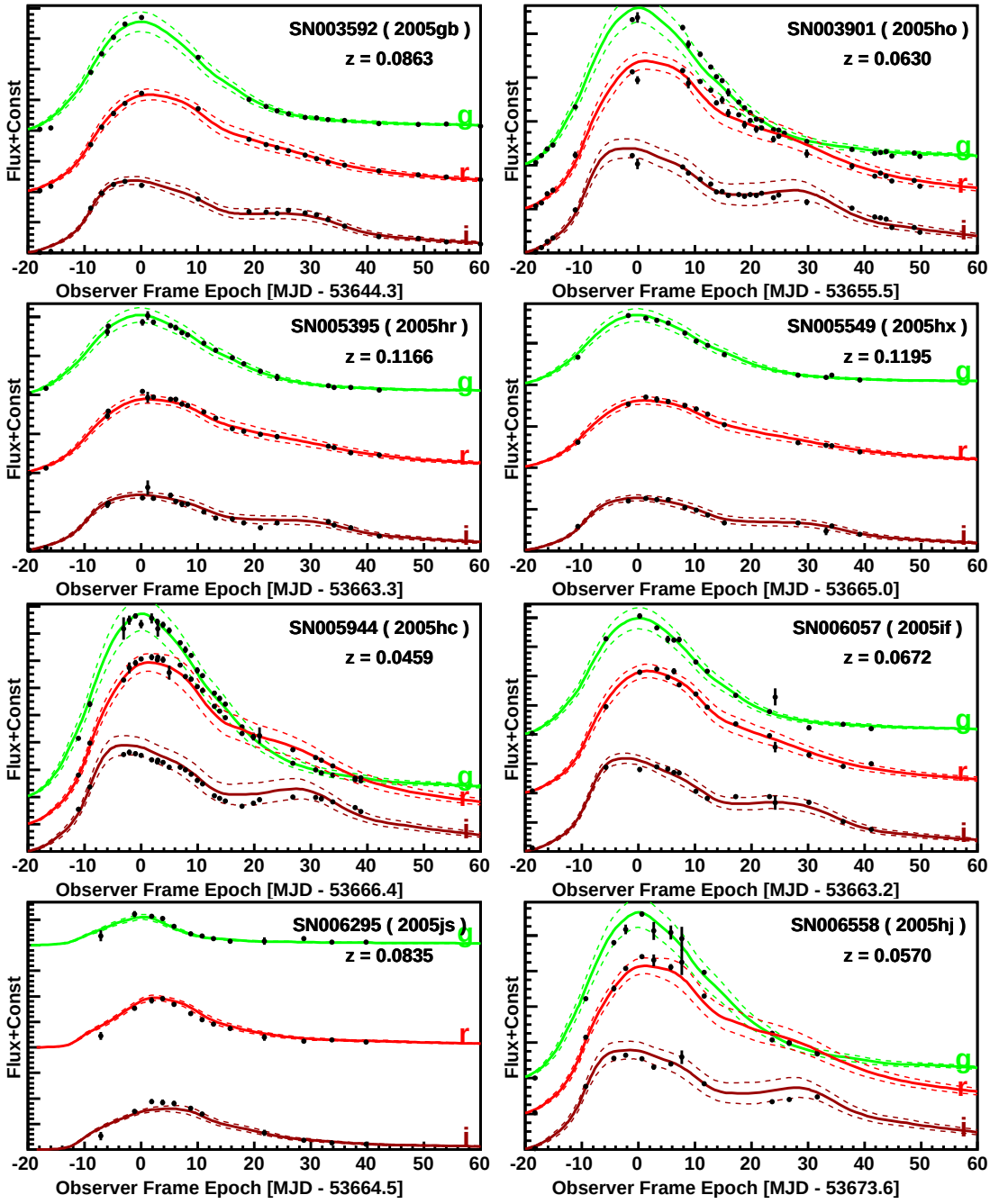

Fig. 4.4 — Continued.

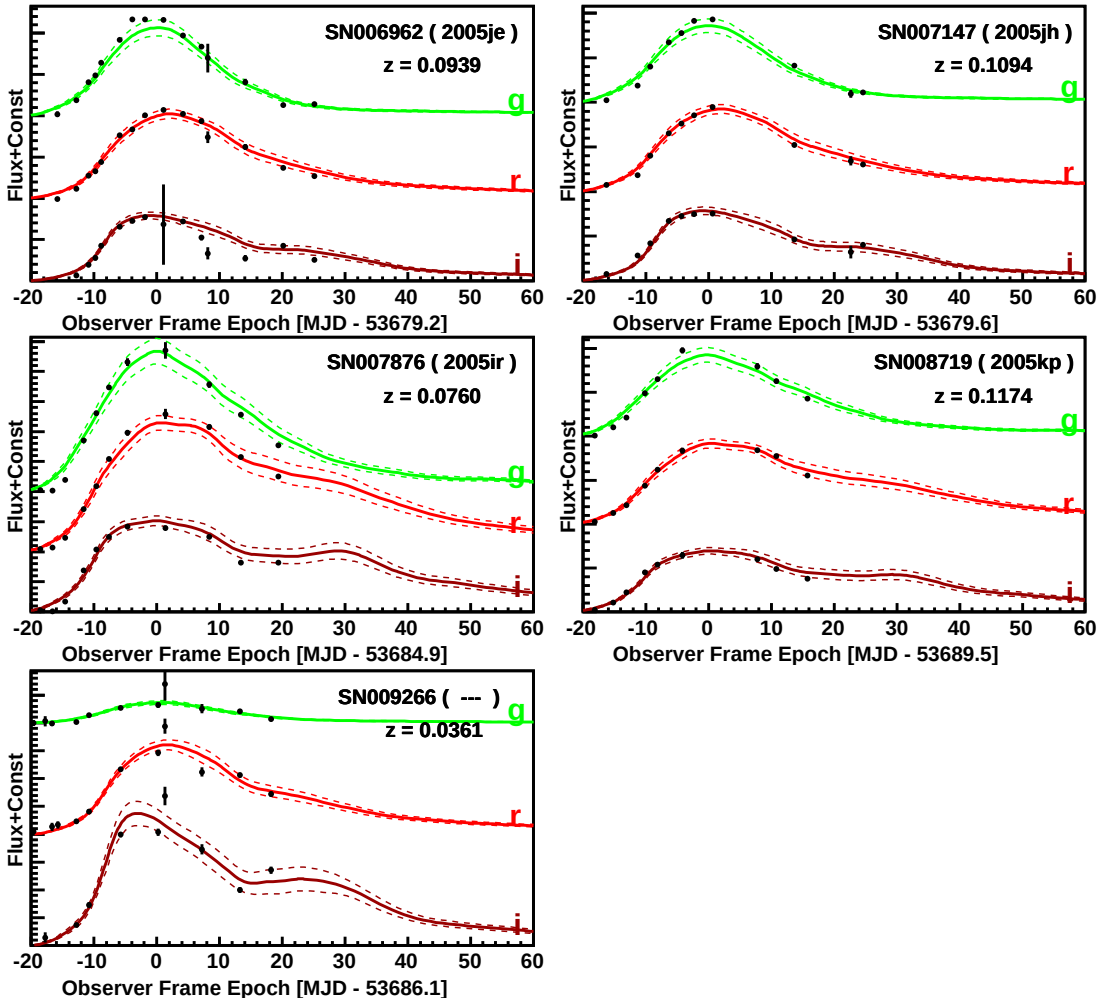

Fig. 4.4 — Continued.

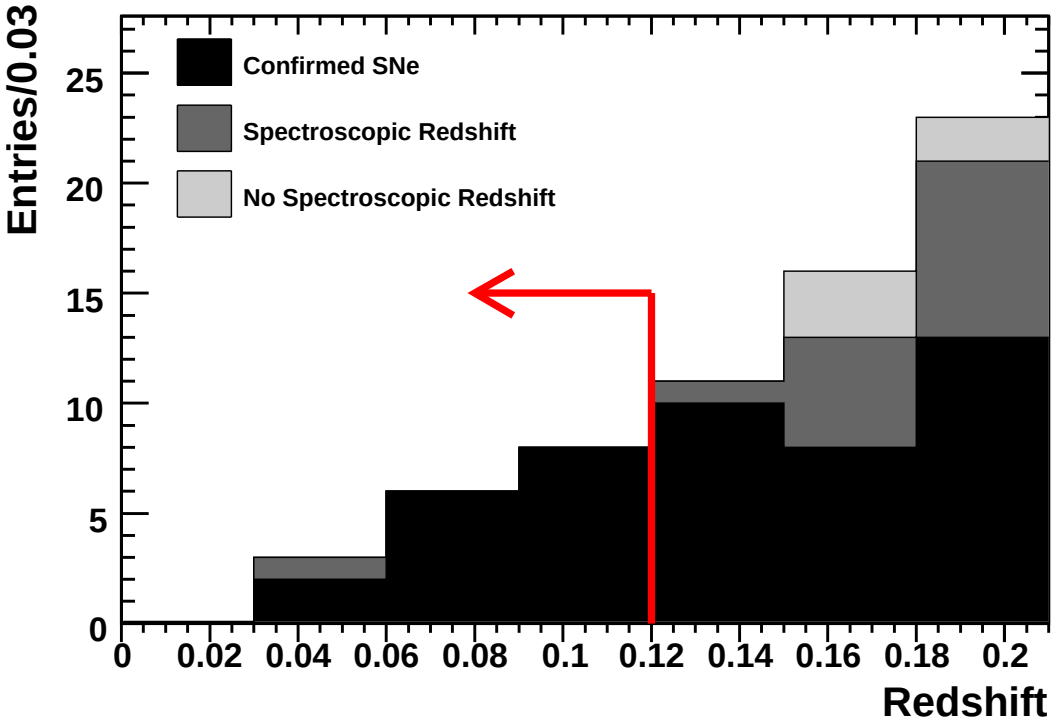

Figure 4.5: Redshift distribution for events passing the rate-measurement selection requirements in §4.2.1. Contributions include: spectroscopically confirmed SNe Ia (black), photometric SNe Ia with host galaxy redshifts (gray), and photometric SN Ia candidates with no spectroscopic redshift (light-gray). The arrow shows the redshift cut for this analysis.

4.3 Survey Efficiency

To convert the number of discovered SNe Ia into a measurement of the SN rate, we must have an estimate of the efficiency for discovering SNe Ia at $z \leq 0.12$ that satisfy the sample selection criteria. We have two tools at our disposal for this estimate: the artificial SN images (fakes) that are inserted into the data stream in real time and Monte Carlo simulations of the 2005 observing season.

4.3.1 Use of Artificial SN Images

As noted in §2.3, the fake SNe images are used to measure the efficiency of the on-mountain software pipeline for point-object detection on a variety of galaxy backgrounds and observing conditions. The fake SNe are also used to measure the efficiency of human scanners for identifying objects as SNe. While the fakes were designed to model realistic SN Ia light curves, the z^2 dependence on the redshift distribution results in only 18 fake light curves with redshift $z < 0.12$. Although all 18 low-redshift fakes were recovered by the SN search pipeline, using such a small sample to measure the pipeline efficiency would result in large statistical and systematic uncertainties. Furthermore, the fake light curves were generated with distributions of A_V and Δm_{15} that were not realistic, which complicates the interpretation of discovery efficiency as a function of redshift.

To obtain a more reliable determination of the survey efficiency, we use fake SN Ia at all redshifts in the following way. We first use the fakes to measure the object-detection efficiency as a function of the signal-to-noise ratio (SNR) in the g, r, and i passbands. The detection efficiency, defined as the ratio of the number of fake epochs detected as objects by the on-mountain software pipeline to the number of fakes inserted into data images at a given signal-to-noise, is shown in Fig. 4.6. While

the object detection efficiency as a function of magnitude or redshift is sensitive to observing conditions (seeing, clouds, moon), the efficiency as a function of SNR is robust against such variations in conditions. As a check that the SNR is an adequate parameterization of the point-source detection efficiency, we have split the sample of fakes into a low-redshift and a high-redshift subsample and determined the efficiency as a function of SNR for each set independently. We find that the results are consistent. With the efficiency as a function of signal-to-noise ratio known, one can estimate the SN discovery efficiency as a function of redshift for *any* choices of SN Ia light-curve models, observing conditions, and population distributions. These efficiency functions measured with fakes are used in the Monte Carlo simulation (§4.3.2) to verify that the software pipelines were fully efficient at low redshift.

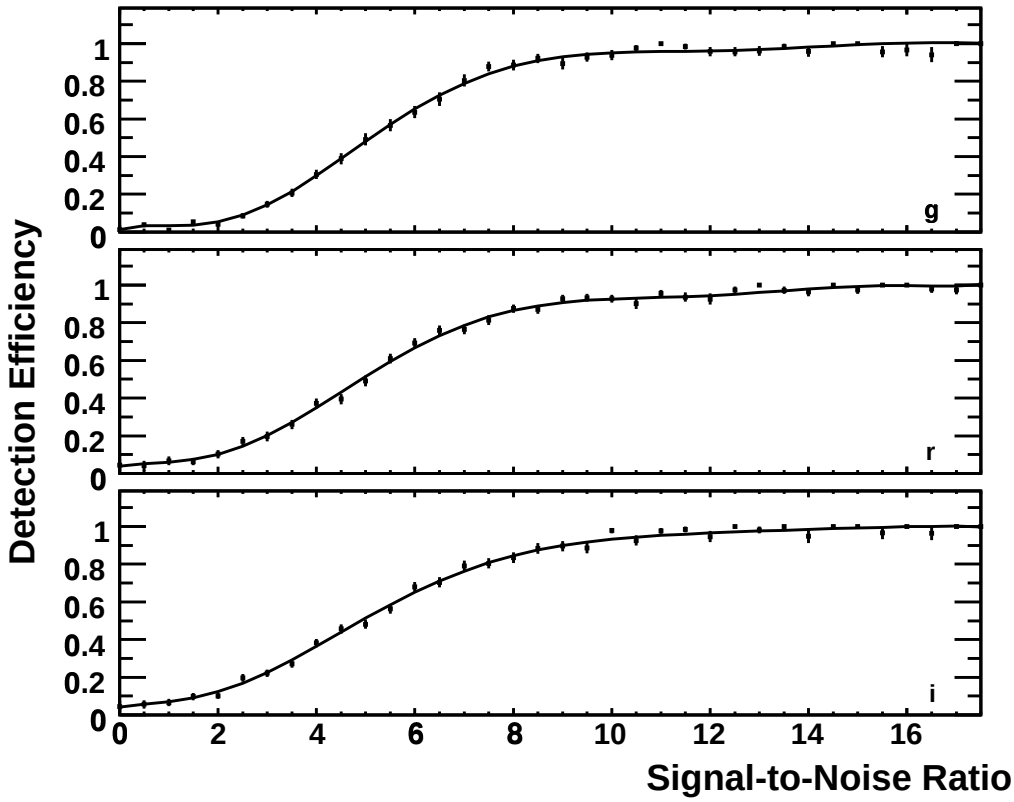

Figure 4.6: The mean object detection efficiency as a function of signal-to-noise ratio for SDSS g-band (top), r-band (middle), and i-band (bottom). The efficiency is derived by counting the fraction of fake images detected by the survey pipeline. The binomial errors on the efficiency measurements are shown. The solid lines show the result of a polynomial fit to the efficiency measurements. These efficiency functions are used to simulate the difference imaging software in the Monte Carlo simulations of the SN light curves.

The fakes also provide information on the efficiency of the human scanners to correctly label as possible SN candidates those fakes that were detected as objects by the software pipeline. For the 2005 season, 91% of all epochs of fakes visually scanned by humans were flagged as SN candidates, and 95% of all detected fake SNe were flagged by humans as SN candidates at least once. The 5% of fakes that were never identified by humans as SN candidates were detected on only a single epoch by the software pipeline, either because they were at high redshift or because they reached peak light well before or well after the observing season. Essentially all fakes detected on two or more epochs by the software pipeline were flagged by humans as SN candidates at least once. Given the selection cuts in §4.2.1, the human scanning efficiency is 100% for SNe Ia contributing to this low-redshift rate measurement.

Summary information on the efficiency of the software pipeline and the human scanners to detect fakes is presented in Figure 4.7, which shows the detection efficiencies, i.e., the fraction detected by the pipeline and the fraction identified as SN candidates by humans, vs. peak g-magnitude. The arrows indicate the peak g-band magnitudes for an unextincted normal and for an unextincted sub-luminous 1991bg-like SN Ia at $z = 0.12$, according to the MLCS2k2 model. This figure indicates that, for the assumed SN Ia model used to generate the distribution of fakes, the combined software+human detection efficiency is essentially 100% for SNe Ia in the redshift range $z \leq 0.12$.

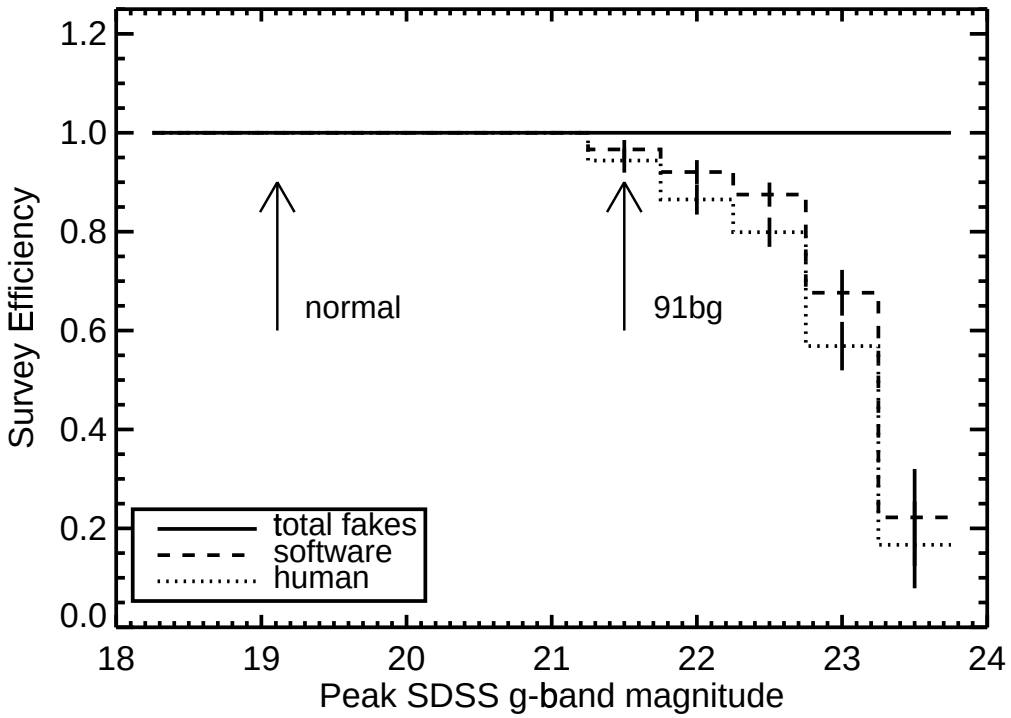

Figure 4.7: The efficiency for identifying fakes as SN candidates, as a function of peak g-band magnitude. The dashed curve is the efficiency for detection by the software pipeline, and the dotted curve is the efficiency for evaluation of the fakes as SN candidates by the human scanners. The arrows indicate the peak magnitudes for a normal and for a 91bg-like SN Ia at a redshift of 0.12 according to the MLCS2k2 model. The binomial errors on the efficiency are shown.

4.3.2 Monte Carlo Simulations

To determine the SN Ia selection efficiency with high precision and to study systematic uncertainties for the rate measurement, we have developed a detailed Monte Carlo light curve simulator (MC). The MC simulates individual light curve data points based on real observing statistics, but without the added complexity of adding fake SNe to images. The MC light curves can be generated and analyzed much more rapidly than the fakes, so the MC can be used to rapidly simulate very large numbers of SN Ia light curves to estimate the SN discovery efficiency and the uncertainty in the efficiency due to assumptions about the SN Ia model distributions. The MC code uses the MLCS2k2 model to generate simulated SN Ia light curves instead of the stretch/Δm_{15} model that was used to generate the fakes.

For each simulated SN Ia, the following parameters are randomly drawn from parent distributions:

1. **redshift, z:**

   Drawn from a distribution proportional to the comoving volume element, which assumes a constant SN Ia rate per unit comoving volume.

2. **host galaxy extinction, A_V:**

   Drawn from a distribution $P(A_V) \propto e^{-A_V/\tau}$, with $\tau = 0.4$. The Cardelli et al. (1989) reddening law, with $R_V = 3.1$, is used to extrapolate the extinction to other wavelengths. The choice of $\tau = 0.4$ was guided by the studies of Jha et al. (2007) and is consistent with the inferred extinction distribution for spectroscopically confirmed SNe Ia in the SDSS SN sample. As we discuss later in this section, the exact choice of τ makes no practical difference to this rate measurement.

3. **MLCS2k2 light curve shape/luminosity parameter, Δ:**

   Drawn from a bimodal Gaussian with a standard deviation of 0.26 for $\Delta < 0$ and 0.12 for $\Delta > 0$, and truncated to lie within the valid range of the MLCS2k2 model, $-0.35 < \Delta < 1.8$. The bimodal Gaussian is based on study of the confirmed SNe Ia in the SDSS-II Supernova Survey first year data.

4. **time of peak light in rest-frame B-band:**

   Drawn randomly from the interval 53616 < MJD < 53705 (Sept. 1 - Dec. 1, 2005).

5. **sky position:**

   Drawn randomly from the range of the survey.

6. **location within host galaxy:**

   Drawn from a distribution proportional to the host galaxy surface brightness (see below). This variable is used only to determine galaxy background light, not extinction.

We note that simulated photometry is generated only at epochs for which we obtained photometric imaging at the corresponding sky location, and therefore the determination of the selection efficiency naturally accounts for the temporal inhomogeneity in sky coverage, as can be seen in Figure 2.1.

Using these parameters for each SN, rest-frame $UBVRI$ magnitudes are generated from the MLCS2k2 model for all dates on which the survey took data at the selected sky position. These magnitudes are modified according to the host galaxy extinction, k-corrected to the observed SDSS gri passbands, and further modified according to the estimated Milky Way extinction at that position (Schlegel et al., 1998). The zero-points from the survey are used to convert the gri magnitudes into flux values that

would have been measured in ADUs by the SDSS 2.5 m telescope. The CCD gains are then used to determine the number of photo-electrons, and hence the signal and noise. Additional noise is computed for each measurement based on the measured observing conditions at each epoch, in each passband, at the assigned sky location. Sky noise is simulated by integrating the estimated sky noise per pixel over an effective aperture with a size determined by the local PSF estimate from `PHOTO`. Noise from the host galaxy is simulated by associating the SN with a host from the SDSS galaxy photometric redshift catalog (Oyaizu et al., 2008) selected to have a photometric redshift equal to the assigned SN redshift. In the SDSS DR5 (Adelman-McCarthy et al., 2007) `photoPrimary` database (Stoughton et al., 2002), each such galaxy image is fit with both an exponential and a de Vaucouleurs surface brightness profile. We use the exponential model in the r-band as a probability distribution from which the SN position within the galaxy is drawn. That is, the galaxy noise model assumes that the SN Ia rate is roughly proportional to r-band stellar luminosity. The estimated contribution of the galaxy light to the noise in each passband is computed by convolving the exponential galaxy model with the PSF in the survey image. In practice, this procedure is computationally expensive, so we pre-compute the noise values on a grid of model parameters and perform a multi-dimensional linear interpolation to obtain an estimate of the galaxy noise.

As a consistency check of the MC as a representation of the SN data, we compare the distributions of signal and noise in gri for the MC sample to the signal and noise for all photometric epochs for the low-redshift SNe Ia in the rate-measurement sample. The comparison of the distributions is shown in Fig. 4.8. The distributions of signal and noise are in good agreement, indicating that the MC model, and the assumed parameter distributions therein, provide a reasonable representation of the low-redshift SN Ia sample.

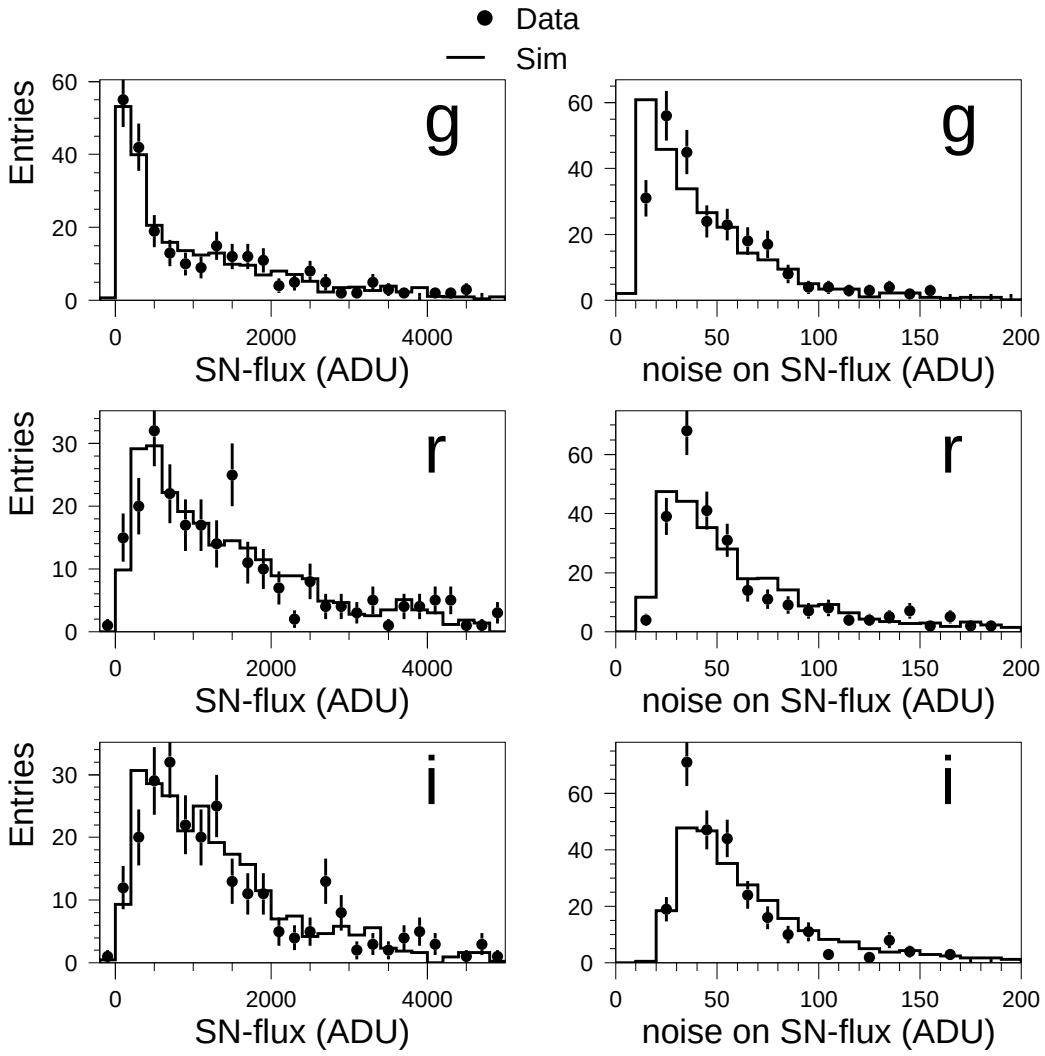

Figure 4.8: For SN Ia that satisfy the selection requirements (§4.2), the signal-flux and noise distributions are shown for all photometric epochs in the g,r,i filters. Each distribution is shown for SDSS data (dots) and for the simulation (histogram) that has been scaled to have the same number of entries as the data.

Having shown that the MC generates photometry that is consistent with our observed low-redshift SN Ia sample, we can use the MC to provide a more reliable determination of the detection efficiency of the on-mountain search pipeline than we could obtain with the relatively small number of low-redshift fakes. For each epoch generated by the MC, we use the efficiency as a function of signal-to-noise ratio in each passband (from Fig. 4.6) to determine the efficiency of the search pipeline to detect SNe Ia at all redshifts. The resulting software pipeline detection efficiency as a function of redshift, based on a MC study using 15640 total SNe (920 in each of 17 redshift bins) is shown in Figure 4.9; the efficiency is 100% over the redshift range $z \leq 0.12$. Since the fakes tests of §4.3.1 showed that the human scanning process causes a negligible loss of efficiency, we conclude that the combined efficiency for SN detection by the pipeline and identification as a candidate by humans is 100% over the redshift range of interest. This does not guarantee that the efficiency of the photometric typing code used for spectroscopic target selection (§2.2) is also 100%, but the studies of §4.2.2 indicate that, with the exception of SN 9266, there were no losses due to the target selection algorithm.

The final step is to use the MC to compute the survey discovery efficiency ϵ for a SN Ia sample defined by the selection requirements in §4.2.1. This efficiency is the ratio of the number of SNe Ia that are detected by the pipeline, identified by humans, and that pass the selection criteria of §4.2.1 to the total number of SNe Ia that reach peak light during the survey, i.e., between Sept. 1 and Nov. 30. While we have seen that the detection efficiency is essentially 100% out to $z = 0.12$, ϵ is less than 100% primarily because the selection requirements on light curve coverage (cuts 4 and 5 in §4.2.1) remove some SNe Ia that peaked in early September or late November. Using the MC sample of 15640 light-curves mentioned above and fitting a linear function

to the resulting selection efficiency in the redshift range $0 < z < 0.12$ gives

$$\epsilon(z) = (0.78 \pm 0.01) + (-0.13 \pm 0.14)\ z \tag{4.1}$$

That is, the survey efficiency is approximately constant at low redshifts, changing by only $\sim 1\%$ over the redshift range of the rate measurement. The mean SN Ia discovery efficiency for our rate sample is $\langle \epsilon \rangle = 0.77 \pm 0.01$.

While the data-MC comparison in Fig. 4.8 indicates that we have made a consistent choice of the parameter distributions for the MC model, to estimate the systematic uncertainty in the discovery efficiency we vary the assumed MC parameter distributions and recompute the efficiency. We find that varying τ, the parameter controlling the extinction distribution, has the largest systematic effect on the determination of the discovery efficiency from the MC. Varying τ over the range $0.2 - 0.6$, the estimated discovery efficiency for the rate-measurement SN Ia sample changes by less than a percent.

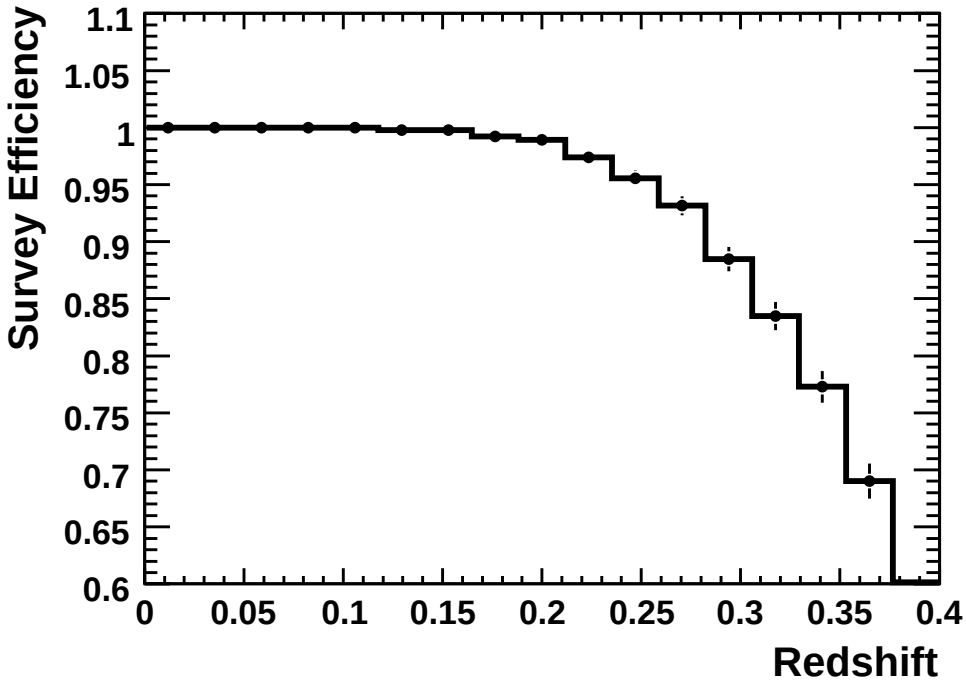

Figure 4.9: Search pipeline software efficiency as a function of SN Ia redshift, as determined from the Monte Carlo simulation.

4.4 SDSS SN Results

4.4.1 Volumetric SN Ia rate

For the purpose of interpreting the SN observations as a volumetric SN rate, we will assume a spatially flat cosmology with non-relativistic matter density $\Omega_m = 0.3$, dark energy density $\Omega_\Lambda = 0.7$, and dark energy equation of state parameter $w = p/\rho = -1$. For the low-redshift rate measurement presented in this section, the dependence on cosmological parameters of the survey selection efficiency is negligible, and so the uncertainty in the rate due to uncertainty in cosmology is due entirely to the difference in the volume of the survey. A change in Ω_m of 0.02 would lead to a 4% change in the rate measurement.

The observed volumetric SN rate, r_V, is defined as

$$r_V = \frac{N}{\widetilde{VT\epsilon}} \ , \tag{4.2}$$

where N is the number of SNe in the sample, and $\widetilde{VT\epsilon}$ is the effective product of the survey volume, V, the observer-frame survey duration, T, and the SN discovery efficiency, $\epsilon(z)$, estimated in §4.3.2,

$$\widetilde{VT\epsilon} = (\Theta T) \int_{z_{min}}^{z_{max}} dz \ \epsilon(z) u^2(z) \frac{du}{dz} \frac{1}{(1+z)} \ . \tag{4.3}$$

Here Θ is the solid angle covered by the survey and $u(z)$ is the comoving distance in the Friedmann-Robertson-Walker metric,

$$u(z) = \int_0^z \ dz' \frac{c}{H(z')} = \frac{c}{H_0} \int_0^z \frac{dz'}{\sqrt{\Omega_m (1+z')^3 + \Omega_\Lambda}} \ . \tag{4.4}$$

If the survey efficiency is independent of redshift, and if the redshift range covered

by the SN observations is small, then $\widetilde{VT\epsilon} \sim (VT\epsilon)/(1+\langle z \rangle)$, where V is the survey volume and $\langle z \rangle$ is the volume-weighted mean redshift of the survey.

For the SDSS-II Supernova Survey we have $N = 17$, $z_{min} = 0$, $z_{max} = 0.12$, $\langle \epsilon(z) \rangle = 0.77 \pm 0.01$, $T = 89$ days $= 0.244$ years, and $\Theta = 0.08277 * 0.98$ steradians. This value for Θ is 98% of the actual sky area covered by the survey, due to the masking of bright stars and variable sources. Substituting these values into Eqn. (4.2), we find a volumetric SN Ia rate of

$$r_V = [2.93^{+0.17}_{-0.04}(\text{systematic})^{+0.90}_{-0.71}(\text{statistical})] \times 10^{-5} \text{ SNe Mpc}^{-3}\ h_{70}^3\ \text{year}^{-1}\ , \quad (4.5)$$

with $h_{70} \equiv H_0\ (70 \text{ km s}^{-1}\text{Mpc}^{-1})^{-1}$ and H_0 the present value of the Hubble parameter. The statistical errors quoted represent the standard frequentist 68.27% central confidence interval on the mean of a Poisson distribution. The systematic uncertainty represents uncertainty on our determination of the SN selection efficiency (§4.3.2) and on the number of photometrically identified SNe Ia (§4.2.2). This measurement represents the volume-averaged SN Ia rate at $z \leq 0.12$. When rate measurements are plotted vs. redshift, it is generally assumed that the rate is constant over the sampled redshift interval. If we assume that the SN Ia rate is constant at $z \leq 0.12$, then Eqn.(4.5) can be interpreted as the rate at the volume-weighted mean of our redshift range, $\langle z \rangle = 0.09$, and we make this assumption when plotting the result. Our result is shown along with previously reported SN Ia rate measurements in Fig. 4.10, but we defer discussion of comparison and combination with other measurements to §4.5.2.

4.4.2 SN Ia Rate per unit galaxy luminosity

Early measurements of the SN rate were generally derived from SN observations that targeted known galaxies; for these surveys, the SN rate is most naturally measured as a rate per unit luminosity in some passband, traditionally the B-band. Blanc et al. (2004) have converted a number of measurements from the literature of the SN Ia rate per unit luminosity to rates per unit volume, and in Table 4.4 we adopt their values for the Cappellaro et al. (1999); Madgwick et al. (2003); Hardin et al. (2000) rate measurements.

For completeness, we convert our volumetric rate to a rate per unit galaxy luminosity in the SDSS passbands. The galaxy luminosity functions in the SDSS passbands are estimated in Blanton et al. (2003b). The corresponding luminosity densities in the *ugriz* passbands, at a mean redshift of $\langle z \rangle = 0.1$ are 1.60 ± 0.32, 1.25 ± 0.05, 1.29 ± 0.04, 1.48 ± 0.05, and 1.89 ± 0.05, in units of $10^8\ L_\odot\ h_{70}\ \mathrm{Mpc}^{-3}$, where $L_\odot$ is the solar luminosity. In combination with the volumetric rate measurement of Eqn.(4.5), this yields the SN Ia rate per unit luminosity in the SDSS passbands, $(r_L)_{ugriz}/h_{70}^2 = 0.183^{+0.06}_{-0.05}$ SNu$_u$, $0.235^{+0.07}_{-0.06}$ SNu$_g$, $0.227^{+0.07}_{-0.06}$ SNu$_r$, $0.197^{+0.06}_{-0.05}$ SNu$_i$, and $0.156^{+0.05}_{-0.04}$ SNu$_z$, where 1 SNu$_x \equiv 1$ SN $10^{-10} L_\odot^x$ (100 yr)$^{-1}$, with $L_\odot^x$ the luminosity in passband x, in units of solar luminosities.

4.4.3 SN Ia Rate as a function of host galaxy type

Recent measurements have shown that the specific SN Ia rate is higher in star-forming galaxies than in passive galaxies. For example, Mannucci et al. (2005) found that the SN Ia rate per unit stellar mass is $\sim 20-30$ times higher in late-type galaxies than in E/S0 galaxies. Sullivan et al. (2006b) have found a similar trend in the SNLS data. A detailed study of the SN rate vs. star formation activity using the SDSS-II Supernova

Survey sample is presented by Smith et al. (2008).

Here, we consider the low-redshift SN Ia rate vs. host galaxy type. We have considered several photometric galaxy-type indicators that are accessible through the SDSS DR5 database (Adelman-McCarthy et al., 2007), including $u-r$ color (Strateva et al., 2001); the likelihood of the de Vaucouleurs model fit to the galaxy surface brightness profile relative to that of an exponential model fit; and the (inverse) concentration index (Shimasaku et al., 2001; Yamauchi et al., 2005), defined as the ratio of the radii that contain 50% and 90% of the Petrosian flux (see Stoughton et al. (2002) for definitions of these quantities). These parameters are listed in Table 4.3 for the host galaxies of the SNe included in the rate-measurement sample. Note that the $u-r$ color in Table 4.3 is computed using SDSS model magnitudes (Stoughton et al., 2002) and is *not* K-corrected to the galaxy restframe. A host galaxy is associated with each SN by determining the nearest object, based on a measure of the galaxy image size. Specifically, the SDSS DR5 catalog includes the parameters of an iso-photal ellipse for each galaxy-like object, and for each of the *ugriz* filter bands, defined as the ellipse where the object surface brightness is 25 magnitudes arcsec^{-2} (Stoughton et al., 2002). We define the distance to a potential host galaxy to be the semi-major axis of the ellipse that is similar (has the same aspect ratio and orientation) to the r-band iso-photal ellipse and that intersects with the position of the SN. The host galaxy for each SN is defined to be the nearest object in this measure. For the SNe listed in Table 4.1, the association of SN with host galaxy was confirmed through visual inspection of the images.

Early-type galaxies generally display red colors (large $u-r$), are reasonably well fit by a de Vaucouleurs surface brightness profile (large values of the relative de Vaucouleurs likelihood), and show relatively strong central light concentration (low values of the inverse concentration index). Consequently, these three indicators are strongly

correlated and tend to give a consistent classification into early and late photometric types, indicated by the last column in Table 4.3. However, the classifications based on the three indicators do not always agree, in which case we have made a judgement based on visual inspection of the galaxy image and, where available, a high signal-to-noise galaxy spectrum. For these five cases, the host type indicated in the last column is marked with an asterisk.

Table 4.3. Host Galaxies for SNe Ia in the rate sample.

SDSS Id	α (J2000.0)	δ (J2000.0)	$u-r$	de Vaucouleurs likelihood	concentration index	Host Type
1241	22 30 41.15	−00 46 34.5	2.82	0.91	0.382	Early
1371	23 17 29.70	+00 25 46.8	2.97	0.00	0.377	Early*
2561	03 05 22.64	+00 51 35.0	2.59	0.00	0.410	Late*
3256	21 57 04.19	−00 13 24.5	1.99	0.00	0.442	Late
3592	01 16 12.71	+00 47 26.0	2.21	0.00	0.427	Late
3901	00 59 24.11	+00 00 09.5	1.40	1.00	0.418	Late*
5395	03 18 33.80	+00 07 24.0	1.29	0.49	0.360	Late*
5549	00 12 59.97	+00 14 54.9	1.01	0.46	0.461	Late
5944	01 56 48.50	−00 12 45.3	2.57	0.00	0.469	Early*
6057	03 30 12.89	−00 58 28.1	1.79	0.00	0.485	Late
6295	01 34 41.84	−00 36 15.2	2.97	1.00	0.312	Early
6558	01 26 48.46	−01 14 17.3	2.23	0.00	0.427	Late
6962	02 35 26.58	+01 04 28.3	2.71	1.00	0.379	Early
7147	23 20 04.44	−00 03 20.2	3.22	1.00	0.350	Early
7876	01 16 43.87	+00 47 36.9	1.71	0.00	0.532	Late
8719	00 30 53.23	−00 43 07.3	1.12	0.01	0.412	Late
9266	03 20 43.19	−01 00 08.2	2.25	0.00	0.398	Late

*At least one of the three photometric type indicators indicates a different type from that listed.

Note. — SDSS Id denotes internal candidate designation. α and δ are the coordinates of the host galaxy of the SN. The photometric morphology indicators, $u-r$, de Vaucouleurs likelihood, and concentration index are described in (§4.4.3).

Of the three photometric type indicators, $u-r$ correlates most strongly with the host type we have assigned to each galaxy in the last column of Table 4.3. The distribution of SDSS galaxies is approximately bimodal in $u-r$ (Strateva et al., 2001), suggesting a natural division between early and late types. We therefore use $u-r$ as the galaxy classifier for the purpose of studying the SN rate vs. galaxy type. This is preferable to using the 'host type' classification in Table 4.3, since the subjective human judgement required to determine the latter makes it difficult to determine its population properties. Strateva et al. (2001) suggest that $u-r=2.2$ is an optimal separator between early and late types. However, our catalog of galaxies with photometric redshifts in stripe 82 (Oyaizu et al., 2008) appears to be better separated into two subpopulations using $u-r=2.4$. Since a division at $u-r=2.4$ also provides better agreement with the subjective 'host type' classification in Table 4.3, we use this color cut to separate the hosts into early ($u-r>2.4$) and late ($u-r<2.4$) types for the relative rate measurement. Using a large sample of galaxies from the SDSS DR5 database, we find that the fractional r-band luminosity densities for early and late-type galaxies at redshifts $z\leq 0.12$ are 54% and 46%, respectively. From Table 4.3, we find that the SN Ia rate per unit r-band luminosity is $\sim 1.68^{+0.52}_{-0.41}$ times higher in late-type galaxies than in early-type galaxies. Using the luminosity functions of Blanton et al. (2003b), we find that the absolute rates per unit luminosity are $r_L/h_{70}^2 = 0.085^{+0.03}_{-0.02}$ SNu_r (early) and $0.142^{+0.04}_{-0.03}$ SNu_r (late). The evidence for a larger SN Ia rate in late-type galaxies is statistically marginal with the current low-redshift sample. The systematic uncertainty is also significant: if we place the host galaxy type cut at $u-r=2.2$, we find no significant difference between the rate per unit luminosity in early- and late-type hosts.

4.5 Fitting SN Rate evolution models

As noted in §1, models for SN Ia progenitors in principle can be distinguished by their predictions for the evolution of the SN Ia rate with cosmic time. In this section, we present a general maximum likelihood method of fitting SN observations to models with a redshift-dependent SN rate. We then apply the method to a recently discussed SN Ia rate model, using data from the SDSS-II Supernova Survey and from other published rate measurements.

4.5.1 Maximum Likelihood method

In this section we describe a method for fitting SN data to models of the SN rate without binning the data. The method is similar to the methods described in Strolger et al. (2004). and Strolger & Riess (2006). A distinguishing feature of our analysis is that it allows for combining multiple data sets and accounts for systematic errors.

A general model for the volumetric SN rate can be written as $r_V(z;\mathbf{p})$, where $\mathbf{p}$ represents the set of model parameters. According to the model, the total number of detected SNe follows a Poisson distribution with mean value

$$\langle N(\mathbf{p})\rangle = \int_0^\infty dz\ \Theta T\epsilon(z)\ \frac{r_V(z;\mathbf{p})}{(1+z)}\ u^2(z)\ \frac{du}{dz}\ , \tag{4.6}$$

where all symbols were defined in §4.4.1. The probability of detecting a SN at redshift z is given by the integrand of Eqn.(4.6), $P(z_i) \propto d\langle N(\mathbf{p})\rangle/dz$, giving a likelihood function for detecting SNe at the N observed redshifts $\{z_i\}$,

$$L(\{z_i\};\mathbf{p}) = \frac{e^{-\langle N(\mathbf{p})\rangle}\langle N(\mathbf{p})\rangle^N}{N!}\prod_{i=1}^{N}\frac{1}{\langle N(\mathbf{p})\rangle}\frac{d\langle N(\mathbf{p})\rangle}{dz}. \tag{4.7}$$

The corresponding log-likelihood function, suppressing terms that do not depend

on the model parameters, is

$$\log L(\{z_i\};\mathbf{p}) = -\langle N(\mathbf{p})\rangle + \sum_{i=1}^{N} \log\left(\Theta T \epsilon(z_i)\ \frac{r_V(z_i;\mathbf{p})}{(1+z_i)}\ u^2(z_i)\left[\frac{du}{dz}\right]_{z_i}\right) . \quad (4.8)$$

The best-fit model is determined by maximizing the log-likelihood with respect to the model parameters, $\mathbf{p}$. To incorporate information about the systematic error in our fits, we weight the contribution to the log-likelihood for each data set by multiplying each term in the log-likelihood function by the factor $\sigma_{stat}^2/(\sigma_{stat}^2+\sigma_{syst}^2)$, where σ_{stat} and σ_{syst} are the statistical and systematic errors for the measurement. This factor assumes that the systematic errors are approximately Gaussian and independent of the statistical errors. We note that auxiliary information about the model parameters and uncertainties in the survey parameters Θ, T, and $\epsilon(z)$ could be incorporated in a more rigorous way via prior probability distributions. However, this would require full knowledge of the probability distribution functions for the efficiency, subject to all possible variations of systematic effects, which is in practice unknown.

To combine data from multiple surveys, the log-likelihood functions for each survey are added together, using the appropriate values of $\epsilon(z)$, Θ, and T for each survey. The advantage of this method is that it does not involve binning the SN data in redshift; however, it does require knowledge of the efficiency function $\epsilon(z)$ for each survey. To evaluate the goodness of fit of a given model, one can use, e.g., the Kolmogorov-Smirnov (KS) test applied to the data and to a large-statistics Monte Carlo sample generated from the best-fit model parameters. The code for fitting rate models was tested on large MC samples ($\sim$ 1000 SNe), and the MC model parameters were accurately recovered.

As an illustration of the likelihood method, we apply it to the SDSS-II Supernova

Survey data, assuming a redshift-independent model over the redshift range probed by the data, $r_V(z) =$ constant. In this case, the rate that maximizes the likelihood can be shown analytically to be given by Eqn. 4.2. The probability for this model from the KS test statistic is $p_{KS} = 0.42$, meaning that if the model is correct, 42% of sample observations drawn from the model would have a KS test statistic as large or larger than that found in comparing this data set to the model. In the discussion that follows the probabilities from the KS test are given as rough estimators of the goodness of fit only; the distribution of the KS test statistic does not in general have an analytic form when model parameters are estimated from the data.

4.5.2 SN Rate Models and Star Formation History

As discussed in §1, measurements of the SN Ia rate provide a means to distinguish between models of SN Ia progenitor systems. The connection between the observed SN Ia rate and the progenitor systems is made through the relation of the SN rate to the cosmic star formation history. Sometime after a population of stars form, a fraction of them will end up in binary systems that are producing SN Ia explosions. If we denote the distribution of delay times between formation of the progenitor systems and the SN explosions by $D(t)$, then the volumetric SN Ia rate $r_V(t)$ and the cosmic star formation rate $\dot{\rho}(t)$ are related by

$$r_V(t) = \int_0^t dt' \dot{\rho}(t') D(t - t') \ . \tag{4.9}$$

We can therefore constrain models for the distribution of delay times, $D(t)$, by comparing the SN Ia rate and the star formation rate. A discussion of predicted delay-time distributions for a variety of SN Ia progenitor models is given in Greggio (2005). A

simple model distribution that allows for two distinct contributions to the SN Ia rate is

$$D(t) = A + B\delta(t) \tag{4.10}$$

where $\delta(t)$ is the Dirac delta function. This '$A+B$' model was proposed by Mannucci et al. (2006) and Scannapieco & Bildsten (2005) and it has been used in SN rate studies by the SNLS (Neill et al., 2006) and Sullivan et al. (2006b). The SN rate can be written $r_V(t) = A\rho(t) + B\dot{\rho}(t)$, where $\rho(t)$ is the stellar mass density. The B term represents an instantaneous or prompt SN Ia component and the A term represents an extended component in which SNe Ia form with uniform probability in the time interval following star formation. In addition to the '$A + B$' model, we also consider a simple model in which $r_V(t)$ evolves as a power law in redshift, independent of considerations of star formation history.

4.5.3 Rate Measurements: Combining Data Sets

The constraints on redshift-dependent models of the SN Ia rate are improved if one uses SN observations over a wide range of redshifts. In the following, we combine the low-redshift rate measurement from the SDSS-II Supernova Survey with other SN Ia rate measurements in the literature. For each data set, we require both the SN redshifts and an estimate of the redshift-dependent selection function $\epsilon(z)$, and we therefore restrict ourselves to using data sets for which it is straightforward to infer the redshift dependence of the efficiency. We note that several authors, including Barris & Tonry (2006) and Poznanski et al. (2007b) have made SN rate measurements based on samples of photometrically identified SNe. However, in combining data sets for the present analysis, we will restrict ourselves to rate measurements that are based

primarily on spectroscopically identified SNe. Of the nine previously published rate measurements that have been based on primarily spectroscopically identified SNe, shown in Fig. 4.10, we will make use of four, in addition to the one in this work. These five rate measurements are shown in bold font in Table 4.4. The weighting factors, used to account for the systematic uncertainty on each measurement, are listed in the last column of Table 4.4. In cases where the uncertainty on the measurement is asymmetric, we define the weighting factor to be the mean of the upper and lower weighting factors. Varying the weighting factor between the extremes of using the smaller weight, and of using the larger weight, the best-fit parameters change by $\sim 5\%$ of the statistical error. In the subsections below, we briefly describe the data from other measurements that we include in the model fits and how we describe their efficiency function. We also discuss measurements that we exclude from the model fits.

Table 4.4. SN Ia Rate Measurements.

Reference	Redshift Range	Mean Redshift	N_{SNe}	Rate $[10^{-5}$ SNe h_{70}^3 Mpc^{-3} yr$^{-1}]$	$\sigma_{stat}^2/\sigma_{tot}^2$
Cappellaro et al. (1999)*	~ 0	~ 0	70	2.8 ± 0.9	N/A
This work*	$0 - 0.12$	0.09	17	$2.9^{+0.9}_{-0.7}$	0.988
Madgwick et al. (2003)	$0 - 0.19$	0.10	19	3.1 ± 1.6	N/A
Blanc et al. (2004)	$0 - 0.3$	0.13	14	$2.0^{+0.84}_{-0.72}$	N/A
Hardin et al. (2000)	$\sim 0.02 - 0.2$	0.14	4	$3.4^{+2.9}_{-1.7}$	N/A
Dahlen et al. (2004)	$0.2 - 0.6$	0.45	3	$6.9^{+15.8}_{-3.7}$	N/A
Neill et al. (2006)*	$0.2 - 0.6$	0.45	73	$4.2^{+1.4}_{-1.1}$	0.492
Tonry et al. (2003)	$\sim 0.25 - 0.6$	0.46	8	4.8 ± 1.7	N/A
Pain et al. (2002)*[a]	$0.25 - 0.85$	0.55	37	$5.4^{+1.5}_{-1.4}$	0.643
Dahlen et al. (2004)*	$1.0 - 1.4$	1.2	6	$11.5^{+4.7}_{-5.1}$	0.686

[a]The value of the rate has been corrected to our assumed cosmology, according to equation 3 of Pain et al. (2002).

Note. — Measurements included in the model fits are shown in bold face, and are marked with an asterisk. Mean redshift refers to the mean of the expected SN redshift distribution, under the assumption of a constant SN rate. For Madgwick et al. (2003), this is estimated as the mean of the observed SN redshift distribution. Systematic and statistical errors, when reported separately, have been combined in quadrature. Rate measurements reported here assume constant volumetric rate over the range of each survey. σ_{stat} is the reported statistical error on the measurement. σ_{tot} is the sum in quadrature of the reported statistical and systematic errors.

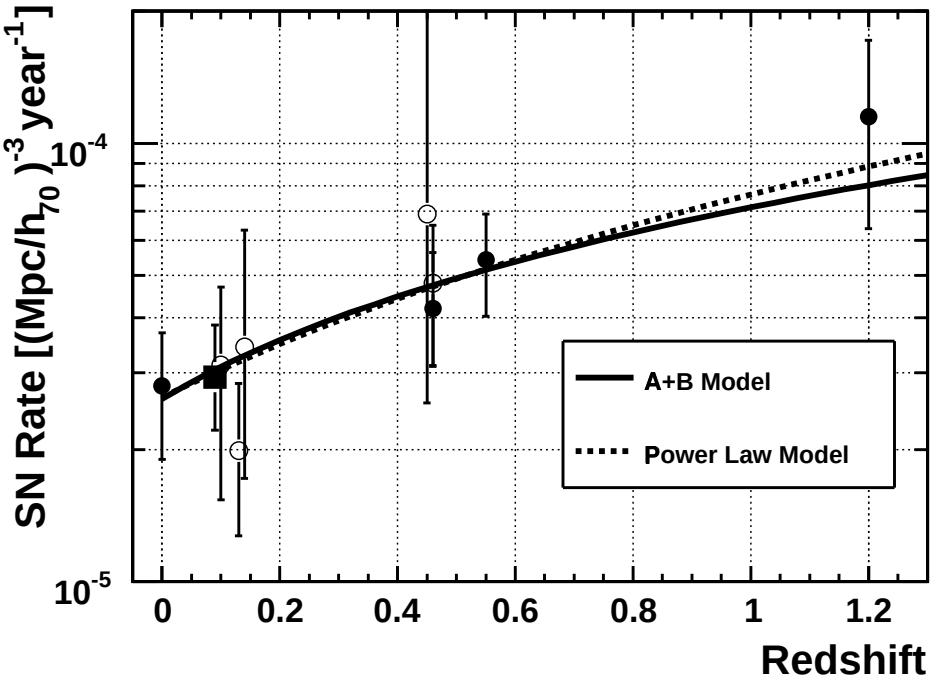

Figure 4.10: Measurements of the SN Ia rate discussed in §4.5.3. The SDSS-II Supernova Survey measurement is shown as the solid black square. Measurements for which the data is used in the model fits are shown as solid circles (see Table 4.4), and measurements not used in the fits as open circles. To plot each measurement, we have assumed in each case a model in which the rate is constant over the redshift range covered by that measurement. The rate as a function of redshift for the best fitting '$A + B$' and power law models are overlaid.

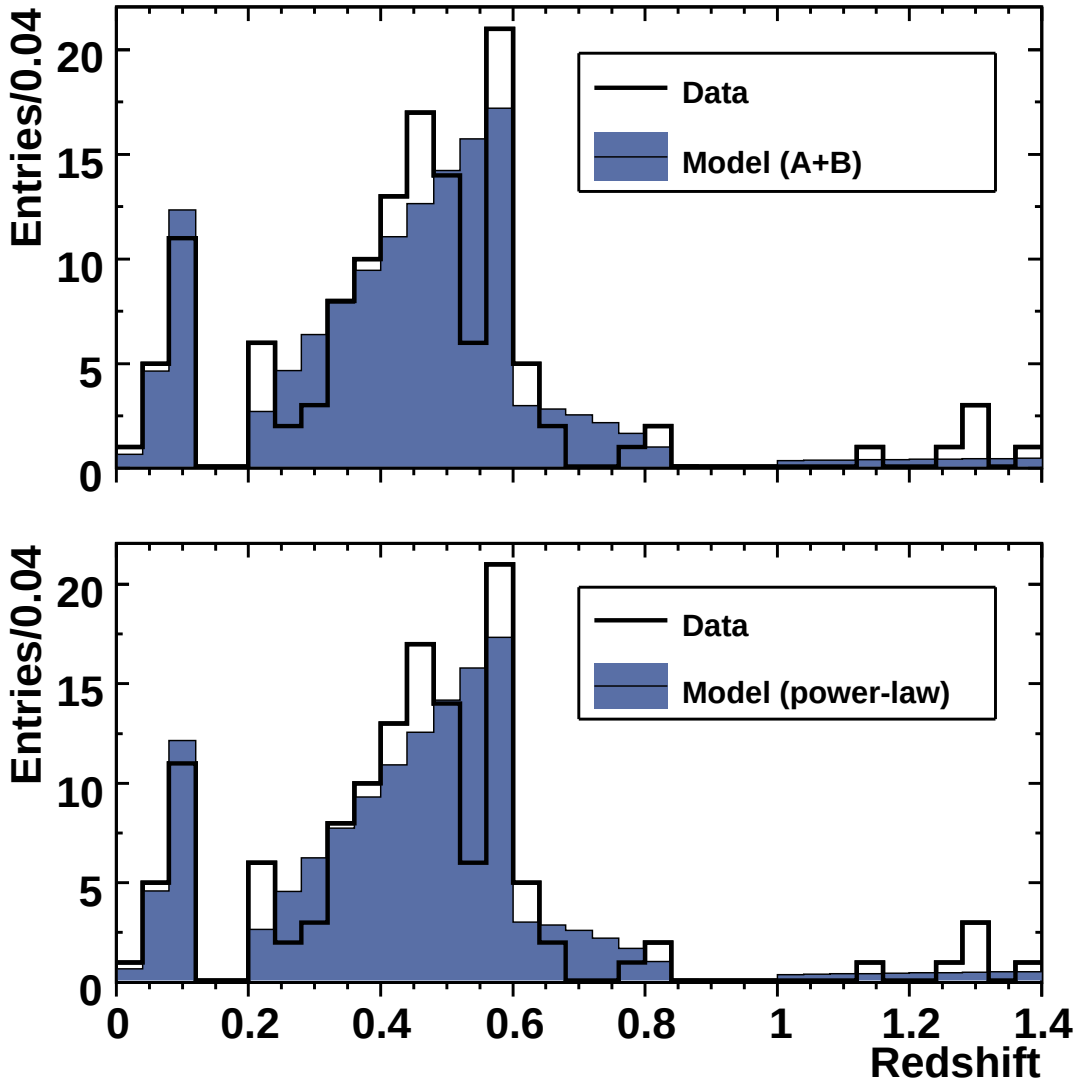

Figure 4.11: Comparison of the observed distribution of SNe and the predicted distributions for the $A + B$ (top) and power law (bottom) rate models. In each panel the shaded region shows the predicted redshift distribution of the best-fit model. The figures include the five highlighted data sets in Table 4.4.

Other rate measurement data included in the model fits

Neill et al. (2006) measured the SN Ia rate using 73 SNe Ia from the SNLS. They state that their sample is spectroscopically complete, i.e., that $\epsilon(z)$ is constant, to $z = 0.6$. Including the solid-angle and survey observation time, the factor $\Theta T\epsilon(z) = 7.37\times10^{-4}$ steradian year.

The measurement of Pain et al. (2002) is based on data from the Supernova Cosmology Project, covering about 12 square degrees. Although Pain et al. (2002) do not give $\epsilon(z)$ explicitly, they do provide the redshift distribution of SNe recovered from their Monte Carlo simulations which assumed a constant rate per unit comoving volume. With this information, we can compute the relative number of MC-generated SNe in each redshift bin and thereby the redshift dependence of their efficiency function. Fitting a quadratic function to this tabulated efficiency function in the range $0.25 < z < 0.85$ gives $\Theta T\epsilon(z) = (2.68 + 0.61z - 4.22z^2) \times 10^{-4}$ steradian year.

Cappellaro et al. (1999) measured the SN Ia rate for the local Universe by combining data from a number of surveys, including visual searches of nearby galaxies. Although they do not provide an efficiency function or a redshift distribution, the redshift range covered by the measurement is so small that we take the quoted result to be the SN Ia rate at $z = 0$. We include the Cappellaro et al. (1999) rate measurement by adding a standard χ^2 term to the log-likelihood function, i.e., a term of the form $(r_V(0;\mathbf{p}) - r_{V,Capp})^2/2\sigma^2_{Capp}$, where $r_V(0;\mathbf{p})$ is the model prediction at redshift zero, $r_{V,Capp}$ is the Cappellaro et al. (1999) measurement in Table 4.4, and σ_{Capp} is the quoted error on the measurement.

Dahlen et al. (2004) measured the SN Ia rate to $z \sim 1.6$ using data from the Great Observatories Origins Deep Survey (GOODS) carried out with the Advanced Camera for Surveys on the Hubble Space Telescope (HST). (Kuznetsova & Connolly (2007)

have recently presented SN Ia rate measurements based on analysis of 57 SNe from HST, including the 42 SNe analyzed by Dahlen et al. (2004), but we will make use of the Dahlen et al. (2004) analysis).

We use their measurement in the redshift range $1.0 < z < 1.4$. Using their scaled efficiency function, as inferred from Figure 14 of Strolger et al. (2004), we fit a function $A + Bz + Cz^2 + Dz^3$, valid in the redshift range $1.0 < z < 2.0$. The best-fit parameters are $A = -7.557, B = 55.93, C = -51.07$ and $D = 12.5$. This function is normalized so that the number of expected SNe for their survey is equal to six, the number they observed in the redshift interval $1.0 < z < 1.4$, giving a value of $\Theta T\epsilon(z) = [-10.35 + 76.61z - 69.95z^2 + 17.12z^3] \times 10^{-4}$ steradian year.

The redshift dependence of the efficiency function for the present data set is discussed in §4.3.2; including the solid-angle and survey observation time, $\Theta T\epsilon(z) = [1.54 - 0.025z] \times 10^{-2}$ steradian year.

Rate measurement data not included in the fits

In fitting the models, we choose not to include several of the SN Ia rate measurements listed in Table 4.4. We exclude the Dahlen et al. (2004) rate measurement in the redshift range $0.2 < z < 0.6$ because the efficiency function, given by Strolger et al. (2004), is only plotted for redshifts greater than 1, and because the 73 SNe from SNLS (Neill et al., 2006) in the same redshift range dominate the fit in comparison to the 3 SNe from Dahlen et al. (2004). Similar reasoning holds for the measurement of Tonry et al. (2003), which is based on 8 SNe in the redshift range well covered by the SNLS, and for which the redshifts are not explicitly stated. Both the Hardin et al. (2000) and the Blanc et al. (2004) rate measurements, based on data from the EROS microlensing survey, included a requirement that each SN be associated with

a host galaxy with apparent magnitude $R \lesssim 19$, which introduces a bias against faint hosts. If SNe Ia occurred at a constant rate per unit R-band luminosity in all galaxies, this would not be an issue. However, as noted above, it has been shown that the SN Ia rate per unit stellar mass (for which the total R-band luminosity is a proxy) is a function of SFR (Mannucci et al., 2005; Sullivan et al., 2006b). Finally, the Madgwick et al. (2003) measurement is based on SNe discovered via principal component analysis in spectra obtained by the SDSS galaxy redshift survey. This measurement has significant systematic uncertainties that are different from those in photometric surveys. In particular, the SNe discovered by this technique must lie within approximately 1.5" of the cores of their host galaxies, the radius of the SDSS spectroscopic fibers. To derive a SN rate from these spectroscopic observations, assumptions are needed about how SNe are distributed within their host galaxies at larger galactocentric distances.

4.5.4 Fits to SN Ia Rate Models

We now consider fits of the combined SN Ia rate measurements to the rate models discussed in §4.5.2, using the maximum likelihood approach of §4.5.1. The errors quoted below are the values of the fit parameters for which the log-likelihood function changes by 1/2 compared to its maximum, which assumes that the likelihood function is approximately Gaussian. We use the MINUIT software package (James & Roos, 1994) for the function optimization and error analysis.

Power-law redshift evolution of r_V

We first consider a simple two-parameter model that describes power-law redshift evolution of the SN rate independent of consideration of the star formation history,

$r_V(z) = \alpha(1+z)^\beta$. The best-fit power-law model is shown as the dashed curve in Fig. 4.10, and the predicted redshift distribution is shown in Fig. 4.11. Fitting this model to the five data sets, we find

$$\begin{aligned} \alpha &= (2.6^{+0.6}_{-0.5}) \times 10^{-5} \text{ SNe Mpc}^{-3}\ h_{70}^3\ \text{yr}^{-1} \\ \beta &= (1.5 \pm 0.6) \\ \rho_{\alpha\beta} &= -0.80 \end{aligned}$$

where $\rho_{\alpha\beta}$ is the correlation coefficient between the two fitted parameters. The KS probability for this model is $p_{KS} = 0.63$. We emphasize that the fitted value of β is greater than 0, i.e., the rate is determined to be an increasing function of redshift, at the $\sim 2.5\sigma$ level.

The 'A+B' model

We next consider the '$A + B$' model, with $D(t)$ given by Eqn. 4.10. As discussed by Förster et al. (2006), there is still significant uncertainty on the cosmic star formation rate (SFR), which is a limitation for placing observational constraints on SN delay time models. In what follows we choose one estimate of the SFR, and do not propagate the systematic uncertainties in the SFR. We follow the approach of Neill et al. (2006) and take the star formation rate from Hopkins & Beacom (2006). The functional form of the star formation rate is

$$\dot{\rho}(z) = \frac{a+bz}{1+(z/c)^d}\ h_{100}\ \text{M}_\odot\ \text{yr}^{-1}\ \text{Mpc}^{-3}\ , \tag{4.11}$$

where $h_{100} = H_0\ (100\ \text{km sec}^{-1}\ \text{Mpc}^{-1})^{-1}$, $a = 0.0118, b = 0.08, c = 3.3$, and $d = 5.2$. For the stellar mass density (the A component) we integrate the star formation rate

over time; as mentioned by Neill et al. (2006), this can be expected to overestimate the total stellar mass density relative to estimates of the stellar mass density that are based on luminosity, as it includes a contribution from stars that have burned out. Performing the fit using the five data sets gives

$$\begin{aligned} A &= (2.8 \pm 1.2) \times 10^{-14} \text{ SNe } \mathrm{M}_{\odot}^{-1} \text{ yr}^{-1} \\ B &= (9.3^{+3.4}_{-3.1}) \times 10^{-4} \text{ SNe } \mathrm{M}_{\odot}^{-1} \\ \rho_{AB} &= -0.78 \end{aligned}$$

where ρ_{AB} is the correlation coefficient between the two fitted parameters. The KS probability for this model is $p_{KS} = 0.71$. The best-fit '$A + B$' model is shown as the solid curve in Fig. 4.10, and the predicted redshift distribution is shown in Fig. 4.11. We note that the uncertainties on the A and B parameters are $\sim 43\%$ and $\sim 35\%$, respectively. For comparison, if we perform a fit to the '$A + B$' model, suppressing the SDSS data, the uncertainties on the fit parameters are $\sim$ 53% and $\sim$ 38%, respectively. Our analysis here is similar to that presented by Neill et al. (2006), with the primary differences being that we use a different subset of the available data, and we use a maximum likelihood method to fit the data to models of the SN rate. For comparison, Neill et al. (2006) found values of $A = (1.4 \pm 1.0) \times 10^{-14}$ SNe $\mathrm{M}_{\odot}^{-1}$ yr^{-1} and $B = (8.0 \pm 2.6) \times 10^{-4}$ SNe $\mathrm{M}_{\odot}^{-1}$. Both analyses find evidence for two components to the SN rate with the significance of the 'A' (extended) component less than that of the 'B' (prompt) component.

We note that one cannot accurately judge the goodness of fit of this model using a visual inspection or χ^2 fit to Fig. 4.10, since the measurements are each plotted *assuming* a constant-rate model. A better picture of the goodness of fit is given by Fig. 4.11, which shows the observed redshift distribution for the five data sets com-

pared with the predicted redshift distributions for the '$A + B$' and power-law rate models convolved with the measured efficiency functions for the different measurements. The agreement between the predicted distributions for both evolving models and that of the data is quite reasonable.

4.6 Summary of Low-Redshift SN Rate Measurement

We have presented a measurement of the SN Ia rate in the redshift range $0 < z \leq 0.12$ from the first season of the SDSS-II Supernova Survey. After selection cuts, the rate-measurement sample includes a total of 17 SNe Ia, of which 16 were spectroscopically confirmed. The final SN in the sample is a highly extincted, photometrically identified SN Ia with a measured host galaxy redshift. The insertion of artificial SNe in the data stream and the use of detailed Monte Carlo simulations of the survey efficiency, along with the rolling nature of the SDSS-II Supernova Survey, have enabled us to obtain a SN Ia rate measurement with smaller systematic uncertainties than previous measurements in a comparable redshift range.

We have also applied a maximum-likelihood technique, which enables us to account for systematic errors and to fit multiple SN data sets to models of the SN rate as a function of redshift. This maximum likelihood method makes optimal use of the available data, but requires estimates of the SN detection efficiency, and its uncertainty, as a function of redshift. We have applied this technique to a combination of recent SN Ia data sets, focusing on the '$A + B$' model that relates the SN Ia rate to the cosmic star formation rate.

Models in which the SN Ia rate evolves with redshift are preferred over a model with a constant rate, but the data do not distinguish significantly between a simple power-law evolution of the SN Ia rate with redshift and the '$A + B$' model. The A

and B parameter values we obtain are in good agreement with the results of Neill et al. (2006).

CHAPTER 5

THE SN RATE AS A FUNCTION OF REDSHIFT FROM THE SDSS-II SUPERNOVA SURVEY

5.1 Introduction

A precise measurement of the low-redshift type Ia SN rate from the first season of the SDSS-II Supernova Survey was presented in Chapter 4. In this Chapter we discuss extension of the volumetric SN Ia rate measurement to a higher redshift limit, based on the first 2 seasons of the SDSS-II Supernova Survey. Including SNe from 2 years of the SDSS-II Supernova Survey and considering a larger redshift range results in a large increase in the number of SNe considered for the rate measurement. At low-redshifts, the SN rate measurements discussed here have the same high purity and completeness as for the low-z rate from the first season discussed in §4, with increased statistical power. Considering higher redshift SNe will allow for investigating the redshift dependence of the SN Ia rate over the range covered by the SDSS-II Supernova Survey. However, at higher redshifts, systematic uncertainties become increasingly important and eventually dominate the error budget. The efficiency studies and SN selection functions described herein have also been used for studies of the type Ia SN rate as an explicit function of the properties of their host galaxies by Smith et al. (2008).

5.2 SN Ia Sample for the Rate Measurement

5.2.1 SN Selection

In the measurement of the low-redshift SN Ia rate, discussed in Chapter 4, we included in our sample all spectroscopically confirmed SNe Ia, subject to a set of objective selection criteria that can be robustly modeled with our SN MC simulations. To account for spectroscopic incompleteness, we analyzed the SMP (§2.5) light-curves for a set of ≈ 1000 photometric SN candidates, which was composed of ≈ 500 "best" Ia candidates, and ≈ 500 randomly chosen candidates.

In the present analysis we use a somewhat different approach for making a correction for spectroscopic incompleteness of the SN sample. As discussed in §2.2, during the survey the search-photometry light-curves were fit to models of type-Ia, type-Ib/c, and type-II SNe, and the results were used as a factor in prioritizing our spectroscopic follow-up resources. In addition, as a method of searching for photometric SNe Ia subsequent to the survey observing season, the search-photometry light curves are used to define a Bayesian probability for the candidate to be a SN of a given type. This is done by marginalizing over the fit parameters to obtain the *Bayesian evidence*, and requiring that the sum of the evidences for the 3 SN types sums to 1. This defines the "probability", $p_{\rm T}$, for an object to belong to the class of SN, T. This quantity can be considered a probability in the sense that it is bounded by $0 < p_{\rm T} < 1$, and is normalized to 1, $\Sigma_{\rm T}\ p_{\rm T} = 1$. However, this procedure makes the initial assumption that the object is a SN, i. e. that the 3 classes $T = {\rm Ia, Ib/c, II}$ are exhaustive, and does not allow for other possibilities for the identity of the object, e. g. AGN. Regardless of this caveat, the quantities $p_{\rm T}$ are in any case useful statistics for analyzing the search photometry light curves. The procedure is motivated by, and modeled after that discussed by (Kuznetsova & Connolly, 2007; Poznanski et al., 2007a).

As discussed in §2.5, the analysis of SN light curves for the SN rate analysis is done using the final photometric reduction (SMP). The set of candidates to be processed through the SMP software pipeline for the present analysis was selected by requiring the candidates to satisfy a set of selection criteria on the color-typing fits (§2.2). Specifically we require

- $p_{Ia} > 0.45$
- At least 3 search discovery epochs
- If the candidate has more than 5 search photometry epochs, the best fit Ia model is not 2005gj

These selection criteria were determined by correlating the fit results from the full analysis of the SMP light-curves for the $\approx$ 1000 photometric SN candidates from the 2005 season with statistics of the corresponding color-typing fits to the search photometry, and looking for a combination of cuts that would result in a sample of SN candidates with high purity and completeness with respect to SNe Ia. Several possible statistics of the color-typing fits were considered to improve the efficiency for selecting SNe Ia from the search photometry SN candidates. The conclusion of these correlation studies was that the Bayesian probability, p_{Ia}, is the best single quantity to consider for selecting a large fraction of SNe Ia, and no significant improvement was found by considering additional fit statistics, such as, e. g. the value of the reduced χ^2 statistic. The choice of a cutoff value of 0.45 for the p_{Ia} statistic was chosen to limit the sample to $\approx$ 600 SNe per season, which is a reasonable number to process through the final photometry pipeline with our available computing resources. The peculiar SN Ia, 2005gj, is included as part of the SN Ia light-curve models in the color-typing fits, and the requirement that the best fit SN *not* be 2005gj is effectively

intended to remove AGN (SN 2005gj has a flat, AGN-like light curve post-maximum; see Prieto et al. (2007)). In addition to the requirements on the color-typing fits, we require the SMP light-curves for the candidates to satisfy the same selection criteria on light-curve sampling and fit quality discussed in §4. We briefly review these criteria below.

1. $-51^\circ < \alpha_{J2000} < 57^\circ$.
2. There are photometric observations on at least five separate epochs between -20 days and $+60$ days relative to peak light in the SN rest-frame.
3. At least one epoch with signal-to-noise ratio > 5 in each of g, r, and i (not necessarily the same epoch in each passband).
4. At least one photometric observation at least two days *before* peak light in the SN rest frame.
5. At least one photometric observation at least ten days *after* peak light in the SN rest frame.
6. MLCS2k2 light curve fit probability > 0.01.
7. MLCS2k2 light curve fit parameter $\Delta > -0.4$.

5.2.2 SN Sample

In the entire redshift range of the SDSS-II Supernova Survey, there are 562 total SN candidates from the 2005-2006 observing seasons that satisfy the selection criteria. The redshift distribution for these SNe is shown in Figure 5.1. However, as will be discussed in §5.3, the systematic uncertainty on our sample selection becomes dominant for redshifts $z \gtrsim 0.2$, and not all of these SNe are useful for making precise

Table 5.1. Number of SN Ia for Rate Measurement

Redshift Limit	Confirmed	Photometric (Spect-z)	Photometric (Photo-z)	Total
0.15	45 (90%)	3 (6%)	2 (4%)	50
0.20	90 (68%)	27 (20%)	15 (11%)	132
0.25	133 (54%)	58 (24%)	57 (23%)	248
0.30	166 (46%)	83 (23%)	114 (31%)	363
∞	197 (35%)	109 (19%)	256 (46%)	562

measurement of the type Ia SN rate. The number of SNe for a few choices of an upper limit on the redshift range are given in Table 5.1. Spectroscopically confirmed SNe Ia from this sample are listed in Table 5.3.

SNe for which we have photometric observations of the light curve, but do not have any spectroscopic observations to determine the type of the SN are referred to as *photometric SNe*. Photometric SNe fall into 2 classes; (i) those that have a precisely (i. e. spectroscopically) measured redshift for their host-galaxy and (ii) those that do not have a precisely measured redshift for their host-galaxy. When the redshift for a photometric SN candidate is unknown, the candidate light curve is analyzed with the photo-z option in the flux-based MLCS light curve fitter (§4.2.2). A cosmology, and hence a distance versus redshift relation, is assumed in order to take advantage of knowledge of the absolute magnitude of type-Ia SNe in determining the redshift. In this procedure the small dispersion in intrinsic luminosity for type Ia SNe translates to photometric redshifts that are accurate to ≈ 0.02 (see Fig. 4.3). The number of SNe from categories (i) and (ii) that satisfy the selection criteria are given, for a few

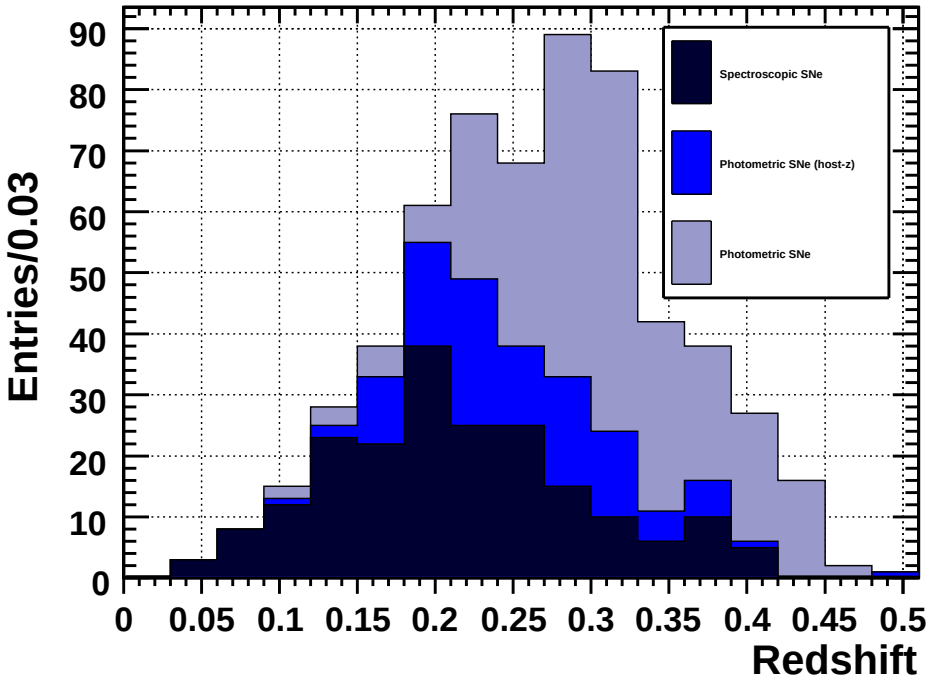

Figure 5.1: Redshift distribution for SN *passing* all selection criteria. The dark blue, blue and light blue shading represents confimed SNe Ia, photometric SNe *with* measured host-galaxy redshifts, and photometric SNe *without* measured host-galaxy redshifts, respectively.

choices of limiting redshift, in Table 5.1. SNe from categories (i) and (ii) are listed in Table 5.4 and Table 5.5, respectively.

Estimating Contamination from non-Ia SNe

Contamination of a photometric set of SNe Ia from non-Ia, core-collapse (CC) SNe is currently a significant limitation in studies of SNe Ia based on photometric measurements. CC SNe form a less homogeneous set than type Ia SNe and, in contrast to SNe Ia, no general parametric models exist to describe the light-curves for CC SNe. In addition, due to the use of type Ia SNe as cosmological tools, there is often an

explicit observational bias *against* CC SNe in modern SN surveys (Sako et al., 2008; Sullivan et al., 2006a). As the global set of well-observed SNe Ia has grown, this limitation for future SNe Ia studies has been recognized, and non-Ia SN observations are gaining increased attention (see e.g. Gal-Yam et al. (2005, 2007)).

For these reasons it is difficult to treat contamination of the set of photometric SNe from non-Ia SNe in the same way as SNe Ia, namely by modeling the SN survey observations of the underlying population with our SN MC. To place limits on the expected level of contamination of the photometric SN sample by CC SNe, we will instead consider the set of confirmed CC SNe from the SDSS-II Supernova Survey. There are 41 confirmed CC SNe from the first 2 years of the SDSS-II Supernova Survey, and an additional 38 from the 3rd year. The reason for the greater relative number of non-Ia SNe in the 3rd year is that, in addition to the usual SN Ia search, the 3rd season contained spectroscopic observing time on the Subaru telescope specifically allocated for a dedicated follow-up program for type-II SNe. The redshift distribution for confirmed non-Ia SNe from all 3 years of the SDSS-II Supernova Survey is shown in Figure 5.2. To investigate possible contamination from non-Ia SNe, we apply to the set of non-Ia SNe the same fits (to a SN Ia model) that are used in defining the SN Ia sample. From this set of confirmed non-Ia SNe, 2 satisfy the selection criteria for the SN Ia rate sample. These are SDSS-SN 8679 (2005jr), a confirmed type-IIn SN at a redshift of $z = 0.294$, and SDSS-SN 14492 (2006jo), a confirmed type-Ib SN at a redshift $z = 0.077$. The light-curve fits to the MLCS SN Ia model for these SNe are shown in Figure 5.3 and Figure 5.4. If we assume that the fraction of non-Ia SN that will satisfy the selection criteria, p_{CC}, is a random variable that follows a binomial distribution, then an observation of 2 successful events out of 71 in total gives 1-sigma limits on p_{CC} of $0.028^{+0.036}_{-0.018}$.

Some care must be taken in interpreting the fits to the confirmed non-Ia SNe as an

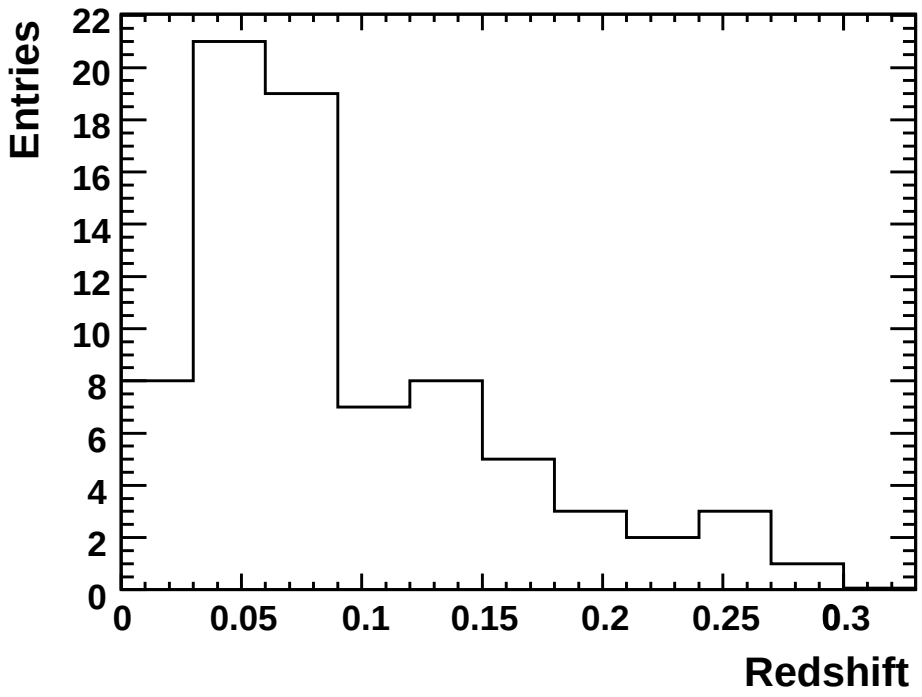

Figure 5.2: Redshift distribution for confirmed non-Ia SNe for the 2005-2007 observing seasons of the SDSS-II Supernova Survey.

estimate of the false positive rate. The spectroscopic incompleteness of the SDSS-II Supernova Survey for non-Ia SNe is not well constrained, but the set of confirmed non-Ia SNe is manifestly *not* complete. As mentioned above, the distribution of non-Ia SN light-curve properties is not well measured, and so it is difficult to evaluate whether the SDSS sample of non-Ia SNe is a representative sampling of the underlying population. However, as the SDSS-II Supernova Survey has a built in spectroscopic bias *against* non-Ia SNe (§2.2) it can plausibly be claimed that any bias in the SDSS-II Supernova Survey non-Ia sample is a bias *toward* the most "Ia-like" non-Ia SNe. With that being the case, our estimate of $\approx 3\%$ false positive rate for non-Ia SNe can be considered a conservative estimate.

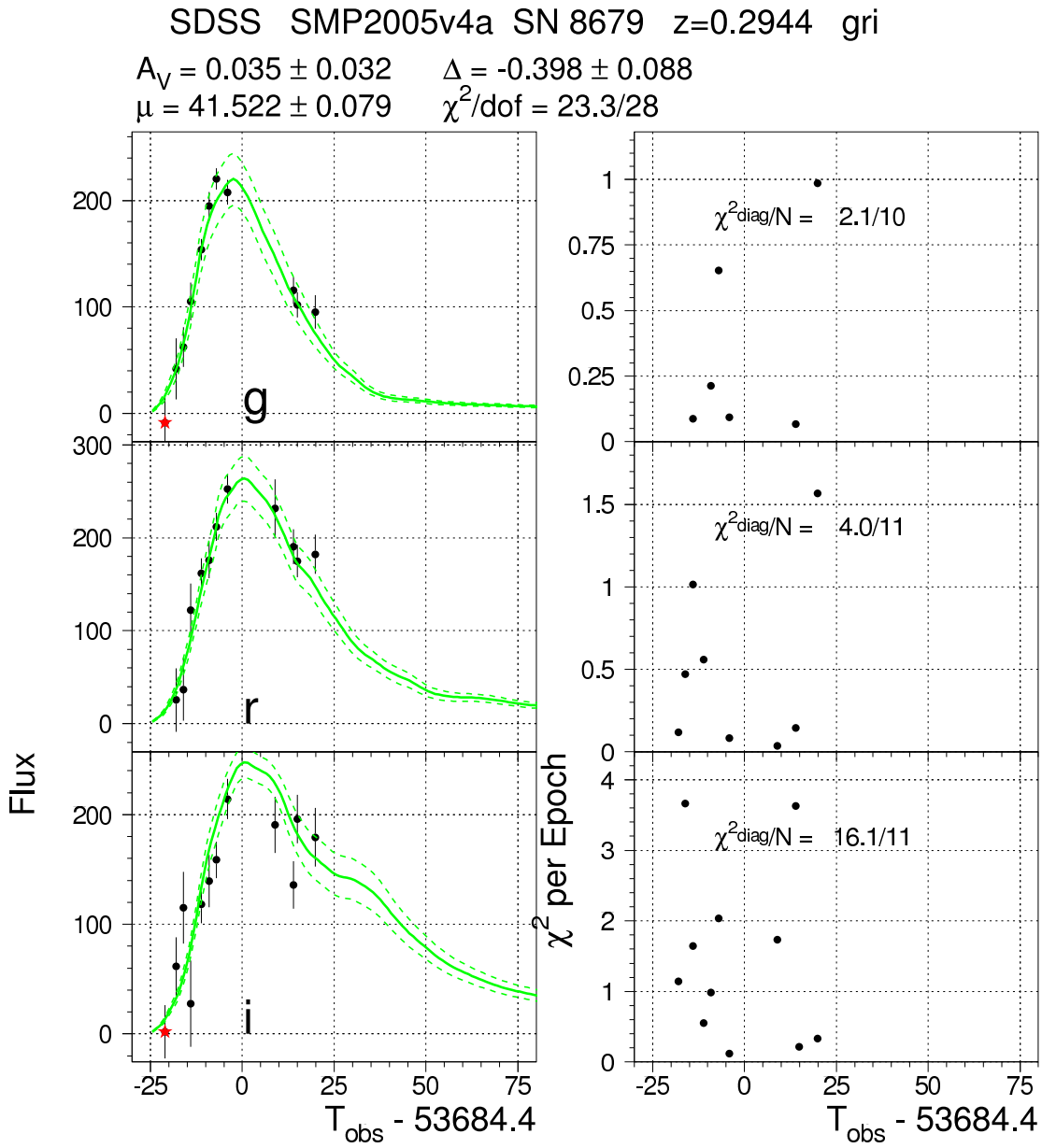

Figure 5.3: Light-curve fit for SN 8679. The left panels show the light curve fits in g (top), r (middle), and i (bottom). The filled circles represent the data. The solid line represents the best fitting model light curve and the dashed curves the 1-sigma model errors. Data points marked with a star are not used in the fit. The right panels show the contribution to the total χ^2 statistic as a function of light curve epoch.

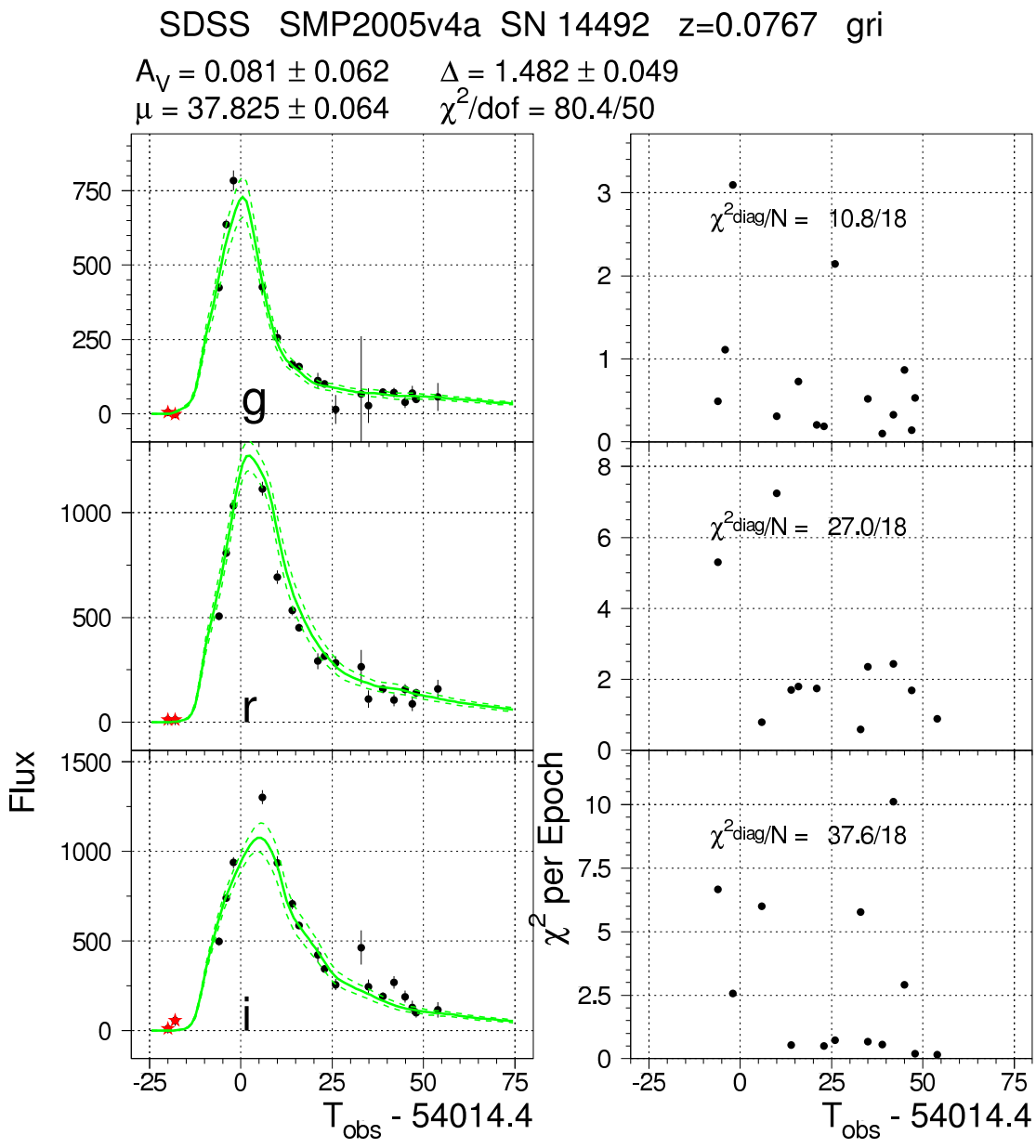

Figure 5.4: Light-curve fit for SN 14492. The left panels show the light curve fits in g (top), r (middle), and i (bottom). The filled circles represent the data. The solid line represents the best fitting model light curve and the dashed curves the 1-sigma model errors. Data points marked with a star are not used in the fit. The right panels show the contribution to the total χ^2 statistic as a function of light curve epoch.

5.3 Survey Efficiency

The use of fake SNe and the SN MC simulation to determine the discovery and selection efficiency has been discussed in detail in §4. Here I discuss the effect on the SN discovery efficiency of the modified selection procedure that uses statistics of the color-typing fits. To study the SN discovery efficiency for this SN rate analysis, we used the SN MC to generate a sample of $\approx 17,000$ MC SNe, which consists of ≈ 1000 SNe in each of 17 narrowly defined redshift bins, in the redshift range $0.025 < z < 0.4$. These MC SNe were filtered through a simulation of the search detection efficiency. That is, the efficiencies as a function of signal to noise ratio determined from the fakes, and shown in Figure 4.6, were applied to the simulated MC photometry. As in the search pipeline, a detection in at least 2 of the *gri* filters is required for the point to be considered to have been detected and to be included in the fit.

The simulated search photometry was then fit with the same color-typing code used during the search, and the cuts outlined in §5.2 were applied. The resulting selection efficiencies are shown in Figure 5.5. While this approach means that formally we are discarding confirmed SNe at low-redshifts ($z \lesssim 0.12$), where we have already demonstrated that the SN Survey is essentially complete, I emphasize that the color-typing code is extremely efficient at identifying low-redshift SNe Ia, and the effect on the sample size is expected to be negligible.

It is important to note that the color-typing can be done with or without utilizing forced photometry (§2.2), and with or without a prior on the SN redshift (from the host galaxy photometric or spectroscopic redshift measurement). The selection cuts are applied to fits that *do not* use forced photometry and *do not* use a prior on the SN redshift. While it is evident from examining the color-typing fits during the SN search campaign that utilizing forced photometry and/or a prior on the SN redshift in

many cases improves the ability to distinguish SNe Ia from their search photometry light-curves, it is significantly more difficult to model the selection function. The additional complications arise because forced photometry is applied non-uniformly to the candidates, and because modeling the distribution of host-galaxy photometric redshifts and their errors is non-trivial (Oyaizu et al., 2007).

Systematic Studies of the SN Discovery Efficiency

In §4.3.2, we considered the effect on the SN rate discovery efficiency of variation in the distribution of SN population parameters, and found that varying the distribution of extinction values had by far the largest effect. Here we repeat the procedure with the modified selection procedure. We vary the input extinction distribution for extinction values, $A_V \propto e^{-A_V/\tau}$, as $\tau = 0.35 \pm 0.1$. We find that for a low-extinction set of SNe, $\tau = 0.25$, the efficiency differs negligibly from the default value of $\tau = 0.35$. However, the efficiency for a high-extinction set of SNe, $\tau = 0.45$, differs markedly from the default set of SNe, particularly for redshifts $z \gtrsim 0.2$. Comparisons of the efficiency between the default and high-extinction sets of SNe is shown in Figure 5.5 (top row). As an additional systematic we assume that 5% of the photometric SNe Ia are CC SNe that have been misidentified.

5.4 SDSS SN Results

5.4.1 Constant Rate

I first consider interpretations of the SN observations described above under a model of the SN rate that is constant as a function of redshift.

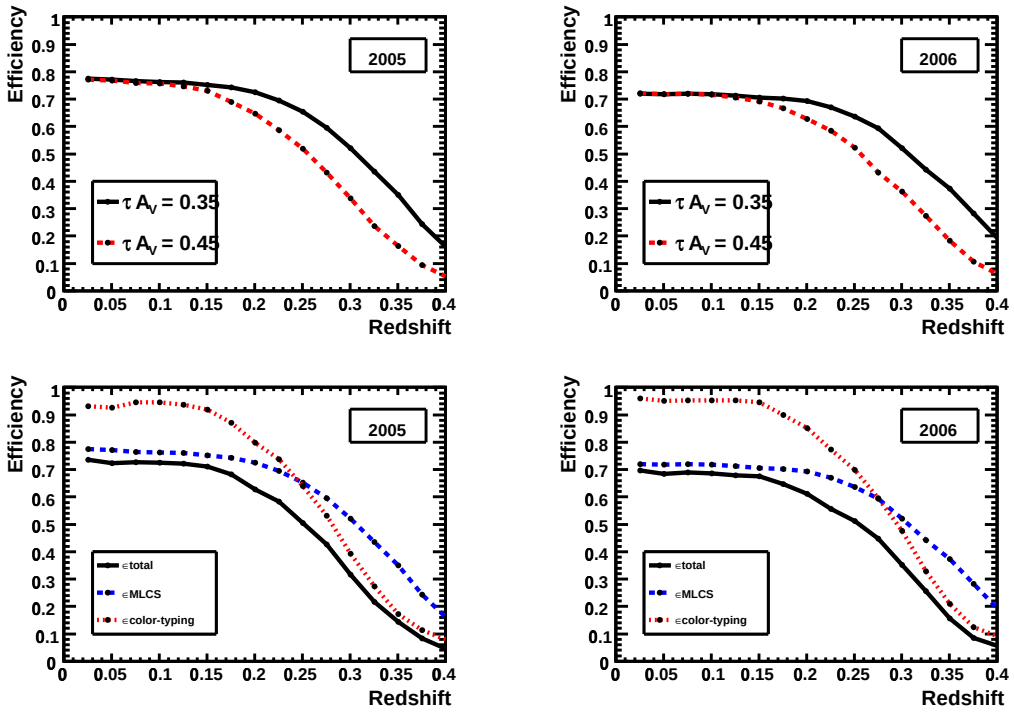

Figure 5.5: Results of studies of the SN discovery efficiency, as a function of redshift, based on MC SN samples. The left (right) columns show results of efficiency studies for the 2005 (2006) observing seasons. The top row shows the efficiency for 2 different assumptions about the distribution of the extinction parameter, A_V. The A_V distribution is assumed to have the form $e^{-A_V/\tau}$. The efficiency is shown for $\tau = 0.35$ (default) and for $\tau = 0.45$ (1 sigma upper limit). The values for $\tau = 0.25$ (1 sigma lower limit) are not shown since they are indistinguishable from the $\tau = 0.35$ values. The bottom row shows the SN selection efficiency for the color-typing (red/dashed), MLCS (blue/dashed) and combined (black/solid) selection criteria.

In a constant rate model, the volumetric rate is given by

$$r_V = \frac{N}{\widetilde{VT\epsilon}} \tag{5.1}$$

where,

$$\widetilde{VT\epsilon} = (\Theta T) \int_{z_{min}}^{z_{max}} dz\ \epsilon(z) u^2(z) \frac{du}{dz} \frac{1}{(1+z)}, \tag{5.2}$$

and $u(z)$, the comoving distance in the Friedmann-Robertson-Walker metric, is given by $u(z) = \int_0^z dz' \; c/H(z')$. For the SDSS-II Supernova Survey, the Earth-frame observation time for 2005 (2006) is 89 (90) days. The solid angle covered is $\Theta = 0.08277 * 0.98$ steradians. This value for Θ is 98% of the actual sky area covered by the survey, due to the masking of bright stars and variable sources.

The value of the volumetric SN Ia rate, as a function of the upper redshift limit for the SN sample, and derived under the assumption of a constant rate model, is shown in Figure 5.6. The value for a redshift cutoff of $z = 0.12$ is lower than that derived based on the first year data (§4, Dilday et al. (2008)). I note that in the 2006 sample of spectroscopically confirmed type Ia SNe, there are 11 SNe Ia at $z \leq 0.12$ that peaked during the survey observation window, compared to 19 in the first year SN sample. The time of peak brightness is a simple feature of the light-curve that is not strongly dependent on assumptions about the SN Ia light-curve model or underlying distributions, and is therefore a robustly determined quantity when the light-curve is well sampled. Therefore it is seen that the 2005 and 2006 SN yields in fact differ by a $\approx 1\sigma$ statistical fluctuation, and this is the cause of the reduced low-redshift rate when including the 2nd SN search campaign. This simple accounting of SNe is independent of the additional color-typing component of the selection criteria, which in principle could be introducing a bias in the SN rate results.

5.4.2 Rate as a Function of Redshift

In Figure 5.7, we plot the volumetric SN Ia rate, in running bins of width $\Delta z = 0.05$. The rate in each bin is computed by assuming the rate to be constant within the bin, which is valid to a good approximation for the small bins considered. The SN rate values are listed in Table 5.2. It can be seen that the systematic uncertainty on the

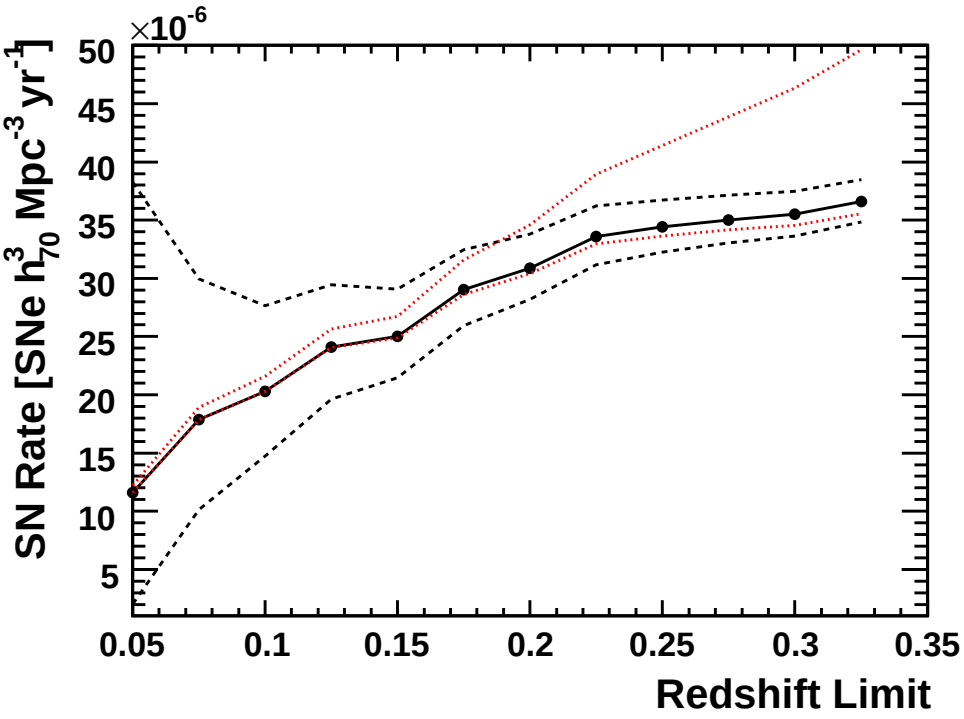

Figure 5.6: SN rate, for a constant rate model, as a function of upper limit on the redshift range. The black/dashed lines show the 1-sigma statistical (Poisson) errors. The red/dotted lines show estimates of the systematic errors, which includes uncertainty on the SN extinction distribution and estimation of contamination of the SN sample.

selection function (due to uncertainty on the extinction distribution) becomes much larger than the statistical uncertainty for $z \gtrsim 0.2$.

The values for the SN Ia rate at $z = 0.1$ and $z = 0.2$ are seen to differ by $\approx 1.9\sigma$. A fit of these rate values to a linear model of rate vs. redshift, over the redshift range $0.1 < z < 0.2$, gives a slope of $(1.45^{+1.07}_{-0.90}) \times 10^{-4}$ SNe yr^{-1} Mpc^{-3} h^3_{70}. Fitting a power-law model, $r_V(z) = A\ (1+z)^{\beta}$, over the same redshift range gives $\beta = 5.16^{+3.84}_{-3.29}$; that is, a constant SN rate ($\beta = 0$) is ruled out with $\approx 1.6\sigma$ significance. The χ^2 values for the linear and power-law model fits (1 degree of freedom) are $\approx 1 \times 10^{-2}$ and $\approx 4 \times 10^{-2}$, respectively. For comparison, the fit of a power-law

Table 5.2. SN Rate vs. Redshift

Redshift	SN Rate $[10^{-5}$ SNe yr^{-1} Mpc^{-3} $h_{70}^3]$
0.05	$1.86^{+1.26+0.11}_{-0.80-0.00}$
0.10	$2.49^{+0.63+0.17}_{-0.51-0.01}$
0.15	$3.28^{+0.48+0.34}_{-0.42-0.07}$
0.20	$3.89^{+0.42+0.98}_{-0.38-0.09}$
0.25	$3.77^{+0.38+1.78}_{-0.35-0.13}$
0.30	$4.18^{+0.43+3.58}_{-0.39-0.17}$

Note. — The errors given are statistical and systematic, respectively

model to a set of published rates measurements discussed in §4.5.4 gave $\beta = 1.5 \pm 0.6$. It should be noted that the power-law model is used as a simple parameterization of the SN rate as a function of redshift, and to formally test the hypothesis that the SN rate is an increasing function of redshift. There is no fundamental reason to expect that the exponents, when considering different redshift ranges, should be identical.

Despite the large systematic uncertainty on the discovery efficiency in the redshift range $0.2 < z < 0.3$, this study represents the first statistically significant measurement of the SN Ia rate in this redshift range. As can be seen, the direction of the systematic uncertainty is to increase the SN rate, and the lower limits provided here are quite robust.

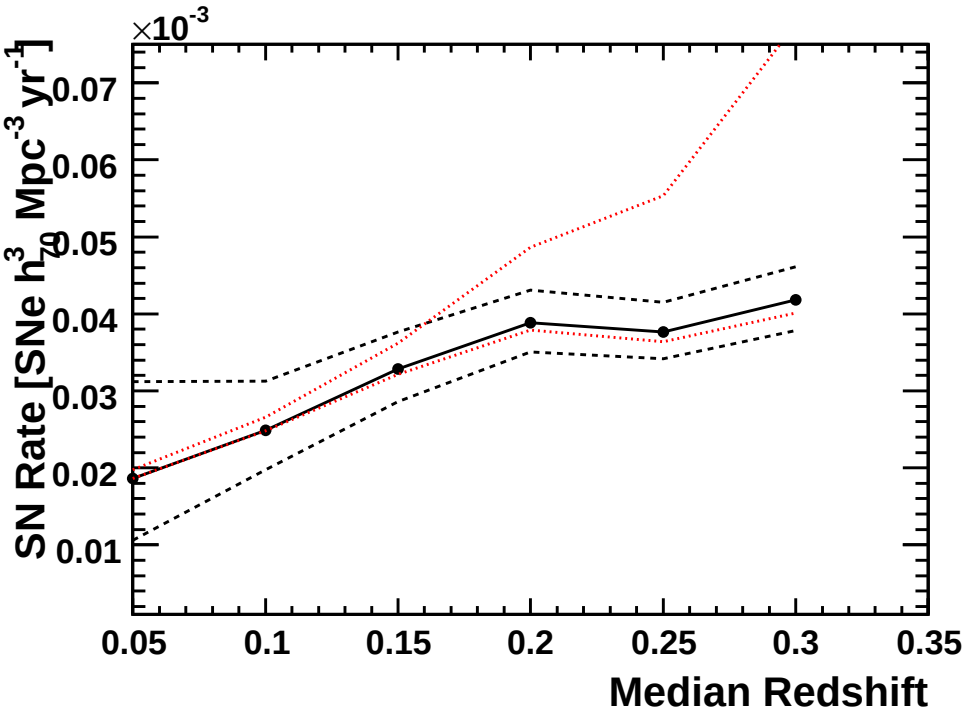

Figure 5.7: SN rate as a function of the median redshift of running bins of size $\Delta z = 0.05$. The SN rate is computed assuming that the rate is constant in each bin. The black/dashed lines show the 1-sigma statistical (Poisson) errors. The red/dotted lines show estimates of the systematic errors, which includes uncertainty on the SN extinction distribution and estimation of contamination of the SN sample.

5.5 Summary of Rate vs. Redshift Studies

In this Chapter we have extended studies of the volumetric SN rate (§4, Dilday et al. (2008)) to a higher redshift limit, based on the first 2 years of the SDSS-II Supernova Survey. The sample of SNe considered comprises ≈ 350 SNe Ia at $z < 0.3$. This total includes 132 at $z < 0.2$, with the majority (68%) being spectroscopically confirmed.

These SN Ia rate measurements constrain the slope of the SN vs. redshift relation in the redshift range $0.1 < z < 0.2$ to be $dr_V/dz = (1.45^{+1.07}_{-0.90}) \times 10^{-4}$ SNe yr^{-1} Mpc^{-3} h^3_{70}. Additionally we have presented the first statistically significant SN Ia rate measurements in the redshift range $0.2 < z < 0.3$. The results presented

here represent an order of magnitude improvement in the statistics for SN Ia rate measurements in the same redshift range, and solidify the SN Ia rate constraints for $z < 0.3$.

Table 5.3: Confirmed SNe Ia in the Rate Sample

SN Id	Ra	Decl	Redshift	Fitprob
762	+15.535165	-0.879083	0.1915	0.944
1032	+46.795666	+1.119523	0.1297	0.401
1112	-20.982382	-0.375271	0.2577	0.554
1166	+9.355588	+0.973216	0.3824	0.748
1241	-22.327515	-0.776642	0.0870	0.992
1253	-36.201069	+0.163013	0.2620	0.824
1371	-10.626243	+0.429292	0.1191	0.896
1580	+45.322945	-0.644122	0.1830	1.000
1688	-38.642315	+0.324480	0.3587	0.759
2017	-31.056742	+0.593424	0.2616	0.935
2031	-47.956875	-1.171496	0.1530	0.804
2165	+17.091644	-0.096385	0.2880	0.803
2246	+50.090328	-0.885660	0.1952	0.987
2308	+34.272736	+0.280203	0.1480	0.860
2330	+6.807011	+1.120527	0.2132	0.892
2372	+40.520657	-0.540883	0.1812	0.984
2422	+1.994446	+0.638106	0.2650	0.622
2440	+42.633595	+0.807733	0.1930	0.983
2533	+31.220621	-0.326553	0.3400	0.533
2561	+46.343353	+0.858294	0.1182	0.999
2635	+52.704254	-1.238155	0.1433	0.991

Continued on Next Page...

Table 5.3 – Continued

SN Id	Ra	Decl	Redshift	Fitprob
2689	+24.900272	-0.758795	0.1615	0.344
2789	-15.798567	+0.401017	0.2903	0.156
2916	-44.078316	+0.569487	0.1242	0.653
2943	+17.704912	+1.007835	0.2654	0.144
2992	+55.496910	-0.782686	0.1266	0.627
3080	+16.932318	-1.039553	0.1742	0.999
3087	+20.406666	-0.977300	0.1646	1.000
3199	-26.707512	+1.050427	0.2511	0.330
3241	-47.348564	-0.354162	0.2589	0.293
3256	-30.732330	-0.223529	0.1076	0.632
3331	+34.561340	+0.796448	0.2060	0.823
3377	+54.156067	+1.079081	0.2451	0.628
3451	-25.930792	+0.708054	0.2500	0.541
3452	-25.328611	+0.639063	0.2304	0.918
3592	+19.052416	+0.791834	0.0866	1.000
3901	+14.850375	+0.002537	0.0628	1.000
4046	-5.501751	+0.642010	0.2770	0.879
4241	+12.237569	-0.905835	0.3320	0.244
4577	+38.475445	+0.280624	0.3630	0.943
4679	+21.528265	+0.676797	0.3324	0.152
5103	-0.115622	+0.737106	0.1460	0.997

Continued on Next Page...

Table 5.3 – Continued

SN Id	Ra	Decl	Redshift	Fitprob
5395	+49.640835	+0.123272	0.1170	1.000
5533	-31.330118	+0.413381	0.2197	0.932
5549	+3.250486	+0.248148	0.1210	0.998
5550	+3.598186	+0.332952	0.1562	0.997
5635	-26.817295	-0.035008	0.1795	0.870
5717	+17.895884	-0.005938	0.2517	0.890
5736	+22.862652	-0.631667	0.2530	0.926
5737	+22.856920	-0.603443	0.3930	0.944
5751	+11.634124	+0.838124	0.1300	0.988
5844	-32.213806	-0.843035	0.3108	0.884
5916	+5.437276	-0.325109	0.1724	0.985
5957	+34.760532	-0.272926	0.2796	0.585
5994	-47.397560	-0.167953	0.1870	0.989
6057	+52.553543	-0.974673	0.0671	1.000
6108	+1.806559	+0.348877	0.2595	0.992
6192	-11.535069	+1.256882	0.2720	0.721
6196	-22.368925	-0.502788	0.2807	0.925
6249	+3.265478	-0.620192	0.2944	0.953
6295	+23.672979	-0.605451	0.0796	0.028
6304	+26.497499	+1.195896	0.1900	0.880
6315	-49.517277	+1.091898	0.2670	0.648

Continued on Next Page...

Table 5.3 – Continued

SN Id	Ra	Decl	Redshift	Fitprob
6406	+46.088593	-1.063022	0.1246	1.000
6422	-10.861311	-0.663264	0.1840	0.938
6558	+21.701641	-1.238156	0.0574	0.999
6649	+34.275829	+0.534720	0.3140	0.509
6699	-37.185101	-1.057078	0.3106	0.959
6780	-31.931484	+0.266987	0.2020	0.975
6933	+11.351676	+1.075463	0.2130	0.887
6936	-36.766190	-0.699864	0.1810	0.900
7143	-14.737671	-0.207482	0.3040	0.681
7147	-9.981691	-0.055565	0.1099	0.247
7243	-31.920958	+0.471857	0.2037	0.984
7335	-41.114864	-0.355408	0.1975	0.641
7473	+4.326311	-0.257352	0.2160	0.851
7475	+4.753400	-0.281566	0.3220	0.582
7512	+52.090214	-0.326167	0.2190	0.517
7779	-49.919827	-0.007236	0.3812	0.399
7847	+32.459843	-0.061855	0.2124	0.896
7876	+19.182377	+0.794520	0.0764	0.392
7947	-45.813992	+0.408286	0.3680	0.276
8030	+40.208656	+0.993058	0.4220	0.999
8046	+39.116718	+0.511177	0.2593	0.992

Continued on Next Page...

Table 5.3 – Continued

SN Id	Ra	Decl	Redshift	Fitprob
8213	-2.479202	-0.921470	0.1847	0.937
8495	-24.739008	-0.748205	0.2144	0.874
8598	+42.667236	-0.066006	0.3606	0.968
8707	+41.236122	+0.203556	0.3951	0.964
8719	+7.721406	-0.718937	0.1163	0.335
9032	-22.115486	-0.493656	0.2540	0.995
9045	-12.162980	-0.608671	0.3895	0.887
9467	-31.048681	+1.180688	0.2184	0.394
10550	-10.324667	-1.204922	0.3001	0.527
12780	-37.845531	+1.227996	0.0500	0.967
12843	-36.122005	-0.980350	0.1670	0.991
12853	-43.234531	+0.723020	0.1694	0.536
12855	-29.744499	+0.716125	0.1707	0.006
12856	-27.134544	+0.755840	0.1717	0.954
12860	-36.305885	+1.175798	0.1217	0.956
12874	-6.035521	-0.177241	0.2449	0.495
12898	+26.793016	-0.147075	0.0835	0.991
12930	-50.317287	-0.474595	0.1475	1.000
12950	-8.332567	-0.840308	0.0827	0.133
12972	+7.958495	-0.383025	0.2610	0.988
12977	+13.695534	-0.250963	0.2470	0.993

Continued on Next Page...

Table 5.3 – Continued

SN Id	Ra	Decl	Redshift	Fitprob
13025	-18.432825	+0.415772	0.2241	0.709
13038	-12.173282	+0.504507	0.1010	0.996
13044	-27.457285	+0.503218	0.1257	0.998
13070	-2.214979	-0.746447	0.1986	0.680
13072	-25.040682	+0.024305	0.2306	0.638
13136	+6.140620	-0.279124	0.3721	0.083
13152	+7.051999	+0.117924	0.2030	0.941
13174	+13.234653	+0.447753	0.2360	0.985
13305	-28.899570	+0.691094	0.2139	0.797
13354	+27.564739	-0.887354	0.1576	0.325
13506	+25.243195	-0.727929	0.2450	0.053
13511	+40.612232	-0.794202	0.2376	0.144
13578	+17.394642	+0.704040	0.2000	0.297
13641	-14.781359	-0.981226	0.2200	0.823
14157	+51.136616	+1.022300	0.2140	0.037
13727	-42.411968	+0.932552	0.2257	0.230
13736	-23.166744	+1.030894	0.1504	0.923
13757	-9.876961	-1.157926	0.2890	0.824
13796	-9.308531	+0.532782	0.1450	0.979
13835	+6.059599	-0.248318	0.2477	0.733
13894	+1.690506	-0.036844	0.1249	0.887

Continued on Next Page...

Table 5.3 – Continued

SN Id	Ra	Decl	Redshift	Fitprob
13934	-17.889029	-0.435261	0.3300	1.000
13956	+20.941742	+0.816645	0.2620	0.313
14019	-43.357643	-0.648002	0.2164	0.434
14024	-41.801495	+0.916261	0.2000	0.154
14108	+53.594551	-1.123299	0.1227	0.831
14212	-29.529982	+1.044906	0.2054	0.830
14261	-31.759708	+0.253713	0.2860	0.683
14279	+18.488695	+0.371563	0.0454	0.551
14284	+49.049191	-0.601036	0.1811	0.204
14298	-45.104961	+1.223240	0.2680	0.619
14377	+48.264271	-0.471711	0.1400	0.645
14397	+6.916010	+0.649433	0.3857	0.530
14437	-27.919119	-1.196431	0.1491	0.891
14735	+35.157921	+0.348310	0.3011	0.084
14816	-23.283739	+0.505992	0.1072	0.127
14846	+7.663188	+0.141478	0.2247	0.986
14871	+54.277039	+0.009272	0.1276	0.991
14979	+54.946407	+0.992738	0.1771	0.805
14984	-46.166515	-0.092828	0.1967	0.454
15002	+22.249660	+0.769842	0.3800	0.137
15009	+32.798515	+0.695780	0.2950	0.596

Continued on Next Page...

Table 5.3 – Continued

SN Id	Ra	Decl	Redshift	Fitprob
15057	+17.881159	+0.409397	0.1905	0.191
15132	-30.299864	+0.197628	0.1440	0.719
15136	-8.837590	-0.718434	0.1490	0.031
15161	+35.842754	+0.818970	0.2500	0.193
15201	-22.480604	+0.003588	0.2085	0.199
15203	+15.734637	+0.183022	0.2043	0.993
15213	+53.019089	-0.100226	0.3112	0.947
15219	+34.611000	+0.226591	0.2470	0.912
15222	+2.853209	+0.702673	0.1994	0.979
15229	+4.831940	+1.090581	0.2268	0.084
15234	+16.958265	+0.828100	0.1363	0.965
15254	-46.507137	-0.360107	0.2010	0.002
15259	-22.455929	-0.407872	0.2100	0.541
15287	-36.040352	-1.057525	0.2740	0.676
15301	-36.420116	+0.589061	0.2963	0.658
15354	+6.773583	-0.126063	0.2221	0.003
15356	-24.946735	+0.409848	0.2747	0.746
15365	-5.443421	+1.249015	0.1875	0.788
15369	-11.167143	-0.562668	0.2450	0.949
15421	+33.741486	+0.602392	0.1850	0.968
15425	+55.561028	+0.478196	0.1600	0.126

Continued on Next Page...

Table 5.3 – Continued

SN Id	Ra	Decl	Redshift	Fitprob
15433	+14.879625	-0.256620	0.2200	0.691
15440	+39.720631	+0.090006	0.2619	0.150
15443	+49.867363	-0.318123	0.1820	0.217
15453	-40.331776	-1.024385	0.1477	0.997
15456	-28.132879	-0.903488	0.3821	0.896
15459	-19.298603	-0.901838	0.1250	0.852
15461	-33.152584	-0.494770	0.1800	0.973
15466	-42.355019	-0.123285	0.2461	0.810
15508	+27.168867	-0.576666	0.1460	0.998
15583	+37.730957	+0.946202	0.1752	0.905
15584	+43.495365	+0.986912	0.2820	0.989
15648	-46.281734	-0.194897	0.1750	0.066
15674	-19.170868	+0.262848	0.1970	0.384
15776	+32.829376	-0.998278	0.3176	0.352
15704	+40.210712	+0.658702	0.3650	0.852
15868	+38.099812	-0.713699	0.2510	0.871
15872	+36.722424	-0.327917	0.1846	0.088
15897	+11.681457	-1.032940	0.1747	0.447
15901	+31.976215	-0.535482	0.1710	0.549
16000	+21.117533	+0.074305	0.3985	0.861
16021	+13.843590	-0.388883	0.0947	0.539

Continued on Next Page...

Table 5.3 – Continued

SN Id	Ra	Decl	Redshift	Fitprob
16032	+44.069099	-0.410825	0.1950	0.430
16072	+3.124366	-0.977378	0.2867	0.921
16073	+8.107599	-1.054066	0.1531	0.997
16093	-9.637568	+1.132362	0.3351	0.966
16100	+30.436174	-1.032490	0.1900	0.447
16185	+16.868010	-0.269455	0.0970	0.997
16211	-11.836029	+0.266796	0.3110	0.834
16276	+20.578695	+1.010544	0.1600	0.958

Table 5.4: SNe with Spectroscopic Redshifts in the Rate Sample

SN Id	Ra	Decl	Redshift	Fitprob
703	-23.782131	+0.650585	0.3000	0.866
779	+26.673695	-1.020721	0.2377	0.936
911	+38.690674	-0.115710	0.2080	0.857
1008	+28.278086	+1.113693	0.1200	0.095
1415	+6.106478	+0.599204	0.2120	0.062
1740	+5.404279	-0.880995	0.1673	0.321
2057	-39.600300	-0.317030	0.2120	0.750
2162	+15.442415	-0.133683	0.1760	0.483
2532	+27.747414	-0.234263	0.2700	0.415
2632	+45.590130	-1.226095	0.2960	0.250
2639	-29.535904	+0.664463	0.2150	0.523
2734	+48.206856	-0.694863	0.1550	0.932
2806	+45.266899	+0.273640	0.2590	0.404
2864	-0.549082	-1.239595	0.2441	0.444
3049	-29.776556	-1.236555	0.1680	0.895
3195	+8.668299	+0.244205	0.3000	0.768
3488	-46.444836	-1.010427	0.1600	0.027
3535	+44.117237	-0.133554	0.3080	0.979
3892	+18.686029	-0.452214	0.3500	0.033
4019	+1.261779	+1.145343	0.1810	0.887

Continued on Next Page...

Table 5.4 – Continued

SN Id	Ra	Decl	Redshift	Fitprob
4059	+54.649906	+0.145748	0.3000	0.111
4181	+37.817760	-1.131004	0.2900	0.912
4236	+1.905610	-1.018380	0.3432	0.827
4281	+33.367344	-0.968310	0.2132	0.993
4307	+29.962479	+0.949618	0.2720	0.992
4311	+32.130825	+1.019885	0.2953	0.056
4676	+18.823647	+0.788048	0.2446	0.083
4690	+32.929462	+0.688171	0.2000	0.126
5473	-5.263457	+0.383429	0.2800	0.824
5486	-26.752029	-0.412051	0.2300	0.603
5524	-43.421352	-0.990351	0.3200	0.963
5673	-6.198760	+0.784193	0.3793	0.888
5785	-31.402615	+0.083764	0.1480	0.383
5890	-27.484442	+0.609156	0.1770	0.999
5959	+38.059757	-0.308211	0.1980	0.929
5963	+11.080997	+0.479400	0.2356	0.999
5993	+29.682386	+0.048967	0.3767	0.412
6275	+34.589737	+0.029923	0.2730	0.114
6479	-39.592785	+0.583495	0.2360	0.885
6614	+26.646919	+0.866741	0.1690	0.224
6714	-2.640027	+0.631759	0.4137	0.176

Continued on Next Page...

Table 5.4 – Continued

SN Id	Ra	Decl	Redshift	Fitprob
6807	-21.930908	-1.145698	0.2950	0.174
6813	+27.270218	+0.057005	0.2860	0.737
6851	+52.104443	-0.048616	0.3050	0.916
6861	-10.567738	-1.113527	0.1900	0.218
6895	-29.807095	+0.928189	0.2170	0.762
6903	-24.556484	+0.971700	0.2530	0.860
7051	-1.458145	+0.024961	0.3300	0.978
7092	-43.719597	+1.220425	0.2250	0.975
7102	-35.380180	-0.615673	0.1964	0.045
7258	-38.770119	-0.999125	0.2560	0.854
7363	+17.963448	-0.782157	0.1800	0.393
7373	-7.195184	+0.588214	0.2820	0.590
7431	-19.045631	-0.275011	0.3500	0.980
7444	+27.702925	+0.429734	0.2499	0.844
7457	-9.096928	-0.372238	0.2540	0.843
7527	-24.743660	-1.204141	0.2370	0.930
7644	-6.065021	+0.868265	0.3100	0.331
7701	+6.516941	-1.228857	0.3600	0.715
7824	-11.186970	-0.080901	0.2910	0.384
7954	-27.323069	+0.347712	0.2550	0.882
8114	-7.783380	+0.228332	0.3750	0.509

Continued on Next Page...

Table 5.4 – Continued

SN Id	Ra	Decl	Redshift	Fitprob
8165	+50.225288	-1.109399	0.3190	0.986
8254	-8.836246	+0.819797	0.1890	0.026
8555	+2.915440	-0.414963	0.1980	0.302
8607	-36.413097	+0.151906	0.2600	0.597
9155	-32.645611	-0.784758	0.3040	0.966
9326	-15.683831	+0.628369	0.3500	0.338
9594	+17.714249	+0.121631	0.2980	0.014
12804	+18.201574	+1.040182	0.1300	0.957
12852	-45.746941	+0.689139	0.2640	0.308
13224	+47.494915	-0.245911	0.2360	0.889
13411	-44.810120	+0.191602	0.1630	0.988
13689	+4.016027	+0.807476	0.2500	0.868
13703	+39.013634	+1.253413	0.2400	0.807
13840	-46.293655	+0.124991	0.2400	0.015
13864	-11.425954	+0.191012	0.2700	0.737
13907	+14.179293	+0.232226	0.2000	0.871
14186	-22.149513	+0.992205	0.3150	0.092
14317	-44.429348	+0.330210	0.1810	0.999
14333	+16.285246	-0.012705	0.2710	0.491
14372	+50.811829	-0.141317	0.3800	0.002
14375	+37.876839	-0.573287	0.3210	0.062

Continued on Next Page...

Table 5.4 – Continued

SN Id	Ra	Decl	Redshift	Fitprob
14445	-19.037378	-0.754009	0.2380	0.248
14525	+16.882721	+0.477105	0.1500	0.940
14545	-8.251869	+1.017142	0.2780	0.944
14589	+48.012074	-0.677608	0.2700	0.892
14784	-36.201633	-0.348273	0.1920	0.332
15325	+32.298229	-0.742454	0.2140	0.839
15343	-36.327675	+0.684753	0.1740	0.772
15353	-9.708446	-0.175873	0.3100	0.374
15454	-32.140640	-0.848134	0.3830	0.983
15467	-39.980198	-0.177548	0.2100	0.876
15587	+54.417168	+0.998247	0.2190	0.106
15675	-16.826370	+0.364142	0.2200	0.898
15722	+55.350544	+1.194496	0.1900	0.440
15748	+48.114418	-0.130724	0.1560	0.751
15755	-1.596887	+0.226288	0.2810	0.092
15765	+32.847115	+0.246027	0.3050	0.544
15784	-3.326376	-0.615412	0.2700	0.836
15806	+24.092169	-0.830701	0.2500	0.661
15823	-45.747437	+0.199008	0.2150	0.957
15892	-36.801048	+0.689379	0.1850	0.432
15909	+11.314829	+0.796676	0.2180	0.031

Continued on Next Page...

Table 5.4 – Continued

SN Id	Ra	Decl	Redshift	Fitprob
16091	+50.190033	+0.841804	0.3000	0.985
16103	-47.024929	-1.050174	0.2020	0.322
16163	+31.499180	-0.855782	0.1600	0.335
16462	+17.040585	-0.386483	0.2450	0.073
16466	-40.591591	+0.103231	0.1880	0.166

Table 5.5: SNe with Photometric Redshifts in the Rate Sample

SN Id	Ra	Decl	Redshift	Redshift Error	Fitprob
822	+40.560692	-0.862174	0.2111	0.0200	0.064
841	+48.495941	-1.010063	0.2935	0.0139	0.988
1342	-13.472594	+0.116888	0.2828	0.0191	0.995
1403	-0.296157	+0.431891	0.2963	0.0539	0.010
1658	-2.495566	+0.650080	0.2677	0.0242	0.852
1921	-44.299973	+0.842507	0.3554	0.0276	0.726
2081	-22.694910	-1.207809	0.2588	0.0234	0.066
2319	+55.465485	+0.345629	0.1593	0.0054	0.999
2784	+28.075249	-0.041696	0.3796	0.0207	0.971
2855	+16.175179	-0.356419	0.2301	0.0170	0.994
2871	+9.347647	-1.086742	0.3233	0.0308	0.404
3077	-30.956190	+0.215300	0.1592	0.0096	0.919
3206	+13.577422	+0.418196	0.4236	0.0197	0.004
3368	+44.455944	+1.230838	0.3266	0.0249	0.589
3417	-45.723927	+0.978246	0.2598	0.0151	0.639
3506	-23.749327	-0.978191	0.2092	0.0089	0.924
3881	-8.118376	-0.441823	0.3181	0.0196	0.680
3945	-13.990948	-0.283072	0.2625	0.0161	0.309
3975	+29.820969	+0.203640	0.3955	0.0195	0.361
3983	+7.275811	-0.256650	0.2869	0.0180	0.460

Continued on Next Page...

Table 5.5 – Continued

SN Id	Ra	Decl	Redshift	Redshift Error	Fitprob
4028	+11.013855	+1.242443	0.3150	0.0313	0.660
4035	+21.467321	+1.047487	0.3419	0.0262	0.017
4044	+33.415249	+1.240871	0.3822	0.0272	0.721
4079	+29.206652	+0.754040	0.4160	0.0146	0.177
4360	+19.655813	+0.915759	0.3263	0.0180	0.834
4558	+29.885477	+0.290103	0.3148	0.0453	0.442
4572	+36.268456	+0.395997	0.4085	0.0283	0.436
4578	+38.596588	+0.311300	0.3347	0.0288	0.859
4714	+37.152367	-0.205492	0.4329	0.0151	0.372
4757	+34.146717	-1.015725	0.4239	0.0197	0.909
4803	+32.564014	+0.302029	0.3983	0.0213	0.634
5199	-11.207582	-0.994946	0.2483	0.0207	0.750
5235	-22.775742	+0.636080	0.2193	0.0330	0.037
5378	+37.736755	-1.252205	0.2343	0.0089	0.044
5468	-17.469336	+0.404756	0.2816	0.0157	0.995
5543	-3.140961	+0.303251	0.3317	0.0212	0.632
5702	+12.583263	-0.919158	0.2188	0.0090	0.984
5731	+11.338489	-0.544509	0.3760	0.0249	0.636
5735	-48.341183	+0.650573	0.2265	0.0174	0.600
5792	-31.285805	-1.237852	0.2307	0.0340	0.390
5802	-31.854973	+0.845613	0.2869	0.0140	0.961

Continued on Next Page...

Table 5.5 – Continued

SN Id	Ra	Decl	Redshift	Redshift Error	Fitprob
5803	-24.020086	+0.932250	0.2781	0.0209	0.113
5917	+6.036846	-0.255145	0.2620	0.0193	0.990
6055	+37.906307	-0.896006	0.4040	0.0203	0.957
6225	+0.287436	-1.000400	0.3370	0.0260	0.377
6282	-40.668613	-0.489767	0.3697	0.0353	0.926
6491	+16.648857	+0.542503	0.2323	0.0158	0.034
6501	-44.843193	+0.131429	0.3499	0.0246	0.983
6530	+14.329072	+0.021290	0.1512	0.0095	0.614
6560	-38.553432	+0.849777	0.2932	0.0270	0.055
6618	+41.919571	+0.964160	0.3108	0.0224	1.000
6889	-33.280098	+0.909463	0.2937	0.0467	0.806
6912	-44.267632	-0.642582	0.3582	0.0369	0.916
6914	-42.760509	-0.780765	0.4148	0.0182	0.124
7205	+44.107216	+0.695057	0.3150	0.0144	0.428
7119	-44.011459	-0.070424	0.3221	0.0272	0.666
7304	+24.835941	-0.656209	0.2573	0.0120	0.935
7357	-38.364113	-0.362666	0.4009	0.0234	0.629
7365	-7.682836	+0.579756	0.4007	0.0239	0.813
7479	+7.225731	-0.409545	0.2059	0.0176	0.797
7550	-38.306023	+1.050803	0.3300	0.0309	0.835
7636	-39.144909	+0.118799	0.3999	0.0207	0.679

Continued on Next Page...

Table 5.5 – Continued

SN Id	Ra	Decl	Redshift	Redshift Error	Fitprob
7654	+2.472380	+0.964465	0.3854	0.0189	0.995
7656	+7.754791	+1.010678	0.3321	0.0515	0.254
7699	+6.238651	-1.215750	0.3528	0.0234	0.418
7712	+10.959782	-1.240849	0.3826	0.0339	0.586
7717	+14.440524	-1.232635	0.3294	0.0255	0.673
7802	-14.424070	+0.729074	0.3056	0.0215	0.481
7803	-13.913658	+0.690414	0.3947	0.0314	0.038
7857	-24.722034	+1.185072	0.4140	0.0201	0.386
7884	+21.767372	+0.123386	0.3403	0.0359	0.977
8092	+50.151157	+0.093876	0.3268	0.0237	0.744
8118	-4.141293	+0.297140	0.4105	0.0221	0.531
8138	+11.466606	+0.378051	0.3338	0.0285	0.818
8226	-25.182802	+0.749110	0.4305	0.0147	0.424
8280	+8.573611	+0.795945	0.3564	0.0317	0.780
8297	+24.974503	+0.691450	0.2503	0.0169	0.759
8323	+49.486015	+0.705368	0.4212	0.0222	0.658
8351	+12.112004	+1.254238	0.4307	0.0127	0.875
8700	+35.109612	+0.227065	0.3912	0.0359	0.379
8705	+40.433060	+0.268717	0.3712	0.0330	0.313
8793	+11.937724	-0.564654	0.3847	0.0355	0.380
9052	+21.041143	-0.483073	0.2396	0.0156	0.939

Continued on Next Page...

Table 5.5 – Continued

SN Id	Ra	Decl	Redshift	Redshift Error	Fitprob
9109	+26.388950	+0.850636	0.2580	0.0170	0.657
9117	+46.901649	+0.988285	0.3096	0.0314	0.964
9218	+46.701477	-0.700521	0.2836	0.0382	0.032
9324	-16.176943	+0.806317	0.2650	0.0000	0.008
9334	-13.007022	+0.841651	0.3294	0.0281	0.739
9739	-36.306335	-0.878946	0.2037	0.0209	0.939
9895	+35.265858	+0.504277	0.3182	0.0327	0.308
10113	+54.181683	-0.140431	0.2997	0.0217	0.960
10559	-5.883640	-1.226615	0.2468	0.0270	0.680
11306	+56.738480	-0.518320	0.2582	0.0236	0.453
12879	+7.449054	-0.162061	0.3962	0.0255	0.043
12978	+7.167003	+0.147861	0.1657	0.0078	0.999
13015	+25.303169	+0.927766	0.2246	0.0077	0.008
13016	+25.588461	+0.979582	0.2445	0.0185	0.797
13064	-16.326523	-1.139602	0.2331	0.0177	0.970
13073	-23.974901	+0.142089	0.3285	0.0377	0.379
15386	-47.415257	-1.232566	0.2616	0.0165	0.889
13096	-1.629856	-1.202283	0.3625	0.0315	0.772
13098	-0.822849	-1.192286	0.2789	0.0154	0.408
13108	+9.870742	-1.200404	0.2642	0.0366	0.959
13144	+20.082094	-0.333601	0.2784	0.0138	0.101

Continued on Next Page...

Table 5.5 – Continued

SN Id	Ra	Decl	Redshift	Redshift Error	Fitprob
13168	+1.601530	+0.621411	0.3696	0.0273	0.675
13323	-36.948795	-0.134715	0.2458	0.0170	0.779
13329	-19.279881	-0.108535	0.3126	0.0259	0.966
13432	-41.546810	-1.075640	0.1646	0.0285	0.660
13441	-13.047049	-0.233050	0.2786	0.0276	0.498
13460	-14.285529	+0.141900	0.3008	0.0198	0.025
13474	+11.820527	-1.067936	0.3272	0.0134	0.074
13476	-3.983387	-0.790977	0.3072	0.0258	0.687
13477	+7.805247	-0.708372	0.4093	0.0242	0.527
13491	+43.285912	+0.118908	0.3772	0.0156	0.790
13495	+55.293995	+0.082106	0.3024	0.0247	0.015
13554	+7.156817	+0.871847	0.3274	0.0251	0.857
13615	-48.587643	+1.186595	0.2494	0.0224	0.964
13633	+4.665617	+0.005899	0.4149	0.0229	0.474
13646	-2.527527	-1.032138	0.2970	0.0149	0.565
13649	-4.471647	-0.618944	0.3177	0.0283	0.281
13675	-49.341034	-0.916605	0.2902	0.0209	0.552
13716	-45.045925	+0.488395	0.2363	0.0310	0.208
13729	-41.081322	+0.875180	0.3316	0.0333	0.688
13732	-35.731728	+0.901021	0.4121	0.0201	0.006
13737	-21.073776	+0.962635	0.3420	0.0273	0.802

Continued on Next Page...

Table 5.5 – Continued

SN Id	Ra	Decl	Redshift	Redshift Error	Fitprob
13740	-48.782986	-1.088698	0.2464	0.0204	0.494
13768	-36.924057	-0.763182	0.2464	0.0151	0.739
13813	-41.679146	-0.404855	0.2422	0.0138	0.308
13843	-40.839634	+0.207174	0.4294	0.0133	0.149
13859	+11.062123	+0.966985	0.3283	0.0195	0.901
13861	-22.152481	+0.075371	0.3739	0.0251	0.989
13867	-8.545136	+0.029390	0.3363	0.0317	0.833
13896	+2.712809	-0.069909	0.2073	0.0124	0.019
13908	+15.915957	+0.295023	0.2893	0.0080	0.013
13952	+4.634405	+0.788501	0.3444	0.0293	0.171
13958	+21.787783	+0.800367	0.2841	0.0072	0.004
13970	+21.264563	+1.199028	0.4020	0.0278	0.002
14074	-17.874083	-0.825294	0.3244	0.0271	0.747
14093	+26.539192	-1.056320	0.4118	0.0159	0.373
14113	+28.444508	-0.818503	0.1680	0.0156	0.037
14206	+17.394648	+0.704040	0.2224	0.0107	0.407
14231	+57.649651	+0.787543	0.1698	0.0138	0.924
14250	+12.822339	-0.605300	0.3945	0.0164	0.663
14268	+52.199345	+0.391068	0.2586	0.0123	0.803
14303	-49.385456	-0.535341	0.2784	0.0249	0.996
14304	-48.998257	-0.605920	0.3222	0.0228	0.896

Continued on Next Page...

Table 5.5 – Continued

SN Id	Ra	Decl	Redshift	Redshift Error	Fitprob
14322	-6.226969	-0.169474	0.3892	0.0326	0.229
14340	-14.173414	-0.855363	0.2911	0.0251	0.953
14342	+36.762356	-0.124528	0.3867	0.0246	0.086
14343	+0.707113	-0.954081	0.2776	0.0232	0.882
14347	+16.980722	-1.017121	0.2937	0.0198	0.660
14357	+47.646004	-0.938122	0.4231	0.0176	0.100
14402	+54.284733	+0.235943	0.2189	0.0533	0.076
14403	+16.838261	+0.651728	0.2930	0.0141	0.195
14404	+19.935963	+0.791945	0.3896	0.0197	0.936
14444	-23.298479	-0.815723	0.2468	0.0191	0.860
14453	-43.713764	+0.949342	0.3472	0.0291	0.654
14463	+3.145272	-0.350521	0.2091	0.0156	0.963
14467	+25.601969	-0.312970	0.3506	0.0219	0.706
14470	+44.214920	-0.351770	0.1791	0.0097	0.493
14491	+57.190311	+0.200347	0.2596	0.0240	0.007
14522	+28.528709	-0.725664	0.4071	0.0250	0.995
14524	+41.562748	-0.797870	0.2751	0.0254	0.419
14528	-10.064901	+0.479597	0.3483	0.0308	0.550
14531	+2.624236	+0.484530	0.3622	0.0237	0.018
14539	+28.243092	+0.505255	0.3855	0.0216	0.225
14540	+36.512310	+0.582063	0.2600	0.0099	0.959

Continued on Next Page...

Table 5.5 – Continued

SN Id	Ra	Decl	Redshift	Redshift Error	Fitprob
14548	+5.724540	+0.832766	0.3035	0.0196	0.875
14549	+8.181086	+0.963311	0.2395	0.0238	0.031
14561	+46.698784	+0.949422	0.1590	0.0182	0.598
14588	+47.689209	-0.776777	0.3789	0.0306	0.911
14617	+53.364662	+1.020237	0.2622	0.0147	0.992
14644	+24.080683	-0.069686	0.3844	0.0331	0.009
14708	+15.314544	-0.464897	0.3475	0.0352	0.936
14750	+34.518982	+0.652976	0.2187	0.0132	0.713
14760	+56.250420	+0.728214	0.3210	0.0222	0.397
14763	+33.566525	+1.121326	0.3425	0.0402	0.741
14786	-28.179609	-0.321451	0.3300	0.0285	0.391
14809	-28.624186	-0.655940	0.3159	0.0240	0.048
14823	+20.802895	-0.310595	0.3199	0.0267	0.863
14888	+25.704519	-0.649860	0.2863	0.0512	0.386
14900	+45.236168	-0.635597	0.4355	0.0103	0.388
14965	+18.935459	+1.037837	0.2590	0.0295	0.730
15055	+58.499172	-0.051699	0.1806	0.0156	0.950
15075	+51.886230	+0.346807	0.3720	0.0416	0.066
15103	-21.901405	-0.504698	0.3804	0.0308	0.728
15108	+24.434656	-0.541610	0.4120	0.0187	0.817
15137	-3.892738	-0.806592	0.2754	0.0190	0.882

Continued on Next Page...

Table 5.5 – Continued

SN Id	Ra	Decl	Redshift	Redshift Error	Fitprob
15291	-21.916155	-1.151761	0.3093	0.0341	0.705
15160	-1.571218	-0.579207	0.2214	0.0226	0.929
15198	+34.627426	-0.212283	0.2912	0.0084	0.062
15260	-20.822716	-0.275792	0.2299	0.0174	1.000
15263	-34.193546	+0.009994	0.3872	0.0303	0.456
15264	-33.449627	+0.015575	0.3134	0.0231	0.194
15268	-21.555054	+0.138679	0.2670	0.0188	0.041
15272	-9.226976	+0.084362	0.2174	0.0190	0.524
15289	-25.566935	-1.198645	0.3550	0.0286	0.979
15294	-41.524788	-0.731923	0.3473	0.0457	0.037
15345	-24.743235	+0.810492	0.2559	0.0215	0.417
15351	-33.464649	-0.053326	0.3382	0.0263	0.246
15357	-24.662676	+0.234191	0.2804	0.0146	0.912
15359	-12.543747	+0.310508	0.2334	0.0173	0.033
15363	+13.033107	+0.661303	0.3448	0.0358	0.116
15366	+9.382154	+1.156781	0.3062	0.0270	0.841
15401	-29.144682	+0.576335	0.3294	0.0286	0.735
15417	+15.557879	+0.461881	0.3054	0.0234	0.723
15419	+19.905230	+0.885640	0.2463	0.0240	0.969
15423	+36.508057	+0.626163	0.3281	0.0109	0.199
15436	+27.725121	+0.007171	0.3493	0.0491	0.209

Continued on Next Page...

Table 5.5 – Continued

SN Id	Ra	Decl	Redshift	Redshift Error	Fitprob
15448	+52.380318	-1.147368	0.2266	0.0151	0.930
15483	-40.208027	+0.696995	0.3297	0.0309	0.947
15489	+7.752604	-0.071033	0.2690	0.0616	0.014
15496	+8.073899	+0.274463	0.2381	0.0102	0.922
15511	+44.930248	-0.955192	0.2571	0.0257	0.996
15522	+39.955208	+0.795600	0.3244	0.0166	0.908
15525	+51.527611	+1.130735	0.3462	0.0442	0.739
15553	-38.879871	+0.944185	0.2893	0.0310	0.908
15569	-0.622365	+0.869958	0.3457	0.0335	0.663
15592	-39.532703	-1.178497	0.3600	0.0214	0.236
15777	-33.811485	-0.618331	0.2958	0.0139	0.194
15710	+55.052727	+0.721995	0.2076	0.0303	0.574
15719	+37.647919	+1.103298	0.2800	0.0161	0.045
15726	-10.505381	-0.007296	0.3980	0.0164	0.249
15745	+42.207901	-0.107615	0.4240	0.0209	0.164
15751	+54.028172	-0.051756	0.3234	0.0347	0.512
15782	-7.323786	-0.428027	0.3126	0.0347	0.100
15802	+29.753187	-1.079412	0.3572	0.0276	0.998
15812	+19.359903	-0.309012	0.3246	0.0275	0.972
15814	+29.725130	-0.372724	0.3548	0.0178	0.549
15816	+19.454563	+0.098759	0.2545	0.0389	0.225

Continued on Next Page...

Table 5.5 – Continued

SN Id	Ra	Decl	Redshift	Redshift Error	Fitprob
15817	+29.564510	+0.013274	0.3905	0.0181	0.618
15829	-36.914501	-0.762292	0.3252	0.0214	0.956
15850	+0.667499	-1.165219	0.2353	0.0207	0.501
15860	+4.597352	+0.183035	0.2906	0.0159	0.917
15870	+30.016201	-0.234981	0.3944	0.0262	0.891
15874	+39.769428	-0.387094	0.4283	0.0176	0.344
15903	+48.906143	-0.602657	0.3190	0.0542	0.054
15951	+8.998732	+1.040345	0.2724	0.0320	0.655
15992	+8.885862	+0.025403	0.4104	0.0226	0.951
15994	+11.932373	+0.100354	0.2223	0.0483	0.127
16052	+58.600201	-0.720806	0.1417	0.0094	0.964
16111	-30.683083	+0.935445	0.2275	0.0172	0.954
16120	+47.706512	-0.236595	0.3850	0.0431	0.208
16121	+49.228779	-0.356068	0.3494	0.0369	0.580
16130	+51.774826	+0.157737	0.3294	0.0203	0.039
16148	+48.661152	+0.588160	0.3056	0.0187	0.898
16152	+46.908451	+0.987692	0.2515	0.0194	0.722
16199	-27.055756	+1.134934	0.2293	0.0228	0.338
16220	+9.925722	+0.680094	0.3240	0.0240	0.470
16225	+36.512043	+0.261177	0.3915	0.0218	0.234
16238	+27.915127	-0.435866	0.3405	0.0413	0.480

Continued on Next Page...

Table 5.5 – Continued

SN Id	Ra	Decl	Redshift	Redshift Error	Fitprob
16302	-28.232782	+0.183434	0.1981	0.0120	1.000
16452	-37.442986	-0.281572	0.1609	0.0155	0.099
16460	+11.009616	-0.230026	0.2828	0.0153	0.593
16642	+29.146982	-0.288654	0.1555	0.0178	0.006
16768	-37.299435	+0.692840	0.1420	0.0134	0.023

CHAPTER 6

THE CLUSTER SN RATE

6.1 Introduction and Review of Previous Measurements

The type Ia SN rate in galaxy clusters is an important field of study for a number of reasons. As discussed in §1, SN rate measurements are an observational probe of the progenitor systems, with the connection to progenitor models being made through inference of the distribution of delay times (DDTs) with respect to star formation. As galaxies in clusters are generally composed of early-type galaxies with old stellar populations, measurements of the SN Ia rate in clusters can in principle simplify the inference of the SN DDT. SNe in galaxy clusters are also a candidate source for metal enrichment of the intra-cluster medium (ICM). In particular, improved measurement of the rate of intra-cluster SNe would be significant for constraining the relative importance of sources that may contribute to the cluster ICM enrichment (e. g. intra-cluster stars vs. galaxy outflow).

The existing measurements of the cluster SN rate are few, and are generally based on low-number statistics. Estimates of the SN cluster rate were first presented by Crane et al. (1977) and Barbon (1978), who considered ≈ 5 SNe discovered in the Coma cluster. The cluster SN rate was measured by Gal-Yam et al. (2003) in clusters at $z \approx 0.25$ and $z \approx 0.9$. The Gal-Yam et al. (2003) results are based on a search for SNe in archival images of the Hubble Space Telescope (HST) and utilize 1 and 2 SNe, respectively. Subsequent to the HST SN search, a dedicated search for SNe in 161 Abell clusters was undertaken by The Wise Observatory Optical Transient Search (WOOTS) (Gal-Yam et al., 2008). A total of 6 SNe Ia discovered by the WOOTS were used to determine the cluster SN Ia rate at $z \approx 0.15$ by Sharon et al. (2007b).

A sample of 2-3 SNe Ia from the Supernova Legacy Survey (SNLS) have been used to determine the cluster SN Ia rate at $z \approx 0.45$ by Graham et al. (2008). Finally, the sample of SNe in the local ($z \lesssim 0.04$) universe presented by Cappellaro et al. (1999) have been reanalyzed by Mannucci et al. (2008) to determine the cluster SN Ia rate with a sample of 12.5 SN Ia (a fractional SN reflects uncertainty in typing; see Cappellaro et al. (1999)). Additionally, Mannucci et al. (2008) have placed the first constraints on the core-collapse (CC) SN rate in galaxy clusters based on a sample of 7.5 CC SNe. A summary of the SN Ia rate results from the above cluster SN studies is given in Table 6.1.

A SN search in 15 massive, high-redshift ($0.5 < z < 0.9$), X-ray selected clusters has been carried out on the HST, as described in Sharon et al. (2007a), and a measurement of the SN Ia rate based on 6-14 SNe discovered by the program is forthcoming (Sharon et al., 2008). A dedicated SN search, targeting ≈ 60 X-ray selected clusters in the redshift range $0.1 < z < 0.2$, is also being carried out on the Bok 2. 3m telescope on Kitt Peak (Sand et al., 2008)

As can be seen in Table 6.1, the knowledge of the cluster SN Ia rate comprises 5 measurements, based on a total of $\approx$ 25 SNe. In this Chapter, I describe new measurements of the cluster SN Ia rate based on data from the SDSS-II Supernova Survey. The measurements are based on 16 (19) SNe from the first 2 (3) seasons of the SN Survey, in the redshift range $0.03 < z < 0.30$, and therefore represent a significant statistical contribution to cluster SN Ia studies. In §6.2 I describe the galaxy cluster catalogs employed in this SN rate analysis. In §6.3 I describe selection of the cluster SN sample from the SDSS-II Supernova Survey data. In §6.4 I describe determination of the efficiency for SN selection. In §6.5 I present results on the cluster SN Ia rate, as well as limits on the cluster CC SN rate, and studies of the distribution of SNe with respect to their host galaxies. I summarize in §6.6.

Table 6.1. Cluster Rate Measurements

Reference	Redshift Range	N_{SNe}	SN Ia Rate [SNuB h^2]
This work (c4)	0.03 - 0.17	5	$0.37^{+0.25}_{-0.16}$
This work (maxBCG)	0.10 - 0.30	12	$0.45^{+0.17}_{-0.13}$
Mannucci et al. (2008)	0 - 0.04	12.5	$0.57^{+0.22}_{-0.16}$
Sharon et al. (2007b)	0.06 - 0.19	6	$0.73^{+0.45}_{-0.29}$
Gal-Yam et al. (2003)	≈ 0.025	1	$0.80^{+1.84}_{-0.65}$
Graham et al. (2008)	≈ 0.45	3	$0.63^{+1.04}_{-0.33}$
Gal-Yam et al. (2003)	≈ 0.9	2	$1.63^{+2.16}_{-1.06}$

6.2 Galaxy Cluster Catalogs

In studying the type Ia SN rate in galaxy clusters we will work with two primary cluster catalogs; the c4 cluster catalog and the maxBCG cluster catalog. The c4 cluster finding algorithm and catalog are discussed in detail by Miller et al. (2005). The maxBCG catalog is presented by Koester et al. (2007a), and the cluster finding algorithm is described by Koester et al. (2007b). We briefly describe and summarize the content of these 2 cluster catalogs below. The redshift distribution for the clusters in these 2 catalogs is shown in Figure 6.1.

6.2.1 c4 Cluster Catalog Description

The c4 cluster catalog is based on the main spectroscopic sample of the SDSS and contains clusters in the redshift range $0.03 < z < 0.17$. The main spectroscopic sample of galaxies from SDSS is designed to be complete to a limiting magnitude of

$r \approx 17.8$ (Strauss et al., 2002). For typical cluster galaxy luminosities, this implies that the identification of member galaxies is complete for clusters at $z < 0.11$. For clusters above this redshift limit a correction has to be made to the total cluster luminosity. The c4 cluster identification algorithm works by searching for groups of objects that are tightly clustered in a 7-dimensional feature space, that includes spatial position, redshift, and observed colors. Note that there is no requirement that the colors for the galaxies be consistent with the colors of early-type galaxies, only that they be consistent with one another. The SDSS main galaxy sample can not be 100% complete, as the SDSS fiber-spectrograph imposes a minimum angular separation for objects targeted for the SDSS main spectroscopic galaxy sample. A correction is applied to the c4 cluster luminosities to account for this by including galaxies as members of the cluster when they satisfy the magnitude requirement ($r < 17.8$) and have similar colors to the spectroscopically determined cluster members. The published c4 catalog is based on the 2nd data release of the SDSS (Abazajian et al., 2004) and contains 748 total clusters. The catalog used in this work is an extended version of the c4 catalog that contains 1713 total clusters and is based on the 5th data release of the SDSS (Adelman-McCarthy et al., 2007). The subset of clusters that we will use in measuring the cluster SN rate are those that lie within stripe 82, and that have $-40^\circ < \alpha_{\mathrm{J2000}} < 50^\circ$. There are 71 c4 clusters in this subset.

6.2.2 maxBCG Cluster Catalog Description

The maxBCG catalog is based on SDSS photometric measurements, and the cluster identification algorithm relies on the tight relationship between color and redshift for luminous red galaxies, which make up the majority of galaxy cluster composition. The maxBCG algorithm assigns a photometric redshift to each identified cluster that

is derived by comparing the cluster member galaxy colors to the expected colors for early-type galaxies, as a function of redshift. Comparison of the photometric redshifts for the maxBCG clusters to the spectroscopically measured redshift of the brightest cluster galaxy (BCG), when available, shows that the residuals for redshift (photometric - spectroscopic) are well described by a Gaussian distribution with a mean of 0 and a width of $\sigma \approx 0.015$. The observed $(g-r)$ and $(r-i)$ colors for maxBCG member galaxies, as a function of redshift, are shown in Figure 6.2. Linear functions were fit to to the $(r-i)$ and $(g-r)$ colors as a function of redshift, z, and these will be used below for applying k-corrections to the observations. For reference, the functions derived are,

$$(r-i)(z) = 0.338 + 0.577\ z \tag{6.1}$$

$$(g-r)(z) = 0.622 + 3.766\ z. \tag{6.2}$$

The maxBCG catalog is restricted to the redshift interval $0.1 < z < 0.3$, and is thus highly complementary to the c4 catalog. The lower-limit for the maxBCG cluster catalog is imposed because the colors for early-type galaxies show a much greater scatter at $z < 0.1$. The upper limit is imposed because, at $z \approx 0.3$, the "4000 $\mathring{A}$ break" that is responsible for the uniformity in early-type galaxy colors moves into the region between the SDSS observer frame g and r band filters. Thus, the accuracy and precision for galaxy photometric redshifts is severely diminished. A lower-limit for the luminosity of cluster members is imposed so that the definition of the composition of the clusters is consistent across the redshift range. The limit corresponds to an absolute magnitude of ${}^{(0.25)}i \approx -20.25$, (the ${}^{(0.25)}i$ notation is explained in §6.2.3) and is such that the catalog is volume limited over the entire redshift range $0.1 < z < 0.3$. The public maxBCG cluster catalog contains 13,823 clusters with $N_{200} \geq 10$.

The subset of maxBCG clusters that we will use in measuring the cluster SN rate are those that lie within stripe 82, and that have $-50^\circ < \alpha_{\rm J2000} < 60^\circ$. There are 471 maxBCG clusters in this subset. Additionally, this work makes use of a catalog of the maxBCG member galaxies.

In addition to the cluster richness and luminosity estimates that are provided with the maxBCG catalog, the maxBCG clusters have been extensively studied by e.g. Sheldon et al. (2007b); Johnston et al. (2007); Sheldon et al. (2007a). Of particular relevance to the study of the SN rate in galaxy clusters are the luminosity functions (LFs) of maxBCG clusters presented by Hansen et al. (2007), and we will make extensive use of these below.

6.2.3 Luminosity Content of c4 and maxBCG Cluster Catalogs

In §6.5 we will present the SN rate in galaxy clusters per unit luminosity. In this section we present a comprehensive discussion of the luminosity content for the c4 and maxBCG cluster catalogs. In what follows we denote a filter, f, that has been k-corrected to a redshift z as ${}^{(z)}f$. All luminosities presented here are for galaxies with $L > 0.4\ L_*$ (L_* is a characteristic luminosity for cluster members; see Equation 6.3). Correcting for the faint end of the luminosity distribution is discussed below.

The c4 catalog provides total cluster luminosities in SDSS r-band. The total *uncorrected* r-band luminosity for the galaxies identified as cluster members, for clusters considered in this study, is $2.02 \times 10^{13}\ L_\odot\ h^{-2}$, where $L_\odot$ is the luminosity of the sun, and h is the value of the Hubble constant in units of 100 km s^{-1} Mpc^{-1}. As discussed in §6.2.1, these luminosities have to be corrected to account for incompleteness of the spectroscopic sample due to fiber-collisions. The total r-band luminosity *after* making this correction is also provided by the c4 catalog and has the value

$4.08 \times 10^{13}\ L_{\odot}\ h^{-2}$. As mentioned above, the luminosities for clusters at redshift $z > 0.11$ also have to be corrected to account for the fact that some cluster galaxies will have observed magnitudes fainter than the completeness limit of the main SDSS galaxy sample ($r \approx 17.8$). Of the 71 c4 clusters we are considering, 12 are at $z > 0.11$. Applying a correction to the luminosities of these 12 cluster results in a total r-band luminosity for c4 clusters in this study of $4.12 \times 10^{13}\ L_{\odot}\ h^{-2}$.

The maxBCG catalog includes the summed luminosities for member galaxies in ${}^{(0.25)}i$ and ${}^{(0.25)}r$. For reference these are given in Table 6.2, for several values of limiting projected distance. However, the maxBCG cluster LFs presented by Hansen et al. (2007) represent a more complete study of the luminosity content of maxBCG clusters, and we will use these as the definitive measure of the total maxBCG cluster luminosities. In particular, a background subtraction has been performed that reduces inaccuracies in the cluster luminosities due to interloping foreground and background galaxies that may be counted as maxBCG cluster members. In Hansen et al. (2007), luminosity functions are presented for maxBCG satellites, as a function of the richness measure, N_{200}. The LFs account for both red and blue cluster galaxies, but do not include the contribution to the luminosity from the BCG. The LFs are assumed to take the form of a Schechter function,

$$\phi(L)\ dL = \phi^{*}\ \left(\frac{L}{L_{*}}\right)^{\alpha}\ e^{-L/L_{*}}\ \frac{dL}{L_{*}} \tag{6.3}$$

where L_{*} is a characteristic luminosity for cluster members, and ϕ^{*} is a normalization constant with units of inverse volume. The 3 parameters of the LFs, ϕ^{*}, L_{*}, α, are each expressed as functions of N_{200}, with the general functional form of $A\ N_{200}^{\beta}$. The values of A (normalization) and β (exponent) for these 3 LF parameters are given in

Table 6.2. maxBCG Cluster Catalog Luminosity Estimates

Filter	Luminosity[a] ($d < \infty$)	Luminosity ($d < 1$ Mpc h^{-1})	Luminosity ($d < 0.5$ Mpc h^{-1})	Luminosity (BCGs)
${}^{0.25}i$	1.19	1.13	0.591	0.367
${}^{0.25}r$	0.97	0.92	0.481	0.258

[a]Luminosities are given in units of $10^{14}\ L_\odot\ h^{-2}$.

Table 6.3. To use the LFs to compute the total luminosity we exploit the identity

$$\Sigma\ L = \langle L(N_{200})\rangle\ N_{200} \tag{6.4}$$

where ΣL denotes the summed luminosity for the cluster, and the average luminosity, $\langle L\rangle$, is given by,

$$\langle L(N_{200})\rangle = \frac{\int_{0.4L_*}^{\infty} dL\ L\ \phi(L)}{\int_{0.4L_*}^{\infty} dL\ \phi(L)}. \tag{6.5}$$

Equation 6.4 gives the total ${}^{(0.25)}i$ luminosity in a cluster, as a function of N_{200}. The total luminosity in clusters in the SN survey region is then the sum over N_{200} of $\langle L(N_{200})\rangle\ N_{SN}(N_{200})$, where $N_{SN}(N_{200})$ is the number of clusters in the survey region for which the number of member galaxies is N_{200}. Using this formalism we find the total luminosity in the survey region is $\Sigma L_i^{0.25} = 1.096 \times 10^{14}\ L_\odot\ h^{-2}$.

Correcting Cluster Luminosities for Faint Galaxies

The luminosities quoted above for the c4 and maxBCG cluster catalogs include only galaxies with $L > 0.4\ L_*$, which is a conventional way of characterizing cluster lumi-

Table 6.3. maxBCG Luminosity Function Parameters

LF Parameter	Normalization	Exponent
ϕ^*	8.0 Mpc^{-3} h^3	-0.20
L_*	0.8×10^{10} $L_\odot$ h^{-2}	0.15
α	-0.28	0.25

nosities. In measuring the cluster SN rate we do not wish to exclude SNe occurring in faint galaxies, and so it is necessary to estimate the contribution to the total cluster luminosities from galaxies with $L < 0.4\ L_*$. The total cluster luminosity can be estimated as $L = k\ L^+$, where L^+ denotes the luminosity for galaxies with $L > 0.4\ L_*$ and the correction factor, k, is given by

$$k = \frac{\int_0^\infty dL\ L\ \phi(L)}{\int_{0.4L_*}^\infty dL\ L\ \phi(L)}. \tag{6.6}$$

For a typical maxBCG cluster with $N_{200} = 20$ the power-law exponent of the luminosity function is $\alpha = -0.59$ (Table 6.3). For a cluster with $N_{200} = 35$ the value for the exponent is $\alpha = -0.68$. The corresponding correction factors are $k = 1.21$ and $k = 1.25$. We will assume that the faint end of the luminosity function is a characteristic property of galaxy clusters and that the power-law behavior of the LFs for maxBCG clusters is appropriate for the c4 clusters also.

k-corrections

It is well known that the wavelength of light emitted from distant objects is shifted to longer wavelengths when propagating through an expanding space-time. For broad-band photometric observations this means that the portion of the spectral energy

distribution (SED) of an astronomical object that is probed by a fixed earth-frame filter is not necessarily equal to the wavelength range of the earth-frame filter, but depends on the redshift of the object. The procedure for transforming observations made in one filter to what would be observed in a different filter is known as a "k-correction" (see e.g. Hogg et al. (2002)). To minimize uncertainties due to k-corrections, the maxBCG luminosities are given in filters that have been k-corrected to the median redshift of the clusters, $z = 0.25$. For comparison of the SN rate results based on the maxBCG clusters with previous cluster SN rate measurements, it will be necessary to k-correct the luminosities into more standard filters.

In order to determine the appropriate k-corrections I chose a set of galaxies from the SDSS galaxy catalog that satisfy the color vs. redshift relations for maxBCG members discussed above. The corresponding set of galaxies contains $\approx 675,000$ members. I then cross correlated these galaxies with their corresponding records in the `photoz` database provided by the SDSS CAS, and based on the work of Blanton et al. (2003a). I thereby determine an average k-correction as a function of redshift, appropriate to the early-type galaxies that make up the bulk of the maxBCG catalog. The k-corrections so derived, in SDSS r and i bands, are shown in Figure 6.3. For reference, the functions employed for k-corrections as a function of redshift, z, are

$$K_r(z) = 9.17 \times 10^{-2} + 1.48\ z \tag{6.7}$$

$$K_i(z) = 3.95 \times 10^{-3} + 1.01\ z \tag{6.8}$$

To transform the maxBCG cluster luminosities from ${}^{(0.25)}i$ to r, I note the following identity:

$$m_r = m_r^{0.25} - K_r(z = 0.25) \tag{6.9}$$

$$= \quad m_i^{0.25} + (r-i)(z=0.25) - K_r(z=0.25) \tag{6.10}$$

Using the expressions given above for $(r-i)(z)$ and $K_r(z)$, evaluated at $z = 0.25$, we derive the transformation $m_r = {}^{(0.25)}m_i + 0.02$. For comparison to other cluster SN rate measurements, it is necessary to express the cluster luminosities in units of $L^r_\odot$. The conversion to solar luminosities is given by

$$\left(\frac{L}{L_\odot}\right)_r = \left(\frac{L}{L_\odot}\right)_{0.25_i} \times 10^{-0.4((m_r - m_{0.25_i}) - (M^r_\odot - M_\odot^{0.25_i}))}, \tag{6.11}$$

where $M_\odot$ is the absolute magnitude of the sun. To compute the absolute magnitude of the sun in an arbitrary filter, I use a solar spectrum obtained from the CALSPEC[1] database, hosted by the Space Telescope Science Institute, and compute synthetic magnitudes using a custom piece of software written for this task. I thereby derive values for the absolute magnitude of the sun of $M^r_\odot = 4.64$ (in agreement with the value published by Blanton & Roweis (2007)), and $M_\odot^{0.25i} = 4.67$. With these values, Equation 6.11 becomes $(L/L_\odot)_r = 0.957\ (L/L_\odot)_{0.25_i}$, giving the r-band luminosity in maxBCG clusters, for galaxies with $L > 0.4\ L_*$, as $\Sigma L_r = 1.049 \times\ 10^{14}\ L_\odot$.

6.3 The Cluster SN Sample

To define the SN sample that is associated with galaxy clusters it is necessary to define selection criteria on both the SN light-curve properties, and the SN spatial correlation with clusters. As mentioned in §2.5, the analysis of SN light-curves is based on the final photometric reductions. SMP light-curves have been generated for

1. All confirmed SNe (type Ia, type Ib/c, type II) for the 2005-2007 SN observing seasons

1. http://www.stsci.edu/hst/observatory/cdbs/calspec.html

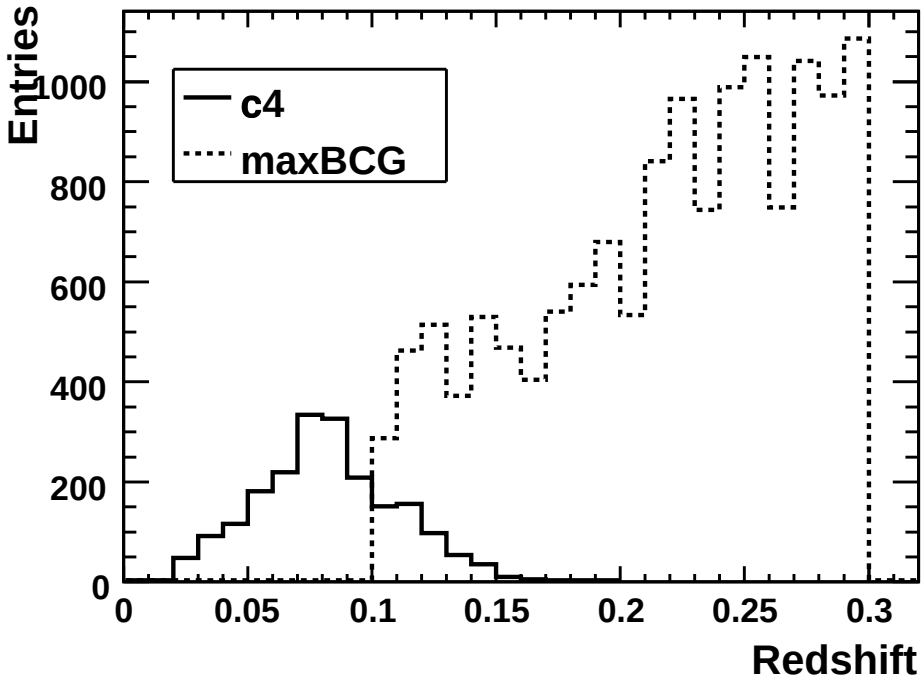

Figure 6.1: Redshift distributions for the c4 ($z < 0.17$) and maxBCG ($0.1 < z < 0.3$) cluster catalogs.

2. 500 "best" photometric SN candidates from the 2005 observing season

3. 500 randomly chosen photometric SN candidates from the 2005 observing season

4. $\approx$ 600 SN candidates from each of the 2005 and 2006 observing seasons that were chosen by objective selection criteria on the color-typing fits

As in §5, the SN rate will be based on SN candidates from category (4). However, we have also considered cluster SN candidates from categories (1), (2), and (3). At the low-redshifts covered by the c4 cluster catalog, confirmed SNe from the 2007 season can be used to place constraints on the type Ia SN rate, and CC SNe from all seasons can be used to place a lower limit on the CC SN rate in galaxy clusters. Additionally, the results of §6.5.4 do not require precise knowledge of the SN selection function.

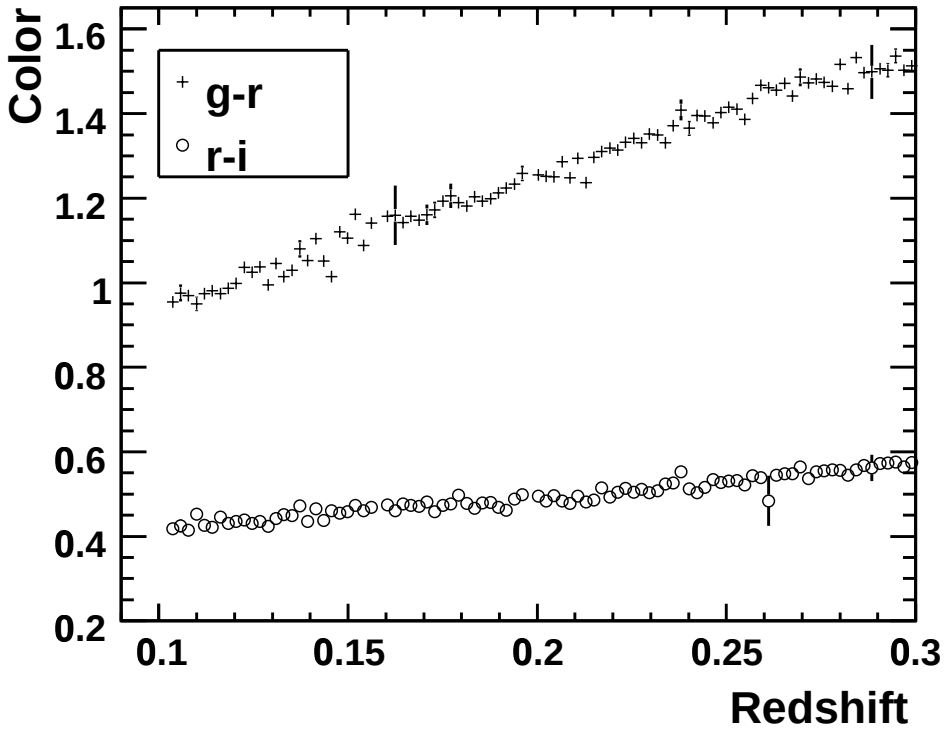

Figure 6.2: Observed colors of maxBCG galaxies vs. redshift.

As discussed in §4 the SNe in the rate sample are required to meet certain requirements on their light-curve fits.

- At least 1 observation at < -2 days relative to maximum light
- At least 1 observation at $> t_{late}$ days relative to maximum light.

  For maxBCG cluster SN candidates $t_{late} = 10$ days.

  For c4 cluster SN candidates $t_{late} = 5$ days.
- Fit probability $> 10^{-10}$.

A SN candidate is defined to be associated with a galaxy cluster if it satisfies

- Within 1 Mpc h^{-1} projected distance of the center of a cluster

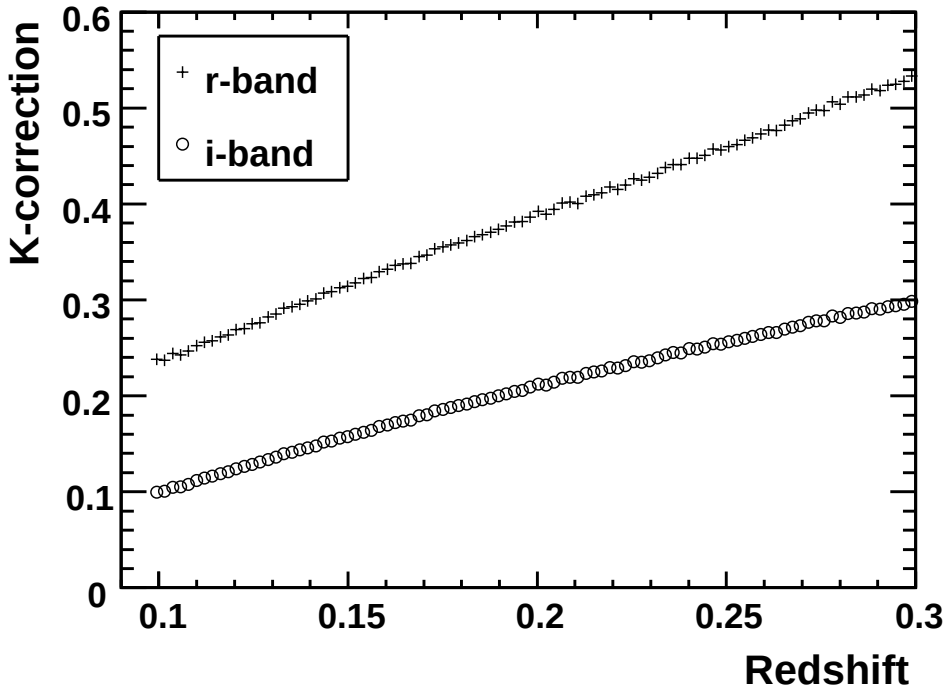

Figure 6.3: K-corrections vs. redshift for early-type galaxies.

- SN redshift is consistent with the cluster redshift.

The definition of redshift consistency depends on whether the SN and/or cluster redshifts are determined photometrically or spectroscopically. For the c4 clusters, the cluster redshifts are always precisely determined with a spectroscopic measurement, whereas the maxBCG cluster redshifts are determined photometrically. Consistency between the SN redshift, z_s, and cluster redshift, z_c, is defined in the following way:

- Spectroscopic SN redshift and spectroscopic cluster redshift

  $|z_s - z_c| < 0.015$

- Spectroscopic SN redshift and photometric cluster redshift

  $|z_s - z_c| < 0.025$

- Photometric SN redshift and spectroscopic cluster redshift

  $|z_s - z_c| < 2.5\ \sqrt{(0.01)^2 + \delta z_s^2}$

- Photometric SN redshift and photometric cluster redshift

  $|z_s - z_c| < 2.5\ \sqrt{(0.015)^2 + \delta z_s^2}$

where δz_s is the error on the SN photometric SN. The SNe that satisfy the selection criteria are listed in Table 6.4 (c4 clusters) and Table 6.5 (maxBCG clusters). We note that SN 16280 is associated with 2 distinct clusters, and that SNe 14279 and 16215 are associated with the same cluster.

6.3.1 Core-Collapse SNe

As discussed above, the type Ia SN rate in galaxy clusters is particularly important as galaxies in clusters are generally composed of old stellar populations, which simplifies the interpretation of the SN rate in terms of a DDT. As core-collapse SNe are known to be produced by young, massive stars, the CC SN rate in galaxy clusters is an interesting complementary probe of the recent star formation activity in galaxy clusters. In the SDSS-II Supernova Survey SN sample, there are 3 confirmed CC SNe in galaxy clusters. These are listed in Table 6.6. SN 18297 is relatively far away from a low-richness cluster and could reasonably be considered to be in the field. However, SNe 13195 and 20838 are solidly associated with c4 clusters.

6.4 Survey Efficiency

The method for determining the SN discovery efficiency is based on the same MC studies discussed in §5. However there is an important modification to be considered for SNe in galaxy clusters. It is a well established result that type Ia SNe in early-

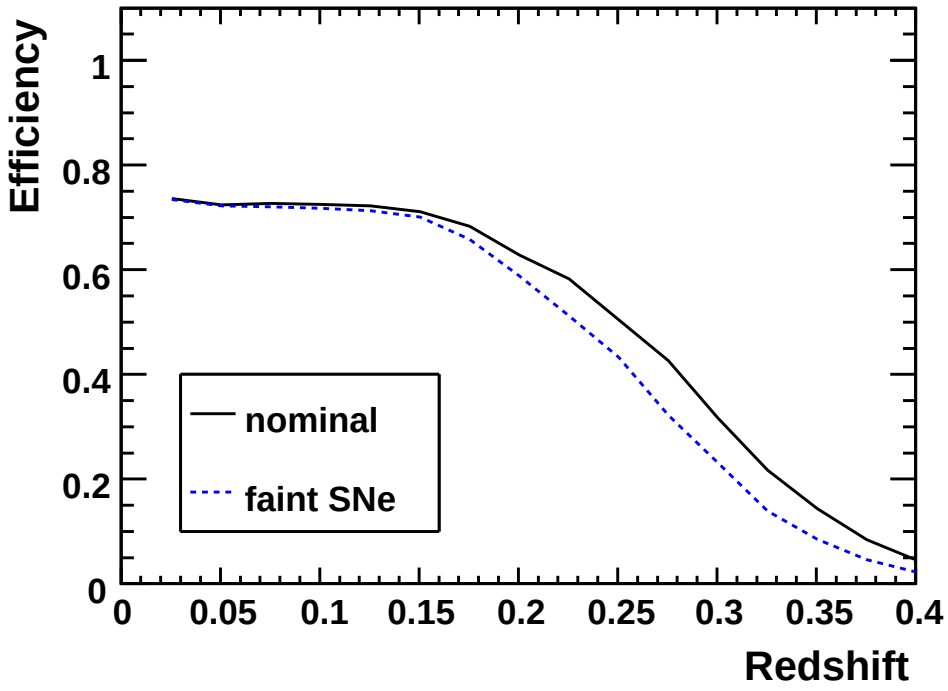

Figure 6.4: Efficiencies for the nominal (black/solid) and faint (blue/dashed) SN distributions.

type galaxies are more likely to be intrinsically faint, fast-declining SNe (Sullivan et al., 2006b; Smith et al., 2008). Therefore, the assumed distribution for MLCS Δ for the entire SN sample is not appropriate for considering SNe in galaxy clusters. To determine the SN discovery efficiency for SNe in galaxy clusters, we generated a set of MC SNe with a Δ distribution similar to the observed distribution for cluster SNe. The results, compared to the efficiency for a MC sample with a nominal Δ distribution are shown in Figure 6.4.

6.5 SDSS SN Results

6.5.1 c4 cluster rate

As discussed above, there are 5 type-Ia SNe from the first 2 seasons in c4 clusters that satisfy the SN selection criteria. The total r-band luminosity in the SN survey region, after correcting for the faint end of the LF, is 4.99×10^{13} $L^r_\odot$. The total observing time for the first 2 seasons of the SDSS-II Supernova Survey is 0.49 years. The efficiency is approximately constant, with the value $\epsilon \approx 74\%$. Using these values, the SN rate in c4 clusters, considering only the first 2 years, is

$$r = \frac{N(1+\langle z \rangle)}{\Sigma L_r \; \epsilon \; T} = 0.30^{+0.20}_{-0.13} \; \mathrm{SNu}r \; h^2 \tag{6.12}$$

with SNur $= (10^{10} \; L^r_\odot)^{-1}(100 \; \mathrm{yr})^{-1}$. Jorgensen (1997) (clusters) and Padmanabhan et al. (2004) (field) give the average mass to luminosity ratio (r-band) for early-type galaxies as ≈ 3, which is in good agreement with the M/L conversion employed by Sharon et al. (2007b). Using this assumption, the type-Ia SN rate per unit luminosity quoted above is equal to $0.10^{+0.068}_{-0.043}$ SNuM h^2, with SNuM $= (10^{10} \; M_\odot)^{-1}(100 \; \mathrm{yr})^{-1}$. Using the same average conversion factor from r to B as Sharon et al. (2007b), this corresponds to $0.37^{+0.25}_{-0.16}$ SNuB h^2.

Although the full analysis of the light-curves for photometric SN candidates from the 3rd year of the SDSS-II Supernova Survey has not yet been performed, it has been shown in §4 that the confirmed type-Ia SN sample from the SDSS-II Supernova Survey is essentially complete to the redshift limit that contains the majority of luminosity of the c4 catalog, $z \approx 0.13$. Therefore, we can plausibly claim that the sample of SNe from the 3rd year data set is complete. Under this assumption, the

value for the cluster SN rate, based on 8 SNe is,

$$r = \frac{N(1+\langle z \rangle)}{\Sigma L_r \ \epsilon \ T} = 0.33^{+0.18}_{-0.13} \ \mathrm{SNu}r \ h^2, \tag{6.13}$$

where ϵ averaged over the first 3 SN observing seasons is 0.72, and the total earth-frame observing time is 0.74 years. Even if we allow for the possibility that we have missed 1 low-redshift cluster SN from the 3rd year sample, the Poisson error on 8 events is still the dominant contribution to the error; if we allow that we missed 2 cluster SNe, than the relative error becomes comparable to the Poisson error on the 5 events from the first 2 year SN sample, although the tighter constraint on the lower limit is still robust.

6.5.2 maxBCG cluster rate

As discussed in §6.3, there are 12 SNe in maxBCG clusters from the first 2 SDSS-II Supernova Survey observing seasons that satisfy the selection criteria. As the SDSS-II Supernova Survey SN discovery efficiency is not well approximated as constant over the redshift range of the maxBCG catalog, in determining the SN rate in maxBCG clusters we use the more formal definition of the SN rate per unit luminosity, r_L,

$$r_L = \frac{N}{\widetilde{\epsilon T \Sigma L}} \tag{6.14}$$

with

$$\widetilde{\epsilon T \Sigma L} = T_\oplus \int_{z_{\min}}^{z_{\max}} dz \ \frac{\Sigma L(z) \ \epsilon(z)}{1+z}, \tag{6.15}$$

where $T_\oplus$ is the earth frame observation time, $\Sigma L(z)$ is the total cluster luminosity as a function of redshift, and $\epsilon(z)$ is the SN discovery efficiency. For the maxBCG

catalog $z_{\rm min}$ is fixed to 0.1. In Figure 6.5 we show the value of the maxBCG cluster SN rate as a function of $z_{\rm max}$. This figure shows that the derived SN rate is not sensitive to the exact upper limit on the cluster sample chosen. If the upper limit is chosen as the upper limit of the maxBCG catalog, $z = 0.3$, then we have $N = 12$, $\widetilde{\epsilon T \Sigma L} = 3.33 \times 10^{13}$ yr $L^r_\odot$, including the correction for the faint end of the LF. The derived value of the SN rate is thus $r_L = 0.36^{+0.14}_{-0.10}$ SNur h^2. Figure 6.6 shows the cluster SN rate as a function of the limit on the projected distance from the center of the cluster, in units of Mpc h^{-1}. The fraction of red, early-type galaxies in clusters is larger at small separations from the cluster center, and in this sense the SN rate at smaller separations is a more reliable probe of the component of the SN rate that originates from an old stellar population. Furthermore, the extent of a cluster is not an unambiguously defined quantity, and SNe at smaller separations are more robustly associated with the cluster. Figure 6.6 shows that the derived SN rate is not strongly dependent on the limiting projected radius that we use to define cluster membership, for limits greater than $\approx$ 0.4 Mpc h^{-1}. While the rate appears to be smaller for projected distances $<$ 0.4 Mpc h^{-1}, with the small number of SN events, it is not a statistically significant result. Figure 6.7 shows the SN rate as a function of the lower limit on the cluster richness measure, N_{200}. The SDSS-II Supernova Survey cluster rate results, along with the previous measurements listed in Table 6.1, in units of SNuB h^2, are shown in Figure 6.10. A fit of the data to a linear model of the cluster SN Ia rate as a function of redshift, $r = A + Bz$, gives best fit values of $A = 0.48 \pm 0.14$ SNuB h^2 and $B = 0.40^{+0.82}_{-0.70}$.

In §4, the SN rate in low-redshift early-type galaxies was estimated as $\approx 0.17^{+0.06}_{-0.04}$ SNur h^2. The SN Ia rate in early-type galaxies is given by Cappellaro et al. (1999) as (converting from SNuB to SNur) 0.25 ± 0.09 SNur. The c4 and maxBCG cluster rates are seen to be larger by a factor of $\approx$ 1.5 compared to the global SN rate for

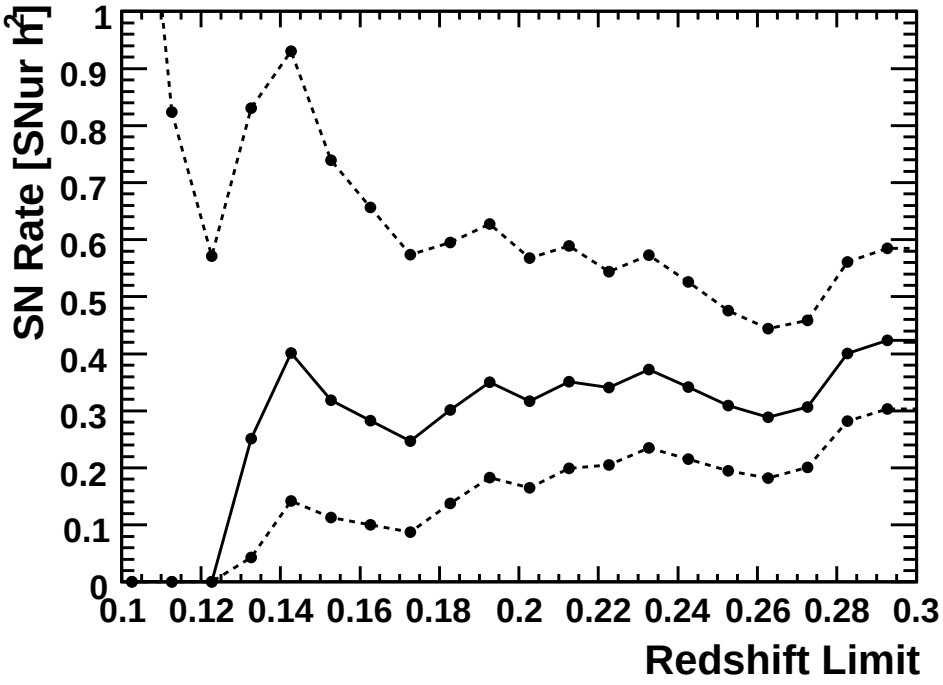

Figure 6.5: maxBCG cluster SN rate as a function of upper limit on the redshift range. The dashed lines represent the 1-sigma upper and lower limit of the SN rate.

early-type galaxies, which is in good agreement with the enhancement of the type-Ia SN rate reported by Mannucci et al. (2008).

6.5.3 Limit on the CC SN cluster rate

As mentioned in §6.3 there are at least 1 spectroscopically confirmed type II SN and 1 spectroscopically confirmed type Ib/c SN in low-redshift c4 clusters. While the efficiency of the SDSS-II Supernova Survey for discovering non-Ia SNe is not well constrained, we can unambiguously state that it is $< 100\%$. Therefore, the detection of 1 type II SN and 1 Ib/c SN can be used to place lower limits on the cluster CC SN rate if we assume that the discovery efficiency is 100%. Making this assumption gives a lower limit of $0.044^{+0.101}_{-0.037}$ SNur h^2 or $0.055^{+0.122}_{-0.045}$ SNuB h^2 for the rate of both

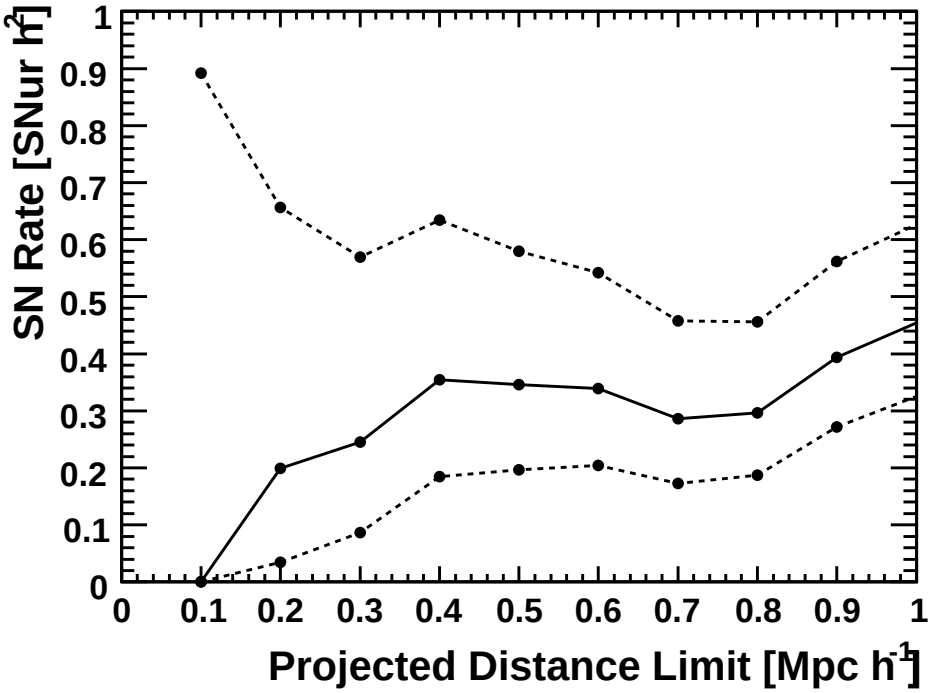

Figure 6.6: maxBCG cluster SN rate as a function of limit on the projected distance. The dashed lines represent the 1-sigma upper and lower limit of the SN rate.

type-Ib/c and type-II SNe. For comparison, Mannucci et al. (2008) have measured the type-Ib/c SN rate in galaxy clusters as $0.14^{+0.16}_{-0.09}$ SNuB h^2 based on 2.5 SNe, and type-II SN rate as $0.41^{+0.29}_{-0.18}$ SNuB h^2 based on 5 SNe. While the SDSS-II Supernova Survey provides weak constraints on the CC SN rate in galaxy clusters, the Mannucci et al. (2008) results are the only existing cluster CC measurements, and so it is worthwhile to confirm that our constraints are consistent.

6.5.4 Radial Distribution of Cluster SNe

Förster & Schawinski (2008) have studied the radial distribution of SNe in early-type galaxies. The sample of SNe includes an unspecified number of SNe from the SDSS-II Supernova Survey. Here we consider the radial distribution for SNe for field and

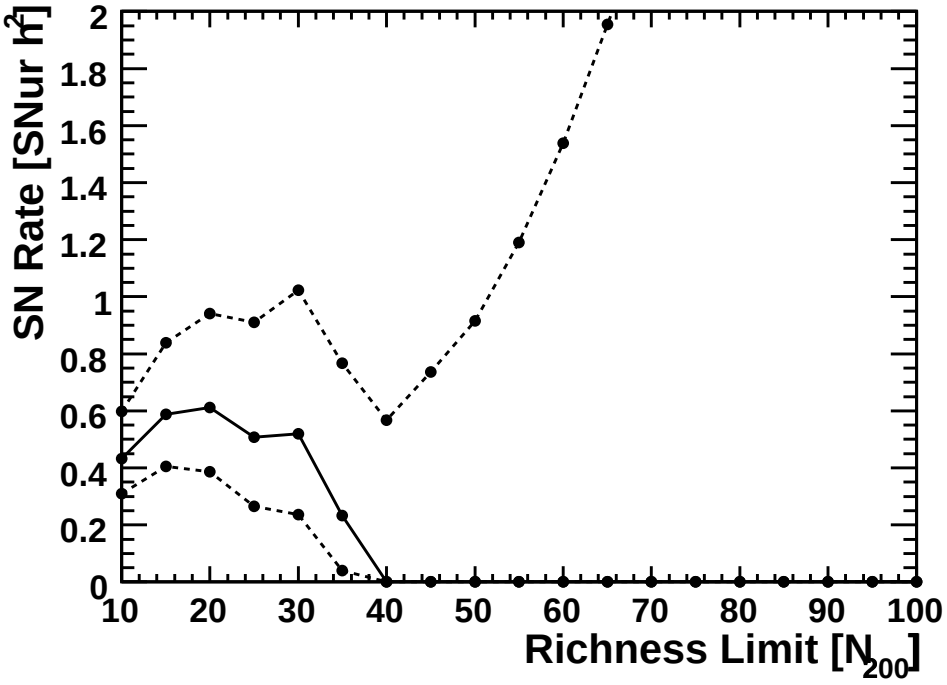

Figure 6.7: maxBCG cluster SN rate as a function of lower limit on the cluster richness measure, N_{200}. The dashed lines represent the 1-sigma upper and lower limit of the SN rate.

cluster ellipticals.

To construct the sample of early-type galaxies, we employ the following procedure. We first assign a host galaxy to each SNe by locating the nearest host from the SDSS database, in units of the isophotal radius of the host galaxy in r-band. The algorithm is described in detail in §4.4.3. Early-type galaxies are defined as those host galaxies that satisfy the following criteria:

- $u - r > 2.4$
- $r < 21.5$
- $\Delta r < 0.05$

It is a well established result that the $(u-r)$ color for SDSS galaxies is bi-modal, with early-type galaxies generally having $(u-r) > 2.4$. The requirement that $r < 21.5$ is imposed as the separation of stars and galaxies is fairly robust to this limit. The requirement that $\Delta r < 0.05$ is imposed to remove outlying, poorly measured galaxies. The distributions of the distance of each SNe from its host galaxy, for field and cluster early-type hosts, is shown in Figure 6.8, and the normalized distributions are shown in Figure 6.9. For field early-type galaxies, a fit of the data to a Sersic model of the luminosity distribution, $dN/dr = A\ \rho\ e^{-\alpha\rho^{-\beta}}$, where ρ denotes the distance of the SN in units of the deVaucouleurs radius of the host galaxy, gives a value for β of 0.23 ± 0.08, which is consistent with a deVaucouleurs profile ($\beta = 0.25$). Since the distribution of light in early-type galaxies is known to follow a deVaucouleurs profile, the result of the fit confirms the results of Förster & Schawinski (2008) that the SN rate in field ellipticals is well represented by a constant rate per unit luminosity. The radial distribution for SNe in cluster early-type galaxies is not compatible with a deVaucouleurs profile, having an enhancement at small radial separations (an attempt to fit the cluster radial distribution to a Sersic profile did not converge). This enhancement is possible evidence for a component of the cluster SN Ia rate that tracks residual star formation activity in cluster early-type galaxies. Such an enhancement is in qualitative agreement with the larger SN Ia rate in cluster ellipticals, compared with field ellipticals, mentioned above and by Mannucci et al. (2008). A KS test on the radial distributions of SNe Ia in cluster and field ellipticals results in an $\approx 19\%$ probability that the data are drawn from the same underlying distribution.

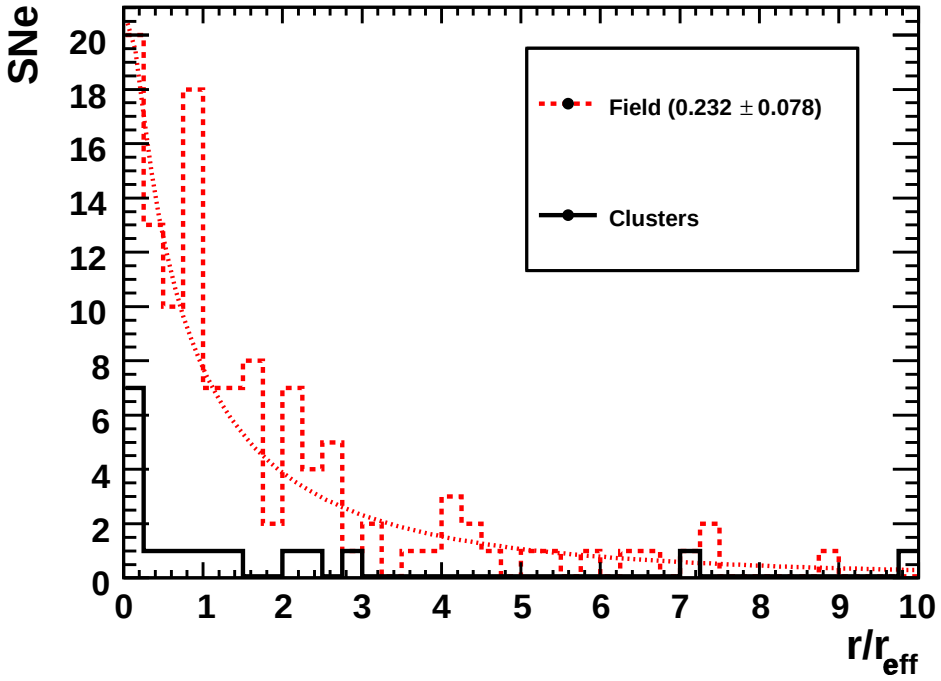

Figure 6.8: Radial distribution of SNe in early-type host galaxies.

6.6 Summary of Cluster SN Studies

In this Chapter we have presented measurements of the type Ia SN rate in galaxy clusters over the redshift range $0.03 < z < 0.30$. These measurements are based on 16 (19) SNe Ia from the first 2 (3) seasons of the SDSS-II Supernova Survey and represent a significant statistical contribution to the study of the type-Ia SN rate in galaxy clusters. Our results on the type Ia SN rate are consistent with previously published measurements, both in the local universe, and at redshift $\approx 0.15 - 0.25$. In turn, the local and low-redshift SN cluster rates are consistent with the SN Ia rate at $z \approx 0.45$ and at $z \approx 0.9$. The current cluster SN Ia rate measurements show no compelling evidence for an increase in the SN rate, as a function of lookback time, as has been well-established for the volumetric SN Ia rate. It should be emphasized,

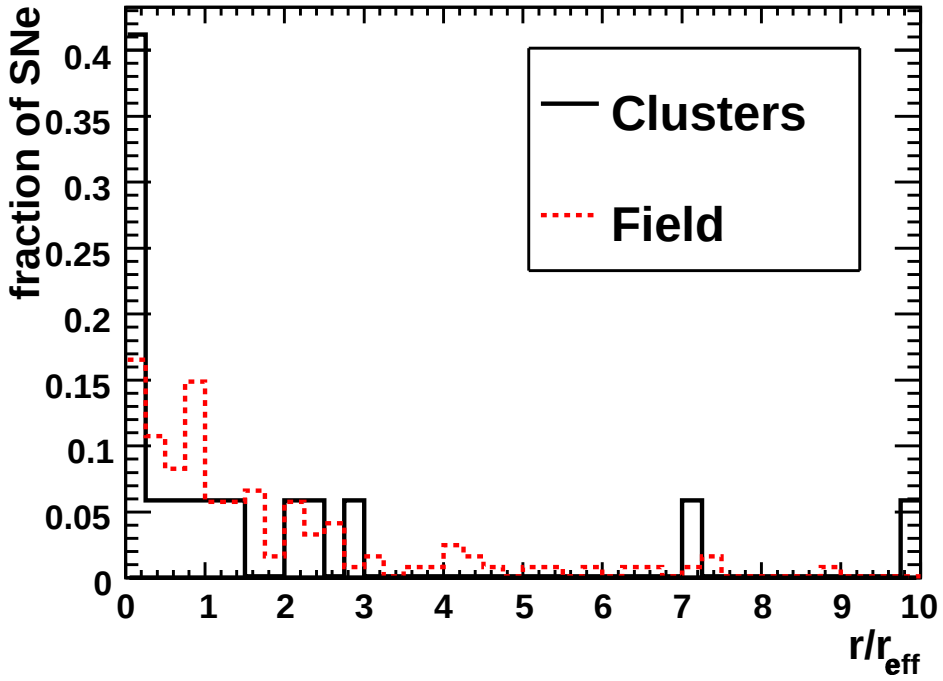

Figure 6.9: Normalized radial distribution of SNe in early-type host galaxies.

however, that the existing cluster SN rate measurements are based on small samples and the measurements do not rule out a redshift dependence to the cluster SN rate.

Although the SDSS-II Supernova Survey was concerned primarily with discovering SNe Ia, 1 type II SN and 1 Ib/c were also discovered in low-redshift galaxy clusters, and we have used these detections to place lower limits on the cluster CC SN rate. These limits represent the 2nd study of CC SNe in galaxy clusters, and are therefore an important consistency check.

We have presented the first study of the radial distribution of SNe Ia in cluster early-type galaxies. The radial distribution for SNe in cluster early-type galaxies is not compatible with a deVaucouleurs profile and suggests a possible enhancement of the SN Ia rate at small radial separations.

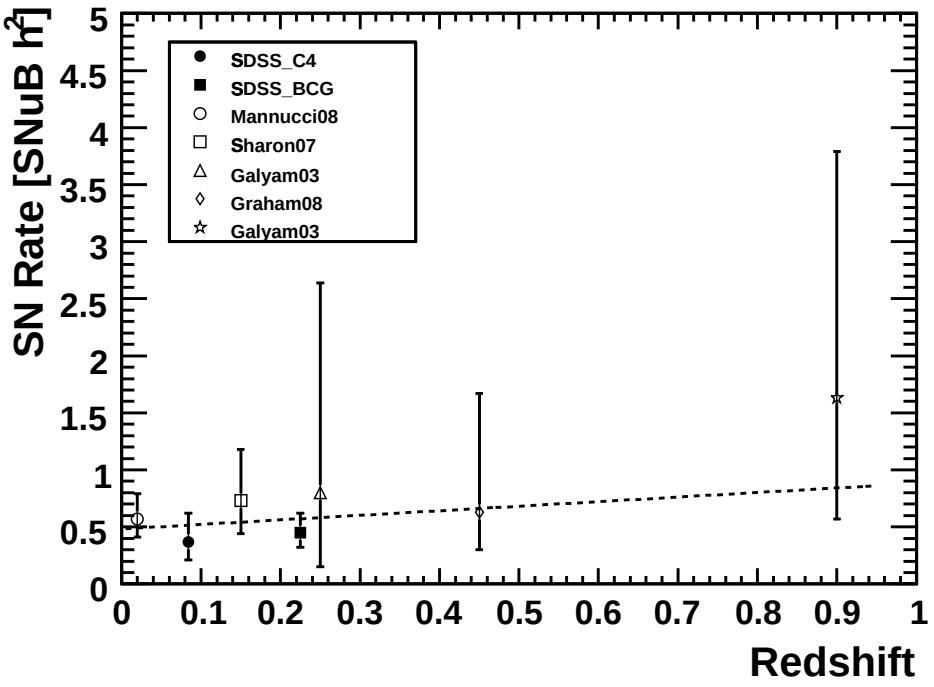

Figure 6.10: Cluster SN Ia rate vs. redshift. The dashed line shows the best fit to a linear model of the SN rate as a function of redshift.

Table 6.4. SNe in c4 Clusters

SDSS Id	SN[a] Type	Cluster Ra (J2000)	Cluster Dec (J2000)	Cluster Redshift	SN Redshift	Projected Dist. (Mpc h^{-1})	Ngals
694	Ia-photo+z	-29.862610	-0.539100	0.1268	0.1270	0.6257	29
6295	Ia	+23.728901	-0.651600	0.0814	0.0796	0.3283	38
13905	Ia-photo+z	+11.549000	+0.348700	0.1153	0.1160	0.8729	5
14279	Ia	+18.786699	+0.297200	0.0450	0.0454	0.7485	128
16215	Ia	+18.786699	+0.297200	0.0450	0.0466	0.9740	128
16280[b]	Ia	+14.270500	-0.918800	0.0443	0.0381	0.8201	13
16280[b]	Ia	+14.067200	-1.255100	0.0442	0.0381	0.1471	65
18375	Ia	+11.566400	+0.002000	0.1140	0.1180	0.3334	34
18890	Ia	+16.431700	-0.849800	0.0669	0.0664	0.3381	5
19968	Ia	+24.344700	-0.447200	0.0558	0.0560	0.4120	19

Note. — SDSS Id denotes internal candidate designation. SNe listed below the double line are from the 2007 SN observing season

[a] "Ia" refers to spectroscopically identified SN; see §2.4. "Ia-photo+z" refers to photometrically identified SN *with* a spectroscopically measured host galaxy redshift; see §4.2.2

[b] SN does not satisfy the color-typing criteria. See §5.2.

Table 6.5. SNe in maxBCG Clusters.

SDSS Id	SN[a] Type	Cluster Ra (J2000)	Cluster Dec (J2000)	Cluster Redshift	SN Redshift	SN Redshift Error	Projected Dist. (Mpc h^{-1})	Ngals
694	Ia-photo+z	-29.789185	-0.567645	0.1243	0.1270	···	0.5629	23
1740	Ia-photo+z	+5.347534	-0.825806	0.1837	0.1673	···	0.8637	25
1782	Ia-photo	-22.141052	+0.295310	0.2781	0.2454	0.0187	0.8347	12
5549	Ia	+3.218521	+0.222306	0.1405	0.1210	···	0.3346	16
5717	Ia	+17.953421	-0.018172	0.2646	0.2517	···	0.9690	16
7363	Ia-photo+z	+18.016899	-0.731066	0.1810	0.1800	···	0.7923	30
13073	Ia-photo	-24.003845	+0.103579	0.2889	0.3285	0.0377	0.8807	15
13655	Ia	+39.036507	-1.006550	0.2727	0.2644	···	0.3489	13
14340	Ia-photo	-14.180206	-0.853948	0.2754	0.2911	0.0251	0.1207	37
15201	Ia	-22.467316	-0.003727	0.2188	0.2085	···	0.2015	32
15498[b]	Ia-photo	+20.494303	+0.334277	0.1701	0.1937	0.0251	0.2868	23
15823	Ia-photo+z	-45.795502	+0.250067	0.2296	0.2150	···	0.9827	22
16452[b]	Ia-photo	-37.507294	-0.329881	0.1323	0.1609	0.0155	0.6129	23
16467	Ia-photo+z	-31.402069	+0.084372	0.2106	0.2200	···	0.4584	21
17435	Ia	+20.365072	+0.021923	0.2160	0.2220	···	0.5505	18
17568	Ia	-46.959778	+0.331601	0.1486	0.1400	···	0.7143	23
18375	Ia	+11.600840	+0.002384	0.1188	0.1180	···	0.5783	23
18909	Ia?	+5.794012	+0.976334	0.2296	0.2270	···	0.1866	16
19341	Ia	+15.847496	+0.319447	0.2539	0.2350	···	0.2750	22
19969	Ia	+31.880201	-0.247330	0.1593	0.1753	···	0.7688	15

Note. — SDSS Id denotes internal candidate designation. SNe listed below the double line are from the 2007 SN observing season

[a] "Ia" and "Ia?" refer to spectroscopically identified SNe; see §2.4. "Ia-photo+z" and "Ia-photo" refer to photometrically identified SNe *with* and *without* a spectroscopically measured host galaxy redshift, respectively; see §4.2.2

[b] SN does not satisfy the p_{Ia} criteria. See §5.2.

Table 6.6. CC SNe in Clusters

SDSS Id	SN Type	Ra (J2000)	Dec (J2000)	Cluster Redshift	SN Redshift	Projected Dist. (Mpc h^{-1})	Ngals
13195	112	38.090099	1.1747000	0.0220999	0.0209999	0.6611930	6
18297	113	16.431699	-0.849799	0.0669	0.0740000	0.9674547	5
20838	113	-21.21780	-1.108899	0.0899000	0.0949999	0.0086120	20

Note. — SDSS Id denotes internal candidate designation.

CHAPTER 7

CONCLUSIONS

In this thesis I have described studies of the type Ia SN rate from the SDSS-II Supernova Survey, a dedicated SN search program that was carried out during the Fall months (Sept. -Nov.) of 2005-2007. The SDSS-II Supernova Survey was extraordinarily successful, discovering ≈ 500 spectroscopically confirmed type Ia SNe in 9 months of observing. This yield represents $\approx 15\% - 20\%$ of all SNe Ia discovered since 1885. There are several features of the SDSS-II Supernova Survey that made it well suited for making precision measurements of the type Ia SN rate. In contrast to many previous SN surveys that targeted known galaxies, the SDSS-II Supernova Survey was a "rolling" survey that observed the same ≈ 300 square degree region of the sky, in the 5 SDSS filters, *ugriz*, with an average observation frequency of once every 4 days. This means that the SDSS-II Supernova Survey was not biased against discovering SNe in faint galaxies, and the SN rate based on SDSS-II Supernova Survey data can be measured directly without the need to extrapolate rates per unit luminosity to unobserved galaxies. Spectroscopic confirmation of SN type was provided through extensive follow-up programs on a variety of telescopes, leading to a high purity of the SN rate sample, particularly at low-redshifts. However, spectroscopic follow-up was not possible for every SN candidate discovered, and the well-sampled, multi-color SN light curves obtained allow us to efficiently identify SN Ia in these cases and to make a correction to the SN rate sample to account for spectroscopic incompleteness. I have described the SDSS-II Supernova Survey observations and SN search algorithms, including description of studies of the SN discovery efficiency of the survey using simulated SNe (fakes) which were inserted directly into the data stream, and a classification algorithm that was developed and implemented to greatly reduce

the human effort necessary on a day-to-day basis for efficiently identifying SNe from among the many transients detected by the SDSS-II Supernova Survey.

Using 17 SNe from the first year of the SDSS-II Supernova Survey, we have made a precise measurement of the SN Ia rate at redshift $z < 0.12$. If we assume that the SN Ia rate is constant over the redshift range considered, we find a value for the volumetric SN Ia rate of

$$r_V = [2.93^{+0.17}_{-0.04}(\text{systematic})^{+0.90}_{-0.71}(\text{statistical})] \times 10^{-5} \text{ SNe Mpc}^{-3}\ h^3_{70}\ \text{year}^{-1}.$$

This measurement is based on a SN Ia sample with a high purity and with a well determined efficiency based on the fakes mentioned above, as well as on additional MC studies. Using this measurement, in combination with several additional published SN rates, we have used a maximum likelihood method to fit the data to models of the SN Ia rate as a function of redshift. The maximum likelihood formalism avoids binning the SN observations and thereby makes optimal use of the SN data, and this is the first time the method has been used in combining multiple data sets. The results confirm that the SN rate is an increasing function of redshift, with a best fit power-law exponent of 1.5 ± 0.6. We also fit the SN data to a simple approximation to a distribution of delay times for SNe Ia that includes a "prompt" and a "delayed" component to the SN rate. With the model for the volumetric SN rate expressed as $r_V(t) = A\rho(t) + B\dot{\rho}(t)$, where $\rho(t)$ is the stellar mass density, we obtain values for A and B of

$$\begin{aligned} A &= (2.8 \pm 1.2) \times 10^{-14} \text{ SNe M}_\odot^{-1} \text{ yr}^{-1} \\ B &= (9.3^{+3.4}_{-3.1}) \times 10^{-4} \text{ SNe M}_\odot^{-1} \end{aligned}$$

with a correlation coefficient $\rho_{AB} = -0.78$.

Using ≈ 350 SNe from the first 2 years of the SDSS-II Supernova Survey, we have also measured the SN Ia rate to a redshift limit of $z \lesssim 0.3$. This represents the largest single sample of SNe that have been used in a SN rate determination in the same redshift range. The size of the SN sample and the redshift coverage allows for constraining the redshift dependence of the SN rate in the redshift range covered by the SDSS-II Supernova Survey. We find a slope of the SN rate, modeled as a linear function of redshift, to be $dr_V/dz = (1.45^{+1.07}_{-0.90}) \times 10^{-4}$ SNe yr^{-1} Mpc^{-3} h^3_{70}. Additionally, this study has provided the first statistically significant measurement if the SN rate at redshift $0.2 < z < 0.3$.

We have measured the SN Ia rate in galaxy clusters in the redshift range $0.03 < 0.30$. The galaxy clusters covered by the SDSS-II Supernova Survey include 71 clusters at $z \lesssim 0.17$ from the c4 cluster catalog and 471 clusters at $0.1 < z < 0.3$ from the maxBCG cluster catalog. We obtain values for the SN Ia rate in galaxy clusters, per unit stellar mass, of $0.10^{+0.068}_{-0.043}$ SNuM h^2 in c4 clusters and $0.12^{+0.046}_{-0.034}$ SNuM h^2 in maxBCG clusters. These measurements are based on 16 (19) total SNe from the first 2 (3) seasons of the SDSS-II Supernova Survey and constitute a significant statistical contribution to the study of the SN rate in galaxy clusters, which thus far have been based on ≈ 25 total SNe Ia from 5 separate SN rate measurements. Combined with previous cluster rate measurements, the SDSS measurements are consistent with a constant SN cluster rate, as a function of redshift.

The SDSS-II Supernova Survey ranks among the most successful SN survey programs that have been carried out, and the SN rate measurements presented in this thesis are the preeminent measurements in the redshift range covered by the SDSS-II Supernova Survey. The improvements in SN rate measurements provided by the SDSS-II Supernova Survey are due to both greater statistical power and reduced sys-

tematic uncertainties in comparison to previous measurements. In combination with improved measurements of the cosmic star formation history and detailed predictions of the distribution of delay times, the SN rate measurements presented here are an important component in placing constraints on SN Ia progenitor systems.

APPENDIX A

SOFTWARE FOR ARTIFICIAL SNE

The SN difference imaging software is organized as a set of *stages* which run sequentially on the SN imaging data. For reference we describe here the stages that were used for inserting artificial SNe (fakes) into the imaging data.

- `SDSSFAKESELECT`: To minimize computation time for inserting fakes into the data-stream, and still retain the ability to simulate the magnitude at an arbitrary light-curve epoch, a range of dates for which the fake magnitude is within the expected limit of the SDSS telescope was computed. This stage checks the library of fakes to see whether any fake has a position within the limits of the field, and that the present MJD falls within the expected range of observability.

- `STARDOPHOT_FAKE`: This stage performs doPhot photometry on calibration stars within the frame. This is necessary to dynamically derive the magnitude to ADU conversion for the fakes.

- `SDSSZERO_FAKE`:

  This stage performs zeropointing of the frame. The magnitudes and magnitude errors of the calibration stars are first converted to flux units via $10^{-0.4m}$, and then the model, ADU counts = A*flux, is solved for A using the weighted least-squares procedure. The zeropointing algorithm does iterative sigma clipping at $\{24.0, 12.0, 6.0, 6.0, 6.0\}$ standard deviations from the best fit zeropoint model. The final zeropoint, the statistical error on the zeropoint, and the RMS of the zeropoint are then converted into magnitudes and stored for use during the SN search.

- `SDSSFAKEINSERT`: This stage inserts the fake into the search image. Given the current MJD and the fake light-curve parameters described above, the theoretical magnitude is computed in real-time. The light-curve model is identical to the stretch model used for online photometric typing, as described in § 2.2. Given the magnitude and the zeropoint computed above, an integrated flux value is computed. The PSF model for the fake comes from the `photo` derived PSF, and this is remapped to the astrometric grid of the search image and photometrically scaled. Poisson noise is then added to each pixel. Finally, the unperturbed search image is copied and the ADU values for each pixel are overlayed on the search image, which is then passed on to the subsequent stages as any other image. A record of changes to the image is written to the corrected frame file header, and the magnitudes and corresponding MJD are written to a `MySQL` database.

APPENDIX B

SDSS-II SUPERNOVA SURVEY SN DATA

Table B.1: SN Runs From SDSS-II

Run	Start Ra	End Ra	Square Degrees	Strip	MJD
5566	-32.7210	+58.9064	123.70	N	53616
5590	-50.6736	+9.9580	81.85	N	53623
5603	-50.6167	+60.1703	149.56	N	53626
5610	-50.5728	+60.2144	149.56	N	53628
5622	-50.7216	+60.6626	150.37	N	53635
5633	-50.6759	+36.4534	117.62	N	53637
5642	-9.8218	+60.6936	95.20	N	53639
5654	-55.4167	-53.0216	3.23	N	53641
5658	+16.0813	+54.5587	51.94	N	53641
5670	-55.5309	+60.7919	157.04	N	53644
5702	-55.5516	-46.4217	12.33	N	53649
5709	-51.6048	+23.2483	101.05	N	53654
5719	-55.4485	+1.1377	76.39	N	53656
5731	+21.1652	+60.6898	53.36	N	53657
5743	-55.4222	-26.9797	38.40	N	53663
5744	-29.7455	+57.8340	118.23	N	53663
5759	-55.5191	+57.8067	152.99	N	53665
5765	+2.2999	+54.8569	70.95	N	53666
5770	-55.5363	+57.9406	153.19	N	53668
5777	+25.6116	+57.9581	43.67	N	53669
5781	-55.3144	+57.8638	152.79	N	53670

Continued on Next Page...

Table B.1 – Continued

Run	Start Ra	End Ra	Square Degrees	Strip	MJD
5792	-55.4171	+57.9081	152.99	N	53673
5800	-55.6072	+56.0717	150.77	N	53675
5808	+49.2695	+57.9570	11.73	N	53676
5813	-55.5580	+44.5945	135.21	N	53677
5823	-55.4651	+60.7055	156.83	N	53680
5842	-55.4335	+60.7569	156.86	N	53683
5864	-50.0582	-45.4170	6.27	N	53686
5865	-42.9646	-18.1076	33.56	N	53686
5866	+18.2081	+60.7267	57.40	N	53686
5872	+25.1426	+60.7813	48.11	N	53687
5878	-59.9846	+60.6845	162.90	N	53693
5898	-59.9839	-33.6336	35.57	N	53698
5902	-60.1275	+18.7818	106.53	N	53699
5909	-59.3483	-4.1011	74.58	N	53702
5915	-60.0099	-27.0694	44.47	N	53703
5918	-54.4629	+60.6699	155.43	N	53704
6281	-56.8151	-34.5157	30.10	N	53974
6283	-11.6869	+12.4179	32.54	N	53974
6293	+7.3097	+13.4481	8.29	N	53977
6313	-60.0547	-45.9880	18.99	N	53989
6314	-47.3922	+60.7007	145.93	N	53989

Continued on Next Page...

Table B.1 – Continued

Run	Start Ra	End Ra	Square Degrees	Strip	MJD
6360	-59.9831	-14.9232	60.83	N	53995
6362	+9.1340	+25.9021	22.64	N	53995
6363	+25.6678	+40.0410	19.40	N	53995
6370	-59.9855	-26.1529	45.67	N	53997
6373	-17.2155	+8.0885	34.16	N	53997
6374	+38.1569	+50.8833	17.18	N	53997
6383	-32.8816	+53.5014	116.62	N	54000
6391	-60.0594	-54.5203	7.48	N	54003
6400	-60.0229	-30.9813	39.21	N	54005
6409	-32.7864	+60.7843	126.32	N	54006
6412	-58.9070	-24.1769	46.89	N	54007
6414	-25.9317	+54.9144	109.14	N	54007
6418	+53.2129	+60.6989	10.11	N	54008
6421	-60.1227	+60.6906	163.10	N	54009
6430	-60.1048	+60.7122	163.10	N	54011
6435	+36.0857	+54.3520	24.66	N	54012
6441	-60.1309	+6.6361	90.14	N	54019
6444	+21.1347	+60.6613	53.36	N	54019
6450	-6.7389	+60.7854	91.16	N	54021
6461	-60.1077	+60.7147	163.11	N	54025
6474	-60.0549	+31.4129	123.48	N	54029

Continued on Next Page...

Table B.1 – Continued

Run	Start Ra	End Ra	Square Degrees	Strip	MJD
6476	+30.5602	+60.6573	40.63	N	54029
6484	-60.0057	+60.6558	162.89	N	54031
6504	-59.9953	+60.6669	162.89	N	54036
6513	-60.0811	+60.7310	163.10	N	54039
6522	-60.0047	-31.8607	37.99	N	54041
6524	+6.1049	+60.7485	73.77	N	54041
6533	-60.0972	+39.6067	134.60	N	54048
6534	+38.6957	+60.7052	29.71	N	54048
6548	-60.0292	-22.0052	51.33	N	54051
6552	-60.0476	+60.7695	163.10	N	54052
6559	-60.0597	+14.0519	100.05	N	54054
6564	-60.0990	+30.1769	121.87	N	54055
6565	+28.1694	+60.6596	43.86	N	54055
6577	-59.9913	+60.6790	162.90	N	54058
6584	-42.8337	+60.7807	139.88	N	54060
6600	-60.0977	+34.8219	128.14	N	54063
6609	+33.1803	+60.7304	37.19	N	54065
6920	-60.2247	-10.0997	67.67	N	54346
6921	+24.0490	+54.8916	41.64	N	54346
6934	-14.7061	+55.8107	95.20	N	54348
6947	+32.2487	+38.0875	7.88	N	54355

Continued on Next Page...

Table B.1 – Continued

Run	Start Ra	End Ra	Square Degrees	Strip	MJD
6951	-52.7023	-20.6660	43.25	N	54356
6958	-60.0728	+60.7450	163.10	N	54358
6961	-39.5388	-34.7480	6.47	N	54359
6962	-34.7345	+2.3945	50.12	N	54359
6963	+1.4230	+25.5273	32.54	N	54359
6982	-27.8584	+60.7718	119.65	N	54365
6985	-60.0702	-35.3699	33.35	N	54366
7003	-46.8591	-32.9372	18.79	N	54373
7006	-34.2355	+1.5483	48.31	N	54373
7033	-48.5072	-30.2433	24.66	N	54381
7034	-15.5143	+60.6925	102.88	N	54381
7037	-60.0637	-11.1103	66.09	N	54382
7043	-53.5537	-33.4930	27.08	N	54383
7047	+9.4094	+44.1449	46.89	N	54384
7054	-56.4651	+60.7613	158.26	N	54386
7060	-59.5227	+60.7000	162.30	N	54388
7077	+18.9234	+60.6972	56.39	N	54392
7080	-60.1219	+15.0337	101.46	N	54393
7081	+15.5735	+60.7927	61.05	N	54393
7092	-60.0792	-28.9422	42.03	N	54396
7095	+10.5430	+60.6963	67.71	N	54396

Continued on Next Page...

Table B.1 – Continued

Run	Start Ra	End Ra	Square Degrees	Strip	MJD
7106	-60.0166	+60.7951	163.10	N	54403
7111	-20.2264	-14.2384	8.08	N	54404
7112	-5.2996	+34.5266	53.77	N	54404
7117	-13.0715	+38.8825	70.14	N	54405
7121	-60.0510	+60.7602	163.10	N	54406
7130	-60.0577	+60.7550	163.10	N	54409
7140	-59.5602	+18.2857	105.09	N	54412
7142	+18.4658	+60.6869	57.00	N	54412
7150	-59.4699	-35.9643	31.73	N	54415
7155	-59.7721	+60.7431	162.70	N	54416
7167	-29.3335	-14.5113	20.01	N	54420
7170	-59.4530	+60.7670	162.30	N	54421
7176	-59.5477	-25.1152	46.48	N	54423
7177	-6.4808	+60.7389	90.75	N	54423
7188	-59.4204	-20.4957	52.55	N	54425
7195	-48.5472	+25.8669	100.46	N	54431
7199	+12.9608	+60.7217	64.48	N	54432
7202	-39.5836	+60.7363	135.43	N	54433
5582	-40.3578	+57.4054	131.98	S	53622
5597	-50.6178	-18.4316	43.45	S	53625
5607	-50.5910	+59.8966	149.16	S	53627

Continued on Next Page...

Table B.1 – Continued

Run	Start Ra	End Ra	Square Degrees	Strip	MJD
5619	-50.6799	+60.7057	150.37	S	53634
5628	-50.7010	+1.9944	71.14	S	53636
5637	-20.7203	+60.7236	109.95	S	53638
5646	-13.8538	+60.7035	100.65	S	53640
5666	+41.2460	+60.7096	26.28	S	53643
5675	-55.5226	-41.7499	18.59	S	53645
5681	+29.9676	+52.8753	30.93	S	53646
5698	-55.6236	-9.8141	61.84	S	53648
5713	-55.5354	+41.4722	130.96	S	53655
5729	-46.9467	-43.0540	5.26	S	53657
5730	+37.1988	+60.7051	31.73	S	53657
5732	+47.1083	+60.7335	18.39	S	53657
5745	+33.0855	+55.0972	29.72	S	53663
5754	-55.5991	+34.3737	121.46	S	53664
5760	+25.1345	+55.6824	41.24	S	53665
5763	-55.4867	+3.9437	80.23	S	53666
5771	+33.0918	+60.7942	37.40	S	53668
5776	-55.5031	+57.8228	152.99	S	53669
5782	+32.6538	+60.6576	37.81	S	53670
5786	-14.8150	+60.6521	101.88	S	53671
5797	-55.5724	+58.0517	153.39	S	53674

Continued on Next Page...

Table B.1 – Continued

Run	Start Ra	End Ra	Square Degrees	Strip	MJD
5807	-47.6672	+57.8946	142.51	S	53676
5820	-44.5412	+59.9635	141.08	S	53679
5836	-55.4841	+60.6972	156.84	S	53681
5847	+25.7116	+60.7446	47.29	S	53684
5853	-58.9471	-19.2755	53.56	S	53685
5870	-55.5706	-6.1632	66.70	S	53687
5871	+31.3923	+60.7350	39.61	S	53687
5882	-60.1057	+60.7064	163.10	S	53694
5889	+44.0099	+60.7792	22.64	S	53696
5895	-60.1151	+60.7064	163.11	S	53697
5905	-59.9883	+60.6862	162.91	S	53700
5924	-60.0649	+60.7589	163.11	S	53705
6287	-58.7794	+60.6962	161.29	S	53975
6330	+1.1732	+27.8222	35.98	S	53990
6348	-31.1948	+2.9395	46.08	S	53993
6349	+26.1051	+38.9807	17.38	S	53993
6353	-59.9949	-48.7678	15.16	S	53994
6355	-5.7804	+59.7952	88.53	S	53994
6367	-47.8229	+60.7172	146.53	S	53996
6377	-60.0009	+14.8517	101.05	S	53998
6401	-50.8974	-41.6160	12.53	S	54005

Continued on Next Page...

Table B.1 – Continued

Run	Start Ra	End Ra	Square Degrees	Strip	MJD
6402	-24.9181	+11.7599	49.52	S	54005
6404	+24.9669	+60.7498	48.31	S	54005
6408	-59.9927	-48.7655	15.16	S	54006
6417	-60.1298	+60.6842	163.10	S	54008
6422	+37.0864	+56.1013	25.67	S	54009
6425	-60.0449	+60.7685	163.10	S	54010
6433	-60.0839	+60.7289	163.10	S	54012
6447	-60.0499	+40.1015	135.20	S	54020
6448	+39.0841	+60.7933	29.31	S	54020
6453	-60.0082	-4.4674	74.98	S	54022
6458	-6.7344	+55.8530	84.49	S	54024
6464	-59.9923	-45.0226	20.21	S	54026
6468	-60.0590	+2.9643	85.08	S	54028
6471	+9.5286	+60.7368	69.13	S	54028
6479	-60.0910	+15.9575	102.67	S	54030
6480	+33.1908	+59.2422	35.17	S	54030
6488	-60.0623	-26.8291	44.86	S	54032
6494	-61.5124	-31.2688	40.83	S	54034
6501	-32.5643	+60.7220	125.94	S	54035
6508	-60.5246	+60.5863	163.50	S	54037
6518	-60.1244	+60.6890	163.10	S	54040

Continued on Next Page...

Table B.1 – Continued

Run	Start Ra	End Ra	Square Degrees	Strip	MJD
6525	+39.1160	+60.6770	29.11	S	54041
6528	-60.1080	-25.2275	47.09	S	54047
6530	-7.9791	+60.7449	92.78	S	54047
6537	-17.3782	+60.7780	105.51	S	54049
6542	-59.9900	-4.5994	74.78	S	54050
6545	+41.2190	+60.6820	26.28	S	54050
6555	-60.0233	+30.9990	122.88	S	54053
6556	+28.3710	+60.7113	43.66	S	54053
6568	-60.0493	+60.7704	163.11	S	54056
6571	-53.7570	-19.3247	46.48	S	54057
6580	-60.0590	+60.7627	163.11	S	54059
6590	-60.0848	-13.5218	62.86	S	54061
6592	+12.0720	+60.7342	65.69	S	54061
6596	-60.0720	+60.7538	163.11	S	54062
6604	+27.2405	+60.7792	45.28	S	54064
6615	-60.0468	-16.7766	58.41	S	54068
6618	-1.8101	+60.7738	84.49	S	54068
6930	-13.7425	+60.5186	100.25	S	54347
6933	-60.0433	-14.0837	62.05	S	54348
6955	-60.1125	+60.7053	163.10	S	54357
6964	+16.3811	+30.9034	19.61	S	54359

Continued on Next Page...

Table B.1 – Continued

Run	Start Ra	End Ra	Square Degrees	Strip	MJD
6976	-19.7235	+60.6733	108.54	S	54362
6981	-60.0533	-19.0353	55.37	S	54365
7013	-22.4841	-8.2618	19.20	S	54376
7016	+15.1591	+60.6735	61.44	S	54376
7018	-60.0402	-50.4596	12.93	S	54377
7024	-60.0280	+15.8730	102.47	S	54379
7038	-1.8830	+60.6984	84.48	S	54382
7051	-60.0570	+60.7632	163.11	S	54385
7057	-59.4918	+60.7315	162.30	S	54387
7071	+14.4300	+60.6948	62.46	S	54390
7074	+14.8106	+60.7773	62.06	S	54391
7076	-60.1189	+14.8882	101.26	S	54392
7084	-59.9870	+60.6843	162.91	S	54394
7096	+18.4160	+60.7919	57.21	S	54396
7101	-55.5534	+60.7896	157.06	S	54402
7110	-60.1022	-22.0787	51.33	S	54404
7124	-59.0697	-17.0035	56.79	S	54407
7127	-60.0576	+60.7547	163.10	S	54408
7133	-57.8985	-22.8683	47.29	S	54410
7136	-44.5234	+60.7171	142.07	S	54411
7145	-59.7253	+60.7887	162.69	S	54413

Continued on Next Page...

Table B.1 – Continued

Run	Start Ra	End Ra	Square Degrees	Strip	MJD
7151	-14.5459	-8.5578	8.08	S	54415
7152	-6.4997	+59.8236	89.54	S	54415
7158	-0.6362	+60.7464	82.87	S	54417
7161	-59.5774	+60.7890	162.49	S	54418
7173	-59.4763	+60.7442	162.30	S	54422
7182	-59.4824	-14.1210	61.24	S	54424
7183	+10.4266	+60.7274	67.91	S	54424

Table B.2: SNe Ia From SDSS-II

SDSS SN ID	Ra	Dec	IAU Name	Redshift
722	0.705670	0.751323	2005ed	0.08658
739	14.595293	0.679057	2005ef	0.10768
744	-30.801477	0.317490	2005ei	0.12780
762	15.535367	-0.879020	2005eg	0.19152
774	25.463507	-0.876397	2005ex	0.09350
1032	46.795700	1.119545	2005ez	0.12975
1112	-20.982510	-0.375230	2005fg	0.25773
1119	-39.586452	0.894650	2005fc	0.29740
1166	9.355610	0.973275	···	0.38240
1241	-22.327442	-0.776597	2005ff	0.08700
1253	-36.201015	0.163140	2005fd	0.26200
1316	-25.136168	0.494423	2005fe	0.21660
1371	-10.626193	0.429387	2005fh	0.11915
1580	45.323078	-0.644057	2005fb	0.18300
1686	2.248345	-0.210410	···	0.13640
1688	-38.642281	0.324540	···	0.35870
1794	-42.163132	-0.445363	2005fj	0.14260
2017	-31.056664	0.593530	2005fo	0.26160
2030	-48.158394	-1.253303	2005fl	0.23360
2031	-47.956779	-1.171423	2005fm	0.15300
2102	-47.778976	0.191117	2005fn	0.09510

Continued on Next Page...

Table B.2 – Continued

SDSS SN ID	Ra	Dec	IAU Name	Redshift
2165	17.091743	-0.096317	2005fr	0.28800
2246	50.090427	-0.885580	2005fy	0.19520
2308	34.272915	0.280263	2005ey	0.14800
2330	6.807040	1.120617	2005fp	0.21320
2372	40.520737	-0.540823	2005ft	0.18120
2422	1.994545	0.638180	2005fi	0.26500
2440	42.633698	0.807815	2005fu	0.19300
2533	31.220730	-0.326450	2005fs	0.34000
2561	46.343430	0.858373	2005fv	0.11819
2635	52.704334	-1.238107	2005fw	0.14330
2689	24.900356	-0.758740	2005fa	0.16153
2789	-15.798573	0.401087	2005fx	0.29030
2916	-44.078251	0.569525	2005fz	0.12420
2943	17.704912	1.007900	2005go	0.26540
2992	55.497055	-0.782667	2005gp	0.12656
3080	16.932346	-1.039507	2005ga	0.17420
3087	20.406733	-0.977217	2005gc	0.16460
3199	-26.707273	1.050585	2005gs	0.25110
3241	-47.348545	-0.354100	2005gh	0.25888
3256	-30.732361	-0.223435	2005hn	0.10760
3317	26.962614	0.640613	2005gd	0.16070

Continued on Next Page...

Table B.2 – Continued

SDSS SN ID	Ra	Dec	IAU Name	Redshift
3331	34.561371	0.796550	2005ge	0.20600
3377	54.156204	1.079170	2005gr	0.24510
3451	-25.930771	0.708193	2005gf	0.25000
3452	-25.328501	0.639207	2005gg	0.23040
3592	19.052420	0.791947	2005gb	0.08656
3901	14.850420	0.002597	2005ho	0.06283
4000	31.016006	-0.365817	2005gt	0.27860
4046	-5.501650	0.642137	2005gw	0.27700
4064	46.109684	1.046413	···	0.15648
4241	12.237720	-0.905790	2005gu	0.33200
4524	45.299824	-0.553860	2005gj	0.06160
4577	38.475544	0.280713	2005gv	0.36300
4679	21.528299	0.676887	2005gy	0.33240
5103	-0.115557	0.737143	2005gx	0.14600
5183	53.454025	0.709360	2005gq	0.38980
5350	-52.780830	-0.779265	2005hp	0.17540
5391	52.341930	-1.094720	2005hs	0.30090
5395	49.640877	0.123405	2005hr	0.11700
5533	-31.330009	0.413270	2005hu	0.21970
5549	3.250533	0.248247	2005hx	0.12100
5550	3.598277	0.333087	2005hy	0.15620

Continued on Next Page...

Table B.2 – Continued

SDSS SN ID	Ra	Dec	IAU Name	Redshift
5588	2.368630	1.154895	2005hw	0.41020
5635	-26.817249	-0.034883	2005hv	0.17950
5717	17.895931	-0.005840	2005ia	0.25170
5736	22.862774	-0.631670	2005jz	0.25300
5737	22.857071	-0.603420	2005ib	0.39300
5751	11.634090	0.838350	2005hz	0.13000
5821	-47.417583	-0.825290	2005hq	0.40080
5844	-32.213806	-0.842940	2005ic	0.31080
5916	5.437367	-0.325013	2005is	0.17240
5944	29.199770	-0.213630	2005hc	0.04594
5957	34.760555	-0.272783	2005ie	0.27960
5966	16.190372	0.513930	2005it	0.30955
5994	-47.397480	-0.167877	2005ht	0.18700
6057	52.553619	-0.974587	2005if	0.06709
6100	-26.516821	1.086505	2005ka	0.31770
6108	1.806593	0.348973	2005ih	0.25950
6127	-22.676027	-0.092337	2005iw	0.28000
6137	-52.063850	0.244760	2005iv	0.30010
6192	-11.535010	1.257000	2005jy	0.27200
6196	-22.368876	-0.502647	2005ig	0.28070
6249	3.265527	-0.620110	2005ii	0.29440

Continued on Next Page...

Table B.2 – Continued

SDSS SN ID	Ra	Dec	IAU Name	Redshift
6295	23.672974	-0.605377	2005js	0.07962
6304	26.497627	1.195950	2005jk	0.19000
6315	-49.517170	1.092020	2005ix	0.26700
6406	46.088573	-1.062947	2005ij	0.12462
6422	-10.861177	-0.663210	2005id	0.18400
6649	34.275890	0.534810	2005jd	0.31400
6696	-20.920660	0.479263	···	0.23790
6699	-37.185005	-1.056990	2005ik	0.31060
6773	-54.935017	0.217395	2005iu	0.09030
6777	-38.783569	0.385625	2005iy	0.40430
6780	-31.931391	0.267097	2005iz	0.20200
6852	53.419842	-0.112120	2005jf	0.30060
6924	-1.030667	0.876967	2005ja	0.32800
6933	11.351710	1.075570	2005jc	0.21300
6936	-36.766178	-0.699777	2005jl	0.18100
6962	38.860867	1.074887	2005je	0.09389
6968	19.555759	-0.906563	···	0.09830
7017	31.365351	-0.497907	···	0.26840
7143	-14.737630	-0.207410	2005jg	0.30400
7147	-9.981593	-0.055487	2005jh	0.10990
7243	-31.920956	0.471970	2005jm	0.20370

Continued on Next Page...

Table B.2 – Continued

SDSS SN ID	Ra	Dec	IAU Name	Redshift
7335	-41.114792	-0.355340	2005kn	0.19747
7426	-20.986610	-0.367927	2005jb	0.38400
7460	-36.415932	-0.681675	2005jx	0.21030
7473	4.326413	-0.257257	2005ji	0.21600
7475	4.753490	-0.281480	2005jn	0.32200
7512	52.090321	-0.326145	2005jo	0.21900
7779	-49.919796	-0.007185	2005jw	0.38120
7847	32.459919	-0.061733	2005jp	0.21240
7876	19.182503	0.794643	2005ir	0.07636
7947	-45.813934	0.408340	2005jj	0.36800
8030	40.208851	0.993120	2005jv	0.42200
8046	39.116840	0.511287	2005ju	0.25930
8151	6.962033	-1.198150	2005hk	0.01306
8213	-2.479047	-0.921407	2005ko	0.18470
8495	-24.738964	-0.748170	2005mi	0.21440
8598	42.667370	-0.065977	2005jt	0.36060
8707	41.236137	0.203660	2005mh	0.39510
8719	7.721477	-0.718860	2005kp	0.11630
8921	-34.998035	-0.007905	2005ld	0.14530
9032	-22.115463	-0.493550	2005le	0.25400
9045	-12.162870	-0.608610	2005kq	0.38950

Continued on Next Page...

Table B.2 – Continued

SDSS SN ID	Ra	Dec	IAU Name	Redshift
9207	19.083639	-0.807803	2005lg	0.35000
9457	-24.185623	0.253050	2005li	0.25690
9467	-31.048611	1.180825	2005lh	0.21840
10028	17.741844	0.276160	2005kt	0.06533
10096	29.429319	-0.179447	2005lj	0.07775
10106	47.693272	-0.204900	···	0.14720
10434	-30.044067	-1.193710	2005lk	0.10430
10449	-22.971340	-1.128220	2005ll	0.24400
10550	-10.324620	-1.204880	2005lf	0.30010
10805	-15.072453	-0.013717	2005ku	0.04546
11067	33.518394	-0.239170	2005ml	0.11400
11206	3.289810	1.145527	2005mm	0.38190
11300	6.750494	-0.586620	2005ln	0.14680
11320	57.553738	-0.240240	2005mo	0.27430
11452	9.299460	-1.203440	2005lo	0.29900
11557	40.400188	0.205010	2005lq	0.38000
11650	16.190300	0.055650	2005mp	0.27300
11864	26.928320	0.207207	2005lp	0.30300
12136	-9.909260	-0.349900	2005mq	0.35000
12778	-42.504166	0.408770	2006fs	0.09923
12779	-50.528126	1.221123	2006fd	0.07996

Continued on Next Page...

Table B.2 – Continued

SDSS SN ID	Ra	Dec	IAU Name	Redshift
12781	5.406560	-1.009973	2006er	0.08431
12841	-38.652752	-1.033663	2006gk	0.29400
12843	-36.121922	-0.980280	2006fa	0.16704
12851	-15.218945	-0.627335	2006gm	0.24960
12853	-43.234451	0.723073	2006ey	0.16940
12855	-29.744476	0.716243	2006fk	0.17070
12856	-27.134529	0.755970	2006fl	0.17173
12860	-36.305809	1.175903	2006fc	0.12170
12869	-32.600876	0.001057	2006ge	0.27900
12874	-6.035380	-0.177130	2006fb	0.24493
12881	10.162356	-0.073583	2006gu	0.23790
12883	-47.374100	0.398685	2006fr	0.30600
12897	18.421391	-0.101587	2006eb	0.01721
12898	26.793100	-0.146973	2006fw	0.08350
12907	20.407873	0.414510	2006fv	0.13182
12927	41.786129	0.775130	2006fj	0.18960
12928	-54.990986	-0.975693	2006ew	0.13970
12930	-50.317234	-0.474537	2006ex	0.14749
12950	-8.332547	-0.840273	2006fy	0.08268
12971	6.648507	-0.302077	2006ff	0.23532
12972	7.958623	-0.382993	2006ft	0.26100

Continued on Next Page...

Table B.2 – Continued

SDSS SN ID	Ra	Dec	IAU Name	Redshift
12977	13.695610	-0.250847	2006gh	0.24700
12979	11.601475	0.003500	2006gf	0.11644
12983	16.458755	0.144805	2006gl	0.26538
13005	27.395475	-0.649895	2006fh	0.12730
13025	-18.432686	0.415893	2006fx	0.22410
13038	-12.173223	0.504620	2006gn	0.10100
13044	-27.457247	0.503270	2006fm	0.12570
13045	-14.975067	0.537673	2006fn	0.18080
13070	-2.214960	-0.746353	2006fu	0.19855
13072	-25.040569	0.024373	2006fi	0.23063
13099	-0.181257	-1.250353	2006gb	0.26607
13135	4.172303	-0.424537	2006fz	0.10469
13136	6.140680	-0.279075	2006go	0.37210
13152	7.052104	0.118013	2006gg	0.20300
13174	13.234697	0.447843	2006ga	0.23600
13254	42.058678	-0.347040	2006gx	0.18068
13305	-28.899536	0.691247	2006he	0.21390
13327	-21.272631	0.002027	2006jf	0.28200
13354	27.564796	-0.887257	2006hr	0.15760
13357	29.472931	-0.534140	2006gw	0.32600
13370	27.151552	0.328227	2006gv	0.19960

Continued on Next Page...

Table B.2 – Continued

SDSS SN ID	Ra	Dec	IAU Name	Redshift
13425	-21.458317	0.054960	2006gp	0.21290
13467	-5.053487	0.205250	2006hq	0.06850
13506	25.243374	-0.727867	2006hg	0.24500
13511	40.612385	-0.794127	2006hh	0.23757
13578	17.394693	0.704147	2006hc	0.20000
13610	-33.985207	0.726270	2006hd	0.29828
13641	-14.781283	-0.981160	2006hf	0.22000
13655	39.020222	-0.994183	2006hs	0.26440
13727	-42.411915	0.932620	2006hj	0.22570
13736	-23.166710	1.030965	2006hv	0.15040
13757	-9.876910	-1.157840	2006hk	0.28900
13796	-9.308413	0.532897	2006hl	0.14500
13830	-8.438320	-0.382257	2006hm	0.33170
13835	6.059633	-0.248247	2006hp	0.24770
13894	1.690563	-0.036750	2006jh	0.12490
13934	-17.889000	-0.435305	2006jg	0.33000
13956	20.941832	0.816670	2006hi	0.26200
14019	-43.357582	-0.647933	2006ki	0.21640
14024	-41.801434	0.916340	2006ht	0.20000
14108	53.594669	-1.123193	2006hu	0.12270
14157	51.136700	1.022387	2006kj	0.21400

Continued on Next Page...

Table B.2 – Continued

SDSS SN ID	Ra	Dec	IAU Name	Redshift
14212	-29.529907	1.045017	2006iy	0.20540
14261	-31.759590	0.253800	2006jk	0.28600
14279	18.488764	0.371677	2006hx	0.04543
14284	49.049355	-0.600947	2006ib	0.18109
14298	-45.104893	1.223257	2006jj	0.26800
14318	-19.574825	-0.136890	2006py	0.05790
14331	7.888657	-0.135800	2006kl	0.22110
14377	48.264309	-0.471627	2006hw	0.13938
14397	6.916140	0.649490	2006kk	0.38570
14421	31.829903	1.252077	2006ia	0.17501
14437	-27.919041	-1.196387	2006hy	0.14910
14451	-51.805058	0.927073	2006ji	0.17840
14456	-16.448891	1.050695	2006jm	0.33000
14481	2.681740	0.201265	2006lj	0.24390
14735	35.158047	0.348417	2006km	0.30110
14782	-45.765732	-0.279047	2006jp	0.16040
14815	-40.928349	0.559500	2006iz	0.13630
14816	-23.283684	0.506050	2006ja	0.10723
14846	7.663240	0.141570	2006jn	0.22470
14871	54.277115	0.009393	2006jq	0.12760
14979	54.946430	0.992820	2006jr	0.17710

Continued on Next Page...

Table B.2 – Continued

SDSS SN ID	Ra	Dec	IAU Name	Redshift
14984	-46.166439	-0.092760	2006js	0.19670
15002	22.249800	0.769953	2006ko	0.38000
15009	32.798557	0.695835	2006kp	0.29500
15129	-41.097469	-0.321385	2006kq	0.19846
15132	-30.299730	0.197725	2006jt	0.14400
15136	-8.837437	-0.718347	2006ju	0.14869
15161	35.842926	0.818997	2006jw	0.24964
15170	58.058578	0.292080	2006jx	0.41000
15171	-55.207462	-1.064470	2006kb	0.11320
15201	-22.480579	0.003663	2006ks	0.20850
15203	15.734763	0.183117	2006jy	0.20430
15213	53.019142	-0.100147	2006lk	0.31120
15217	22.634235	0.219780	2006jv	0.37100
15219	34.611153	0.226687	2006ka	0.24700
15222	2.853353	0.702730	2006jz	0.19939
15229	4.831990	1.090717	2006kr	0.22680
15234	16.958349	0.828197	2006kd	0.13634
15254	-46.507065	-0.360047	2006oy	0.20100
15259	-22.455811	-0.407827	2006kc	0.21003
15287	-36.040314	-1.057427	2006kt	0.27400
15301	-36.420052	0.589120	2006lo	0.29630

Continued on Next Page...

Table B.2 – Continued

SDSS SN ID	Ra	Dec	IAU Name	Redshift
15340	-23.997181	0.821370	2006mu	0.14100
15354	6.773680	-0.126003	2006lp	0.22210
15356	-24.946707	0.409917	2006lm	0.27470
15365	-5.443370	1.249135	2006ku	0.18750
15369	-11.167063	-0.562580	2006ln	0.24500
15383	34.149509	-0.155150	2006lq	0.31620
15421	33.741600	0.602503	2006kw	0.18500
15425	55.561108	0.478300	2006kx	0.16004
15433	14.879636	-0.256530	2006mt	0.22000
15440	39.720646	0.090085	2006lr	0.26190
15443	49.867455	-0.318023	2006lb	0.18202
15453	-40.331680	-1.024283	2006ky	0.14770
15456	-28.132713	-0.903443	2006ll	0.38210
15459	-19.298553	-0.901753	2006la	0.12670
15461	-33.152508	-0.494677	2006kz	0.18000
15466	-42.354954	-0.123223	2006mz	0.24610
15504	-14.298523	-0.876403	2006oc	0.27010
15508	27.168976	-0.576590	2006ls	0.14600
15583	37.731102	0.946297	2006mv	0.17520
15584	43.495461	0.986980	2006nt	0.28200
15648	-46.281620	-0.194827	2006ni	0.17496

Continued on Next Page...

Table B.2 – Continued

SDSS SN ID	Ra	Dec	IAU Name	Redshift
15674	-19.170860	0.262920	2006nu	0.19700
15704	40.210705	0.658755	2006nh	0.36500
15734	5.530280	-0.095643	2006ng	0.39800
15749	51.285324	-0.040610	2006mw	0.11800
15756	0.374817	0.275983	2006nf	0.38800
15776	32.829441	-0.998217	2006na	0.31760
15833	-59.136124	0.570217	2006mx	0.12900
15868	38.099804	-0.713590	2006pa	0.25100
15872	36.722446	-0.327790	2006nb	0.18460
15897	11.681467	-1.032913	2006pb	0.17470
15901	31.976307	-0.535390	2006od	0.17100
16000	21.117599	0.074383	2006nj	0.39850
16021	13.843727	-0.388803	2006nc	0.09470
16032	44.069229	-0.410760	2006nk	0.19500
16069	-18.753946	-1.006603	2006nd	0.12878
16072	3.124467	-0.977297	2006nv	0.28670
16073	8.107767	-1.054033	2006of	0.15310
16093	-9.637490	1.132495	2006oe	0.33510
16099	26.420891	-1.054420	2006nn	0.19686
16100	30.436293	-1.032397	2006nl	0.19000
16106	-27.910601	-1.148805	2006no	0.25120

Continued on Next Page...

Table B.2 – Continued

SDSS SN ID	Ra	Dec	IAU Name	Redshift
16108	-56.982208	0.570613	2006og	0.15800
16116	-4.697967	-1.105807	2006oh	0.15640
16165	30.733137	-0.533857	2006nw	0.16000
16185	16.868082	-0.269350	2006ok	0.09700
16206	5.788207	-0.053600	2006pe	0.16000
16211	-11.835900	0.266950	2006nm	0.31102
16213	8.971043	0.258397	2006oi	0.19800
16215	18.407681	0.423863	2006ne	0.04660
16232	17.205410	-0.989545	2006oj	0.33970
16259	-7.970020	0.856350	2006ol	0.11912
16276	20.578690	1.010610	2006om	0.16000
16280	14.121716	-1.226700	2006nz	0.03810
16281	-7.057850	-0.668070	2006pd	0.18690
16287	46.664532	0.064050	2006np	0.10737
16314	-39.071072	-0.843467	2006oa	0.06256
16333	-31.006287	-1.070167	2006on	0.07193
16350	-36.360466	-0.885830	2006ph	0.23610
16352	-13.750617	-0.873340	2006pk	0.24800
16357	-29.180790	-0.606843	2006pi	0.37380
16392	27.950609	0.263313	2006ob	0.05917
16402	-23.632271	0.265317	2006sv	0.26450

Continued on Next Page...

Table B.2 – Continued

SDSS SN ID	Ra	Dec	IAU Name	Redshift
16414	-20.673565	0.738160	2006pj	0.30720
16421	51.836227	1.089690	2006pg	0.32030
16442	-30.053190	-0.733220	2006oo	0.28080
16473	-31.387863	0.588490	2006pl	0.21650
16482	-31.290468	0.933647	2006pm	0.21078
16541	57.261864	-0.532770	2006pn	0.13000
16567	25.438065	-0.189123	2006pf	0.40000
16578	-54.186798	-0.848477	2006po	0.17470
16618	21.279375	-1.218960	2006pq	0.20000
16619	25.938721	-1.111930	2006ps	0.06850
16631	54.622795	-0.675560	2006pv	0.20700
16641	23.561220	-0.403600	2006pr	0.12710
16644	36.817379	-0.393467	2006pt	0.29881
16692	-39.617241	0.993307	2006op	0.03409
16737	-47.167313	-0.952317	2006qc	0.16230
16748	7.951325	-0.513940	2006sx	0.23170
16758	-18.387621	1.150830	2006pw	0.32700
16774	35.271698	0.828400	2006sy	0.36583
16776	-12.978583	-0.176077	2006qd	0.26700
16779	45.290520	-0.026250	2006qa	0.39800
16781	52.061047	-0.200945	2006qb	0.32600

Continued on Next Page...

Table B.2 – Continued

SDSS SN ID	Ra	Dec	IAU Name	Redshift
16789	43.784332	0.234795	2006pz	0.32497
16793	-31.424629	0.446995	2006qg	0.20420
16836	16.250851	-0.374675	2006sw	0.33100
16847	-6.678767	0.961083	2006px	0.27700
16872	-33.029091	0.706857	2006qh	0.12660
16894	56.314552	-0.128500	2006tb	0.29650
16899	52.460098	0.295067	2006ta	0.28770
16938	-11.916753	-0.534437	2006qe	0.33843
16941	-4.281413	-0.556410	2006sz	0.19400
16953	12.243635	0.476940	2006pp	0.33900
16956	-57.226612	-0.319970	2006qj	0.10870
17048	27.581514	0.884887	2006qi	0.18900
17081	27.537964	0.420477	2006ql	0.27100
17106	47.008190	0.943407	2006tc	0.21280
17117	40.600311	-0.796530	2006qm	0.14017
17135	56.528252	0.389747	2006rz	0.03092
17168	-20.276182	-1.167077	2007ik	0.18300
17171	-33.497944	-1.217740	2007id	0.16031
17176	-25.597139	0.613330	2007ie	0.09345
17186	31.612844	-0.899547	2007hx	0.07976
17208	1.491593	1.103077	2007ic	0.14300

Continued on Next Page...

Table B.2 – Continued

SDSS SN ID	Ra	Dec	IAU Name	Redshift
17215	54.926346	1.092273	2007hy	0.18138
17218	-3.828170	-0.030063	2007jp	0.18000
17220	9.701510	-0.179310	2007ji	0.18200
17223	26.361357	-0.019420	2007jj	0.23600
17253	2.994223	0.998160	2007jq	0.15900
17254	8.391867	0.984927	2007ii	0.26300
17258	35.738651	1.025733	2007jr	0.08900
17274	-0.658507	0.105860	2007ij	0.18400
17280	55.791901	0.102477	2007ia	0.13099
17332	43.773479	-0.147413	2007jk	0.18284
17340	41.212070	0.364843	2007kl	0.25729
17366	-44.212711	-1.029193	2007hz	0.13933
17389	-36.705132	-0.960143	2007ih	0.17100
17391	-12.447563	-0.931403	2007jo	0.19400
17435	20.344603	-0.014823	2007ka	0.22200
17460	42.083656	-0.288163	2007km	0.24800
17464	6.640813	0.042000	2007jb	0.28000
17497	37.136597	-1.042103	2007jt	0.14478
17500	4.189404	1.200897	2007lf	0.04407
17528	-49.725170	-0.422120	2007iy	0.37100
17552	-37.679462	-1.003167	2007jl	0.25700

Continued on Next Page...

Table B.2 – Continued

SDSS SN ID	Ra	Dec	IAU Name	Redshift
17568	-46.897053	0.277665	2007kb	0.14000
17605	-50.797230	0.098447	2007js	0.16800
17629	30.636423	-1.089173	2007jw	0.13690
17745	2.960260	-0.339190	2007ju	0.06300
17746	3.903793	-0.389327	2007jv	0.15500
17784	52.461735	0.056837	2007jg	0.03710
17790	-59.363239	0.371683	2007jx	0.17700
17791	-27.626717	0.737930	2007kp	0.28600
17801	-43.906799	-0.898017	2007ko	0.21000
17809	6.364570	-0.839570	2007kr	0.29000
17811	12.878683	-0.947383	2007ix	0.20000
17825	32.947132	-0.912453	2007je	0.16000
17875	20.983383	1.255050	2007jz	0.22200
17880	44.972393	1.160713	2007jd	0.07265
17884	27.599834	1.172077	2007kt	0.24200
17886	54.006413	1.103383	2007jh	0.04075
18030	4.932963	-0.400133	2007kq	0.15646
18091	23.367531	0.524667	2007ku	0.37100
18241	-47.612247	-0.761693	2007ks	0.09500
18298	18.266727	-0.539997	2007li	0.11979
18323	3.428647	0.652160	2007kx	0.16000

Continued on Next Page...

Table B.2 – Continued

SDSS SN ID	Ra	Dec	IAU Name	Redshift
18325	8.905757	0.370037	2007mv	0.25800
18375	11.516453	-0.010383	2007lg	0.11800
18415	-22.521746	1.058577	2007la	0.13000
18451	26.485849	-0.217640	2007mt	0.40800
18456	29.458820	-0.398100	2007lk	0.22000
18463	17.566000	0.472007	2007kv	0.26000
18466	48.418530	0.629983	2007lm	0.21300
18485	47.959126	-0.692440	2007nu	0.28200
18486	55.180023	1.003060	2007ln	0.09000
18602	-21.016407	0.609223	2007lo	0.13800
18604	-19.079107	0.421383	2007lp	0.15000
18612	12.287926	0.596990	2007lc	0.11504
18617	-14.238473	0.849160	2007mw	0.32800
18643	-8.800063	0.944557	2007lv	0.11846
18650	-31.552767	0.015053	2007lt	0.11500
18697	11.223940	-0.997043	2007ma	0.10725
18721	3.077330	-0.077290	2007mu	0.40309
18740	16.855333	1.043777	2007mc	0.15400
18749	12.547347	0.675430	2007mb	0.19000
18751	5.722397	0.775957	2007ly	0.07600
18768	17.216749	1.197873	2007lh	0.19600

Continued on Next Page...

Table B.2 – Continued

SDSS SN ID	Ra	Dec	IAU Name	Redshift
18782	39.262341	-0.866590	2007ns	0.36600
18787	29.729773	-1.027070	2007mf	0.19600
18804	25.265623	-0.448463	2007me	0.20000
18807	46.640938	0.793297	2007mg	0.15818
18809	50.881321	0.666650	2007mi	0.13184
18835	53.685165	0.355520	2007mj	0.12327
18855	48.632370	0.269847	2007mh	0.12782
18890	16.444450	-0.758825	2007mm	0.06643
18903	12.251377	-0.324000	2007lr	0.15638
18909	5.782784	0.983487	2007lq	0.22700
18927	46.682510	-0.754007	2007nt	0.21300
18940	10.348987	0.411937	2007sb	0.21200
18945	10.078393	-1.037377	2007nd	0.26800
18959	36.408745	0.709575	2007ng	0.40108
18965	13.509197	1.069047	2007ne	0.20500
19002	42.615353	-0.551143	2007nh	0.27300
19003	-40.851524	-0.769883	2007mp	0.06115
19008	-28.036654	-1.069917	2007mz	0.23000
19023	-52.883045	0.006233	2007ls	0.24600
19025	-41.454723	-0.296250	2007mx	0.40800
19027	-31.115860	-0.372013	2007my	0.29000

Continued on Next Page...

Table B.2 – Continued

SDSS SN ID	Ra	Dec	IAU Name	Redshift
19033	-43.765518	0.060990	2007of	0.40300
19051	-8.624727	0.423087	2007nb	0.27900
19067	-34.371845	0.984587	2007oq	0.33900
19070	-26.613384	0.880505	2007na	0.47000
19101	7.972727	0.138297	2007ml	0.20200
19149	31.460024	-0.331857	2007ni	0.20800
19155	31.266500	0.174557	2007mn	0.07689
19174	25.659817	1.030370	2007or	0.16600
19207	-26.536036	-0.920280	2007oa	0.25000
19211	-46.846161	-0.453953	2007oh	0.41900
19220	-18.258003	-0.071803	2007ox	0.21200
19282	-0.927800	-0.505863	2007mk	0.18641
19341	15.860275	0.331405	2007nf	0.23500
19353	43.114365	0.251810	2007nj	0.15395
19365	29.411045	-0.522130	2007os	0.34900
19381	50.235516	1.058133	2007nk	0.21600
19389	51.297283	-0.106257	2007nz	0.46900
19425	-36.491272	-0.740520	2007ow	0.21100
19543	-2.091643	0.279823	2007oj	0.12000
19596	53.884266	0.703323	2007po	0.28900
19604	5.324495	1.074560	2007oi	0.30000

Continued on Next Page...

Table B.2 – Continued

SDSS SN ID	Ra	Dec	IAU Name	Redshift
19616	37.101093	0.184685	2007ok	0.16554
19625	34.141289	-0.722390	2007pn	0.31400
19626	35.927898	-0.825970	2007ou	0.11321
19632	40.286552	0.144415	2007ov	0.31500
19658	8.903190	-0.232700	2007ot	0.19900
19702	47.754837	0.356760	2007pp	0.26200
19757	-10.518997	1.222837	2007oy	0.37700
19775	-41.043919	0.651277	2007pc	0.14900
19794	-0.680950	0.249347	2007oz	0.29730
19818	35.266685	0.496400	2007pe	0.30400
19899	-18.507696	-0.648740	2007pu	0.09100
19913	-26.237537	-0.341267	2007qf	0.21000
19940	-44.606464	-0.268477	2007pa	0.15700
19953	-27.069521	0.579063	2007pf	0.12400
19968	24.348757	-0.311987	2007ol	0.05604
19969	31.910473	-0.324003	2007pt	0.17529
19990	34.806313	-0.384843	2007ps	0.24600
19992	-2.895850	-1.184990	2007pb	0.24300
20039	9.878606	1.024367	2007qh	0.24700
20040	-31.120506	0.815070	2007rf	0.29000
20048	-20.691948	0.736347	2007pq	0.18500

Continued on Next Page...

Table B.2 – Continued

SDSS SN ID	Ra	Dec	IAU Name	Redshift
20051	-30.061878	1.126930	2007pv	0.26300
20064	-1.413770	-0.917650	2007om	0.10503
20084	-12.024723	-0.578053	2007pd	0.09125
20097	-48.245441	-0.099330	2007rd	0.24000
20106	-13.445740	0.329000	2007pr	0.33300
20111	-5.605613	0.248113	2007pw	0.24800
20142	23.008253	-0.429703	2007qg	0.32000
20144	-37.568092	0.444617	2007ql	0.23000
20184	-0.211443	1.158317	2007qn	0.32400
20186	-2.705425	0.797910	2007pj	0.34700
20208	32.389874	-1.000607	2007qd	0.04313
20227	-10.880040	-0.098527	2007qi	0.29600
20245	-18.294449	0.756297	2007pi	0.28800
20345	10.701763	0.379773	2007qp	0.27000
20350	-47.194199	-0.955807	2007ph	0.12946
20364	25.756653	-0.945483	2007qo	0.23000
20376	-40.604523	-0.523973	2007re	0.20100
20430	-47.583176	0.468637	2007qj	0.17000
20432	-44.191166	0.457365	2007qk	0.30400
20470	52.604912	1.009433	2007pz	0.12700
20474	-47.165550	1.018913	2007rg	0.45000

Continued on Next Page...

Table B.2 – Continued

SDSS SN ID	Ra	Dec	IAU Name	Redshift
20528	43.121788	-1.139513	2007qr	0.13609
20533	52.355858	-0.646340	2007qt	0.30900
20575	-34.734303	0.142547	2007rh	0.22400
20581	-22.296974	0.010737	2007qm	0.20500
20625	5.683380	-0.479007	2007px	0.10818
20687	16.718121	1.154080	2007ri	0.19100
20718	28.495262	-0.092667	2007rj	0.08879
20764	26.120728	0.229773	2007ro	0.17000
20768	40.625885	-0.971123	2007qq	0.23700
20821	55.572632	1.063133	2007rk	0.19600
20829	-21.863247	0.859100	2007qu	0.31000
20834	15.449173	-0.693620	2007rr	0.19000
20862	-0.494140	-0.737553	2007rn	0.27600
20889	52.381668	0.515563	2007py	0.20929
20934	35.437889	0.864500	2007rm	0.30000
20978	35.387787	-0.374925	2007rl	0.33000
21006	47.941784	0.091893	2007qs	0.29000
21033	28.813673	0.643107	2007qy	0.24000
21034	28.141323	1.244080	2007qa	0.10858
21042	-44.988407	0.827585	2007qz	0.32000
21062	-26.568407	0.396303	2007rp	0.13884

Continued on Next Page...

Table B.2 – Continued

SDSS SN ID	Ra	Dec	IAU Name	Redshift
21422	13.383800	0.900247	2007rq	0.27000
21455	33.799450	0.535903	2007sc	0.26900
21502	-6.400217	-0.890333	2007ra	0.08900
21510	7.352820	0.831490	2007sh	0.14988
21669	11.614180	-1.062250	2007rs	0.12418
21766	27.584187	-0.403885	2007rc	0.12788
21810	-26.845423	0.796737	2007se	0.17600
21814	-17.753696	1.206077	2007sf	0.10000
21839	-41.571613	-0.837870	2007sl	0.09500
21861	-10.141317	-0.901660	2007sg	0.18800
22075	29.963091	1.216435	2007si	0.12995
22182	-39.289295	0.421617	2007sm	0.06000
22284	-26.481598	-0.213173	2007sn	0.13800

REFERENCES

Abazajian, K. et al. 2004, AJ, 128, 502

Adelman-McCarthy, J. et al. 2005, IAU Circ., 8481, 1

Adelman-McCarthy, J. K. et al. 2007, ApJS, 172, 634

Alard, C., & Lupton, R. H. 1998, ApJ, 503, 325

Aldering, G. et al. 2006, ApJ, 650, 510

Barbon, R. 1978, AJ, 83, 13

Barentine, J. et al. 2005a, Central Bureau Electronic Telegrams, 254, 1

—. 2005b, Central Bureau Electronic Telegrams, 259, 1

—. 2005c, Central Bureau Electronic Telegrams, 268, 1

—. 2005d, Central Bureau Electronic Telegrams, 280, 1

—. 2005e, Central Bureau Electronic Telegrams, 247, 1

—. 2005f, Central Bureau Electronic Telegrams, 304, 1

—. 2005g, Central Bureau Electronic Telegrams, 315, 1

—. 2005h, Central Bureau Electronic Telegrams, 339, 1

—. 2005i, Central Bureau Electronic Telegrams, 281, 1

—. 2005j, Central Bureau Electronic Telegrams, 229, 1

Barris, B. J., & Tonry, J. L. 2006, ApJ, 637, 427

Bassett, B. et al. 2007a, Central Bureau Electronic Telegrams, 1076, 1

—. 2007b, Central Bureau Electronic Telegrams, 1079, 1

—. 2007c, Central Bureau Electronic Telegrams, 1081, 1

—. 2007d, Central Bureau Electronic Telegrams, 1098, 1

—. 2007e, Central Bureau Electronic Telegrams, 1102, 1

—. 2007f, Central Bureau Electronic Telegrams, 1104, 1

—. 2007g, Central Bureau Electronic Telegrams, 1109, 1

—. 2007h, Central Bureau Electronic Telegrams, 1117, 1

—. 2007i, Central Bureau Electronic Telegrams, 1128, 1

—. 2007j, Central Bureau Electronic Telegrams, 1135, 1

—. 2007k, Central Bureau Electronic Telegrams, 1137, 1

—. 2007l, Central Bureau Electronic Telegrams, 1139, 1

—. 2007m, Central Bureau Electronic Telegrams, 1146, 1

—. 2007n, Central Bureau Electronic Telegrams, 1167, 1

—. 2007o, Central Bureau Electronic Telegrams, 1061, 1

—. 2007p, Central Bureau Electronic Telegrams, 1057, 1

—. 2006a, Central Bureau Electronic Telegrams, 621, 1

—. 2006b, Central Bureau Electronic Telegrams, 623, 1

—. 2006c, Central Bureau Electronic Telegrams, 624, 1

—. 2006d, Central Bureau Electronic Telegrams, 627, 1

—. 2006e, Central Bureau Electronic Telegrams, 629, 1

—. 2006f, Central Bureau Electronic Telegrams, 637, 1

—. 2006g, Central Bureau Electronic Telegrams, 643, 1

—. 2006h, Central Bureau Electronic Telegrams, 650, 1

—. 2006i, Central Bureau Electronic Telegrams, 654, 1

—. 2006j, Central Bureau Electronic Telegrams, 656, 1

—. 2006k, Central Bureau Electronic Telegrams, 657, 1

—. 2006l, Central Bureau Electronic Telegrams, 663, 1

—. 2006m, Central Bureau Electronic Telegrams, 667, 1

—. 2006n, Central Bureau Electronic Telegrams, 680, 1

—. 2006o, Central Bureau Electronic Telegrams, 688, 1

—. 2006p, Central Bureau Electronic Telegrams, 713, 1

—. 2006q, Central Bureau Electronic Telegrams, 726, 1

—. 2006r, Central Bureau Electronic Telegrams, 735, 1

—. 2006s, Central Bureau Electronic Telegrams, 740, 1

—. 2006t, Central Bureau Electronic Telegrams, 743, 1

—. 2006u, Central Bureau Electronic Telegrams, 745, 1

—. 2006v, Central Bureau Electronic Telegrams, 762, 1

—. 2006w, Central Bureau Electronic Telegrams, 770, 1

—. 2006x, Central Bureau Electronic Telegrams, 786, 1

—. 2006y, Central Bureau Electronic Telegrams, 611, 1

Blanc, G. et al. 2004, A&A, 423, 881

Blanton, M. R. et al. 2003a, AJ, 125, 2348

—. 2003b, ApJ, 592, 819

Blanton, M. R., & Roweis, S. 2007, AJ, 133, 734

Blondin, S., & Tonry, J. L. 2007, ApJ, 666, 1024

Branch, D., Livio, M., Yungelson, L. R., Boffi, F. R., & Baron, E. 1995, PASP, 107, 1019

Cappellaro, E., Botticella, M. T., & Greggio, L. 2007, in American Institute of Physics Conference Series, Vol. 937, Supernova 1987A: 20 Years After: Supernovae and Gamma-Ray Bursters, ed. S. Immler, K. Weiler, & R. McCray, 198–205

Cappellaro, E., Evans, R., & Turatto, M. 1999, A&A, 351, 459

Cardelli, J. A., Clayton, G. C., & Mathis, J. S. 1989, ApJ, 345, 245

Crane, P., Tammann, G. A., & Woltjer, L. 1977, Nature, 265, 124

Dahlen, T. et al. 2004, ApJ, 613, 189

Dilday, B. et al. 2008, ApJ, 682, 262

Dilday et al., B. 2008a, in preparation

—. 2008b, in preparation

Förster, F., & Schawinski, K. 2008, MNRAS, 388, L74

Förster, F., Wolf, C., Podsiadlowski, P., & Han, Z. 2006, MNRAS, 368, 1893

Frieman, J., Turner, M., & Huterer, D. 2008a, ArXiv e-prints, 0803.0982

Frieman, J. A. et al. 2008b, AJ, 135, 338

Fukugita, M., Ichikawa, T., Gunn, J. E., Doi, M., Shimasaku, K., & Schneider, D. P. 1996, AJ, 111, 1748

Gal-Yam, A., Cenko, S. B., Fox, D. B., Leonard, D. C., Moon, D.-S., Sand, D. J., & Soderberg, A. M. 2007, in American Institute of Physics Conference Series, Vol. 924, The Multicolored Landscape of Compact Objects and Their Explosive Origins, 297–303

Gal-Yam, A., Cenko, S. B., Fox, D. W., Leonard, D. C., Moon, D.-S., Sand, D. J., & Soderberg, A. M. 2005, in Astronomical Society of the Pacific Conference Series, Vol. 342, 1604-2004: Supernovae as Cosmological Lighthouses, ed. M. Turatto, S. Benetti, L. Zampieri, & W. Shea, 305–+

Gal-Yam, A., Maoz, D., Guhathakurta, P., & Filippenko, A. V. 2003, AJ, 125, 1087

—. 2008, ApJ, 680, 550

Graham, M. L. et al. 2008, AJ, 135, 1343

Greggio, L. 2005, A&A, 441, 1055

Gunn, J. E. et al. 1998, AJ, 116, 3040

—. 2006, AJ, 131, 2332

Guy, J. et al. 2007, A&A, 466, 11

Guy, J., Astier, P., Nobili, S., Regnault, N., & Pain, R. 2005, A&A, 443, 781

Hamuy, M., Phillips, M., Suntzeff, N., & Maza, J. 2003, IAU Circ., 8151, 2

Hamuy, M., Phillips, M. M., Suntzeff, N. B., Schommer, R. A., Maza, J., & Aviles, R. 1996, AJ, 112, 2391

Hansen, S. M., Sheldon, E. S., Wechsler, R. H., & Koester, B. P. 2007, ArXiv e-prints, 0710.3780

Hardin, D. et al. 2000, A&A, 362, 419

Höflich, P., Khokhlov, A., Wheeler, J. C., Phillips, M. M., Suntzeff, N. B., & Hamuy, M. 1996, ApJ, 472, L81+

Höflich, P., Khokhlov, A. M., & Wheeler, J. C. 1995, ApJ, 444, 831

Hogg, D. W., Baldry, I. K., Blanton, M. R., & Eisenstein, D. J. 2002, ArXiv Astrophysics e-prints, astro-ph/0210394

Holtzman et al., J. 2008, submitted to AJ

Hopkins, A. M., & Beacom, J. F. 2006, ApJ, 651, 142

Howell, D. A., Sullivan, M., Conley, A., & Carlberg, R. 2007, ApJ, 667, L37

Ivezić, Ž. et al. 2007, AJ, 134, 973

James, F., & Roos, M. 1994, MINUIT, CERN, Geneva

Jha, S., Riess, A. G., & Kirshner, R. P. 2007, ApJ, 659, 122

Johnston, D. E. et al. 2007, ArXiv e-prints, 0709.1159

Jorgensen, I. 1997, MNRAS, 288, 161

Kasen, D., & Woosley, S. E. 2007, ApJ, 656, 661

Kessler et al., R. 2008, in preparation

Koester, B. P. et al. 2007a, ApJ, 660, 239

—. 2007b, ApJ, 660, 221

Kuznetsova, N. V., & Connolly, B. M. 2007, ApJ, 659, 530

Li, W. et al. 2003, PASP, 115, 453

Lupton, R., Gunn, J. E., Ivezić, Z., Knapp, G. R., & Kent, S. 2001, in ASP Conf. Ser. 238: Astronomical Data Analysis Software and Systems X, ed. F. R. Harnden, Jr., F. A. Primini, & H. E. Payne, 269–+

Madgwick, D. S., Hewett, P. C., Mortlock, D. J., & Wang, L. 2003, ApJ, 599, L33

Mannucci, F., Della Valle, M., & Panagia, N. 2006, MNRAS, 370, 773

Mannucci, F., Della Valle, M., Panagia, N., Cappellaro, E., Cresci, G., Maiolino, R., Petrosian, A., & Turatto, M. 2005, A&A, 433, 807

Mannucci, F., Maoz, D., Sharon, K., Botticella, M. T., Della Valle, M., Gal-Yam, A., & Panagia, N. 2008, MNRAS, 383, 1121

Matheson, T. et al. 2005, AJ, 129, 2352

Miller, C. J. et al. 2005, AJ, 130, 968

Neill, J. D. et al. 2006, AJ, 132, 1126

Nugent, P., Kim, A., & Perlmutter, S. 2002, PASP, 114, 803

Nugent, P., Phillips, M., Baron, E., Branch, D., & Hauschildt, P. 1995, ApJ, 455, L147+

Oyaizu, H., Lima, M., Cunha, C. E., Lin, H., & Frieman, J. 2007, ArXiv e-prints, 0711.0962

Oyaizu, H., Lima, M., Cunha, C. E., Lin, H., Frieman, J., & Sheldon, E. S. 2008, ApJ, 674, 768

Padmanabhan, N. et al. 2004, New Astronomy, 9, 329

Pain, R. et al. 2002, ApJ, 577, 120

Perlmutter, S. et al. 1999, ApJ, 517, 565

Phillips, M. M. 1993, ApJ, 413, L105

Phillips, M. M. et al. 2007, PASP, 119, 360

Pier, J. R., Munn, J. A., Hindsley, R. B., Hennessy, G. S., Kent, S. M., Lupton, R. H., & Ivezić, Ž. 2003, AJ, 125, 1559

Poznanski, D., Maoz, D., & Gal-Yam, A. 2007a, AJ, 134, 1285

Poznanski, D. et al. 2007b, MNRAS, 382, 1169

Prieto, J. L. et al. 2007, astro-ph/0706.4088

Pskovskii, I. P. 1977, Soviet Astronomy, 21, 675

Quimby, R., Höflich, P., Kannappan, S. J., Odewahn, S. C., & Terrazas, E. 2005, Central Bureau Electronic Telegrams, 266, 1

Riess, A. G. et al. 1998, AJ, 116, 1009

Riess, A. G., Press, W. H., & Kirshner, R. P. 1996, ApJ, 473, 88

Sako, M. et al. 2008, AJ, 135, 348

—. 2005, ArXiv Astrophysics e-prints, astro-ph/0504455

Sand, D. J., Zaritsky, D., Herbert-Fort, S., Sivanandam, S., & Clowe, D. 2008, AJ, 135, 1917

Scannapieco, E., & Bildsten, L. 2005, ApJ, 629, L85

Schechter, P. L., Mateo, M., & Saha, A. 1993, PASP, 105, 1342

Schlegel, D. J., Finkbeiner, D. P., & Davis, M. 1998, ApJ, 500, 525

Sharon, K. et al. 2007a, in American Institute of Physics Conference Series, Vol. 924, The Multicolored Landscape of Compact Objects and Their Explosive Origins, 460–463

Sharon, K., Gal-Yam, A., Maoz, D., Filippenko, A. V., & Guhathakurta, P. 2007b, ApJ, 660, 1165

Sharon et al., K. 2008, in preparation

Sheldon, E. S. et al. 2007a, ArXiv e-prints, 0709.1162

—. 2007b, ArXiv e-prints, 0709.1153

Shimasaku, K. et al. 2001, AJ, 122, 1238

Smith, C., Rest, A., Hiriart, R., Becker, A., Stubbs, C. W., Valdes, F. G., & Suntzeff, N. 2002, in Presented at the Society of Photo-Optical Instrumentation Engineers (SPIE) Conference, Vol. 4836, Survey and Other Telescope Technologies and Discoveries. Edited by Tyson, J. Anthony; Wolff, Sidney. Proceedings of the SPIE, Volume 4836, pp. 395-405 (2002)., ed. J. A. Tyson & S. Wolff, 395–405

Smith et al., M. 2008, in preparation

Stoughton, C. et al. 2002, AJ, 123, 485

Strateva, I. et al. 2001, AJ, 122, 1861

Strauss, M. A. et al. 2002, AJ, 124, 1810

Strolger, L.-G., & Riess, A. G. 2006, AJ, 131, 1629

Strolger, L.-G. et al. 2004, ApJ, 613, 200

Sullivan, M. et al. 2006a, AJ, 131, 960

—. 2006b, ApJ, 648, 868

Tonry, J., & Davis, M. 1979, AJ, 84, 1511

Tonry, J. L. et al. 2003, ApJ, 594, 1

Webb, A. 2002, Statistical Pattern Recognition: 2nd Edition (West Sussex, England: John Wiley and Sons, Ltd.)

Williams, R. D., & Seaman, R. 2006, in Astronomical Society of the Pacific Conference Series, Vol. 351, Astronomical Data Analysis Software and Systems XV, ed. C. Gabriel, C. Arviset, D. Ponz, & S. Enrique, 637–+

Yamauchi, C. et al. 2005, AJ, 130, 1545

Zheng, C. et al. 2008, AJ, 135, 1766